Corrosion Studies of Platinum Nano-Particles for Fuel Cells

Shim, Signe Sarah; Chorkendorff, Ib; Andersen, Steen Yde

Publication date:
2012

Document Version
Publisher's PDF, also known as Version of record

Corrosion Studies of Platinum Nano-Particles for Fuel Cells

Signe Sarah Shim

The Technical University
of Denmark
Department of Physics

IRD Fuel Cells A/S
R&D Department

January 16, 2012

Preface

The present thesis is submitted in candidacy of the Ph.D. degree from the Technical University of Denmark (DTU). It represents results obtained during my work at IRD Fuel Cells A/S and at Center for Individual Nanoparticle Functionality (CINF), Department of Physics, Technical University of Denmark. The work was carried out from January 2008 to September 2011 under the supervision of Professor Ib Chorkendoff from CINF, DTU and Research Manager Steen Yde Andersen from IRD fuel cells. Financial support was provided by IRD Fuel Cells, Energi Fyns Udviklingsfond and the Danish Agency for Science, Technology and Innovation through the Industrial Ph.D. Fellowship Program.
The focus of the project has been on development and understanding of the degradation mechanism of platinum and platinum alloy catalysts for Proton exchange membrane (PEM) fuel cells. The results obtained during the Ph.D. period have brought new knowledge to IRD Fuel Cells. A substantial amount of time have been spent on introducing and developing new techniques to IRD Fuel Cells.
I would like to express my gratitude towards the electrochemistry group at DTU for always being part of the project, especially Dr. Francisco Perez-Alonso and Dr. Billie Abrams with whom I have had excellent collaborations. I am especially grateful for the extremely useful input I received in the final phase of the project from Dr. Francisco Perez-Alonso.
I would like to thank all my colleagues at IRD Fuel Cell A/S for their contributions to the present project. A special thanks to Senior Research Scientist Peter B. Lund for many valuable discussions and for his always positive attitude.

Signe Sarah Shim
Svendborg, January 16, 2012

Abstract

The main focus of the present thesis is on corrosion and prevention of corrosion of platinum particles supported on carbon. This is important for instance in connection with start up and shutdown of fuel cells.
The degradation mechanism of platinum particles supported on carbon has been characterized during oxygen reduction reaction (ORR) condition using identical location (IL) transmission electron microscopy (TEM). A TEM grid was used as the working electrode in an electrochemical setup allowing a direct correlation between the electrochemical response and the TEM analysis. The main results of the corrosion was a decrease in the particle size, some particles disappeared and other particles sintered. The TEM observations of the platinum particles provide evidence that dissolution of platinum particles is one of the main causes of degradation of platinum particles supported on carbon under ORR conditions.
In the present work the corrosion stability of three commercial catalysts have been investigated. Even though they have similar specifications they have different corrosion stabilities. From an industrial point of view it is interesting that the catalyst supplied by company 2 is much more corrosion stable and has a higher utilization of the platinum surface area than the other catalysts investigated.
The experiments preformed revealed that platinum particles can be stabilized against corrosion by adding gold to the platinum particles. In the present work electrocatalysts with one third, two thirds and one monolayer of gold on platinum supported on carbon were synthesized by an inverse micelle method. The results obtained appear independent of the gold coverage. It has been shown that the electrochemical active surface areas of the platinum and platinum gold particles synthesized by the inverse micelle method were very low compared to the theoretical calculated surface areas.
In the present work it was attempted to synthesize 5 nm platinum particles supported on carbon by the polyol method. The performed experiments showed that a gaussian particle size distribution of platinum particles is obtained when the carbon dispersion is added after the reduction of the platinum particles. If the reduction of the platinum particles are preformed before adding the carbon dispersion a bi normal size distribution of platinum particles is obtained. The level of water in the polyol method does not appear to have the effect on the platinum particle size as reported in the literature.

Resume

Hovedfokus i afhandlingen er på korrosion og forebyggelse af korrosion af platin-partikler supporteret på kulstof. Dette er vigtigt for eksempel i forbindelse med opstart og nedlukning af en brændselscelle.
Nedbrydnings-mekanismen for platin-partikler supporteret på kulstof er bestemt ved hjælp af transmissions-elektron-mikroskopi (TEM) idet de samme steder på prøven er undersøgt før og efter ilt-reduktions-reaktionen (ORR). Den direkte sammenhæng mellem den elektrokemiske behandling og TEM analyser er belyst ved at anvende et TEM gitter som arbejdselektrode i en elektrokemisk opstilling. De vigtigste resultater af korrosions-testen var at nogle platin-partikler forsvandt mens andre platin-partikler sintrede sammen. TEM studierne af platin-partiklerne dokumenterede, at opløsning af platin-partikler er en af de væsentligste årsager til nedbrydning af platin-partikler supporteret på kulstof under ORR betingelser.

I det udførte arbejde er korrosions-stabiliteten af tre kommercielle katalysatorer blevet undersøgt. På trods af at de næsten har identiske datablade er deres korrosions stabilitet meget forskellige. Fra et industrielt synspunkt er det interessant, at katalysatoren fra selvskab 2 er langt mere korrosions-stabil og at den har en højere udnyttelse af platin-overfladen end de øvrige undersøgte katalysatorer. Det er desværre ikke muligt at oplyse navnene på katalysator leverendørende på grund af fortrolighedsaftaler.
Det eksperimentelle arbejde, der er gennemført i projektet, viste at platin-partikler kan stabiliseres mod korrosion ved at tilføje guld til platin-partiklerne. Der er blevet syntetiseret katalysatorer med henholdsvis en tredjedel, to tredjedele og et monolag af guld på platin-partiklerne supporteret på kulstof med omvendt-micelle-metoden. Korrosions-stabiliteten af guld platin-partiklerne synes at være uafhængig af guld-dækningsgraden. Det elektrokemiske aktive overflade-areal af platin- og platin-guld-partiklerne syntetiseret med inverse micelle metoden var meget lavt i forhold til det teoretisk beregnede overflade-areal.
Syntetisering af 5 nm platin-partikler supporteret på kulstof er forsøgt ved brug af polyol-metoden. De udførte eksperimenter viste, at platin-partiklerne havde en Gauss-størrelsesfordeling når kulstof dispergeringen blev tilføjet efter reduktionen af platin-partiklerne. Hvis operationen blev udført i omvendt rækkefølge blev størrelsefordelingen af platin partiklerne bi-normal. I litteraturen er det rapporteret at mængden af vand anvendt i polyol-motoden havde en indvirkning på størrelsen af de syntetiserede platin-partikler. Dette kunne ikke verificeres i de udførte experimenter.

List of Included Papers

Identical location transmission electron microscopy study of Pt/C electrocatalyst degradation during oxygen reduction reaction
F. J. Perez-Alonso, C. F. Elkjær, S. S. Shim, B. A. Abrams, I. E. L. Stephens, I. Chorkendoff
Journal of Power Sources, **196**, 6085, (2011)

Other Publications

First principles calculations and experimental insight into methane steam reforming over transition metal catalyst
G. Jones, J. G. Jacobsen, S. S. Shim, J. Kleis, M. P. Andersson, J. Rossmeisl, F. Abild-Petersen, T. Bligaard, S. Helveg, B. Hinnemann, J. R. Rostrup-Nielsen, I. Chorkendoff, J. Sehested, J. K. Nørskov
Journal of catalysis, **259**, 147, (2008)

Magnetic order in perovskite-related $SrFeO_2F$
F. J Berry, R. Heap, Ô. Helgasson, E. A. Moore, S. Shim, P. R. Slater, M. F. Thomas
Journal of Physics: Condensed Matter, **20**, 5207, (2008)

Contents

Chapter 1

Introduction

A major problem with the sustainable energy sources such as wind and solar energy is there reliability. Energy will only be produced when the wind blows or the sun shines. Furthermore, the need for power varies during the day. Hence, there are major demands for new ways to store the energy so it can be released on marked demands. Synthetic fuels and methanol are candidates for energy carriers but the most promising candidate is hydrogen. Hydrogen can be produced from water and it can be used directly in a fuel cell [1].
A fuel cell converts chemical energy from a fuel into electricity through a chemical reaction with oxygen or another oxidizing agent. Hydrogen is a common fuel for use in fuel cells but hydrocarbons such as natural gas and alcohols such as methanol are also usable. Fuel cells are different from batteries since they require a constant supply of fuel and oxygen to run, if this is fulfilled they should be able to supply electricity continuously.
In a fuel cell the electricity is generated directly from the chemical reaction. The efficiency for fuel cells are around 80% [2].
Proton exchange membrane (PEM) fuel cells could play a major role in a future carbon-free society, with their ability to convert chemically stored energy into electricity. The most significant obstacle preventing the widespread utilization of PEM fuel cells is their high cost. A significant portion of their cost can be traced to the poor activity and low stability of the platinum particles supported on carbon used at the cathode, which drives the oxygen reduction reaction (ORR) [3].
Platinum is a scares resource and the high cost of the platinum is a limiting factor for the mass production of PEM fuel cells [4]. Therefore, it would be advantageous if the amount of platinum could be reduced or if platinum could be replaced by a cheaper and more abundant metal. Furthermore, both the platinum metal and the carbon support are subject to different types of corrosion in the harsh environment of a fuel cell.

1.1 Thesis outline

The main focus of this thesis is to elucidate the corrosion mechanism for platinum in a fuel cell. Furthermore, new catalysts that might be more corrosion stable are synthesized for the cathode in a fuel cell.
The thesis has been divided into 8 chapters. In Chapter 2 an introduction to the fuel cell is given. Furthermore, degradation mechanisms for platinum corrosion and some suggestions regarding the prevention of corrosion of platinum particles are briefly reviewed.
In Chapter 3 the experimental techniques used in the project are described. Chapter 4 describes the identical location TEM studies of Pt/C electrocatalyst degradation during the oxygen reduction reaction. In Chapter 5 the degradation of three commercial electrocatalysts during the oxygen reduction reaction is studied. Due to confidentiality agrement it is not possible to state the names of the manufactures. Chapter 6 focuses on the manufacturing of Pt/Au electrocatalysts and on their degradation during oxygen reduction reaction. Chapter 7 describes the polyol synthesis of platinum particles on a carbon support. Finally, Chapter 8 summarizes the conclusions and outlook on future investigations.

Chapter 2

Fuel cells

In this chapter the history and the principles behind fuel cells are briefly outlined. Furthermore, the different types of fuel cells are briefly reviewed. The main focus in the present project is on the prevention of catalyst degradation in connection with fuel cells, hence a review of catalyst degradation in fuel cells are presented at the end of the Chapter.

2.1 History

The lawyer and scientist William Grove in 1839 was the first to demonstrate the principle of a fuel cell. In Grove's setup two glass tubes were used, one filled with hydrogen and one filled with oxygen. The two tubes were placed in a beaker with an acid electrolyte. A platinum wire was placed in each tube and the wire was in contact with both the gas and the electrolyte. Grove used a galvanometer to show that a current was flowing between the platinum wires. Over a period of 24 hours, the reaction had consumed a substantial part of the hydrogen and oxygen [2, 5]. A schematic drawing of Grove's setup is presented in Figure 2.1.

2.2 Principle

In a fuel cell hydrogen and oxygen reacts to produce water. During the reaction electrical energy and heat are being produced.
In the original experiment performed by Grove the interfaces between the gas, the platinum electrodes and the electrolyte were very small. The small area was a limiting factor for the current that could be drawn from the system. Therefore, the contact area in present days fuel cells are maximized to generate larger currents in a layered structure called a membrane electrode assembly (MEA).
In a fuel cell the reacting gasses must be spatially separated and the electrons are guided through and external circuit. To obtain the spatial separation of the gasses an electrolyte, that only conducts ions and not electrons, is used. Both sides of the electrolyte have to be in contact with the electrodes as well as with the gasses. On the anode side the electrode collects electrons from the fuel. The electrons pass through an external circuit and on the cathode side they are used to reduce the gas. Thus, the reaction of the fuel is split into two electrochemical half cell reactions. The reaction of hydrogen and oxygen are

$$\text{Anode} \qquad \mathrm{H_2} \rightarrow 2\mathrm{H^+} + 2e^- \tag{2.1}$$

$$\text{Cathode} \qquad \frac{1}{2}\mathrm{O_2} + 2\mathrm{H^+} + 2e^- \rightarrow \mathrm{H_2O} \tag{2.2}$$

The anode reaction is the hydrogen oxidation reaction (HOR) while the cathode reaction is the oxygen reduction reaction (ORR).
A schematic drawing of a fuel cell is presented in Figure 2.2.

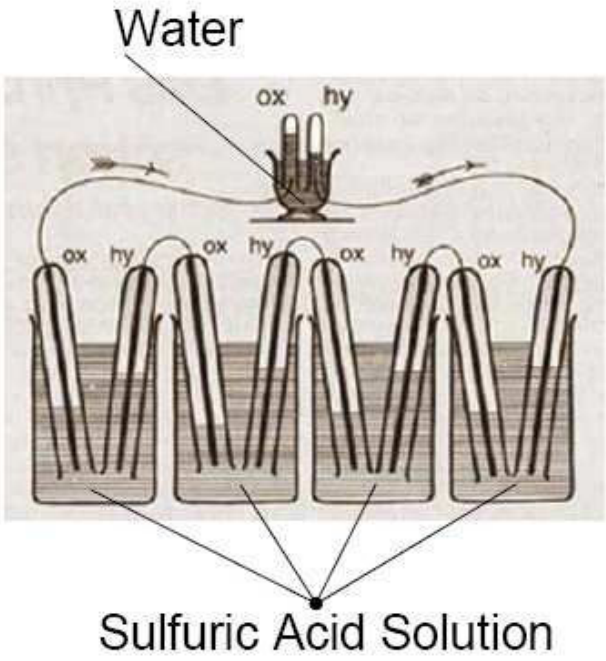

Figure 2.1: A schematic drawing of the setup used by Grove. [6]

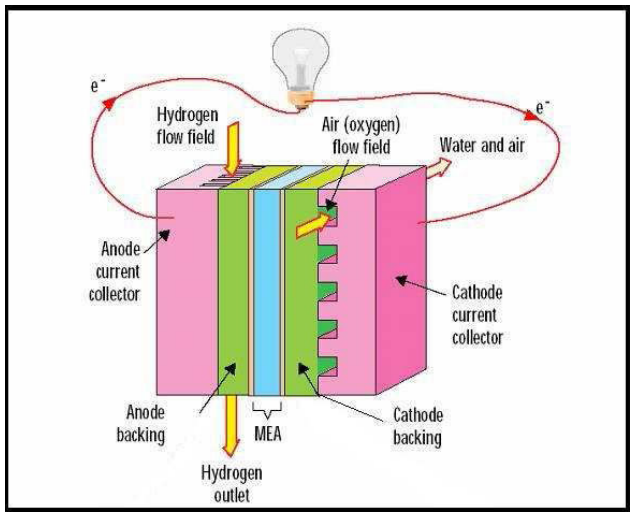

Figure 2.2: A schematic diagram of a fuel cell. The MEA is a membrane electrode assembly [7]

2.3 Types of fuel cells

Presently, fuel cells are classified in many different categories [2]. An overview is given in Table 2.1. The different types of fuel cells have been developed with different objectives. Therefore, each of them have some advantages and some disadvantages. The present project is focused on development of catalyst material for the proton exchange membrane fuel cells (PEMFC). Thus, such fuel cells will be described in detail in the following sections.

Table 2.1: Data for different types of fuel cells

Fuel cell (FC) type	Mobile ion	Operation temperature
Alkaline (AFC)	OH^-	50-200°C
Proton exchange membrane (PEMFC)	H^+	30-100°C
High temperature Proton exchange membrane (HT-PEMFC)	H^+	100-200°C
Direct methanol (DMFC)	H^+	20-90°C
Phosphoric acid (PAFC)	H^+	$\sim$ 220°C
Molten carbonate (MCFC)	CO_3^{2-}	$\sim$650°C
Solid oxide (SOFC)	O^{2-}	500-1000°C

2.4 Proton exchange membrane (PEM) fuel cell

The proton exchange membrane (PEM) fuel cell that is also named the polymer electrolyte (PEM) fuel cell was first developed by General Electric in USA in the 1960s for use by NASA in their first manned space vehicles [2].

2.4.1 Membrane electrode assembly (MEA)

The heart of the PEM fuel cell is the membrane electrode assembly (MEA), which is a layered structure consisting of the polymer electrolyte in the middle and on each side a catalytic active electrode that form the anode and the cathode, respectively. A schematic drawing of the PEM fuel cell is illustrated in Figure 2.3.

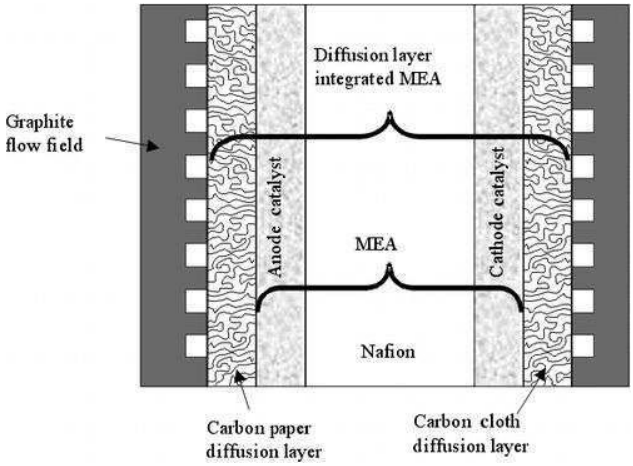

Figure 2.3: Schematic diagram of a membrane electrode assembly (MEA)

The PEM fuel cell uses hydrogen at the anode side and either oxygen or air at the cathode side. The mobile

ions in PEM fuel cells are protons that are transported through the membrane while the electrons are passed through an external circuit.
The PEM fuel cell works at temperatures between 30-100°C, which gives the possibility of a quick start [2]. The individual parts of the MEA is described in the Subsections 2.4.1.1 to 2.4.1.3.

2.4.1.1 Membrane

The polymer electrolyte membranes are produced by different companies. The most popular is Nafion produced by Dupont. This membrane is a sulphonated fluoroethylene which has a ionic sulfonate group, SO_3^-. The structure of Nafion is illustrated on Figure 2.4.

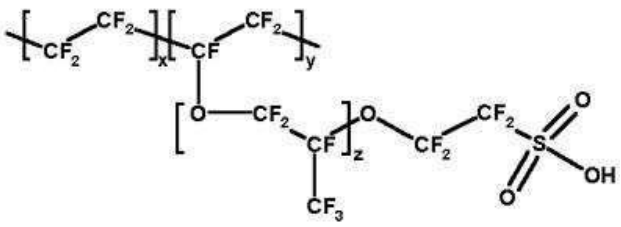

Figure 2.4: The structure of Nafion.

The presence of the SO_3^- groups generate hydrophilic regions within an overall hydrophobic structure. The hydrophilic SO_3^- groups can absorb a high quantity of water thereby enhancing there capability of proton conduction. The protons are able to move around in the membrane because they are weakly bound to the SO_3^- groups.
The proton conductivity of the membrane is directly proportional to the water content. However, the water should not flood the electrodes that are bound to the membrane since flooding will result in malfunction of the fuel cell.
In a PEM fuel cell the water produced at the cathode, in an ideal world, would be enough to keep the membrane humidified and a possible excess of water would be removed by the air blowing over the cathode. In reality the gasses used in a fuel cell have to be humidified to make sure that the water needed for conduction the ion is present in the PEM fuel cell [2].

2.4.1.2 Electrodes

The catalysts used in a PEM fuel cell today is either an alloy of platinum and ruthenium at the anode side and platinum at the cathode side or just pure platinum on both sides.
The catalyst layers are placed on each side of the membrane so each have contact to the membrane and to the gas diffusion layer. This is illustrated in Figure 2.3.
The catalyst particles are nano sized particles on the surface of a support. The support is typically a carbon based powder. A transmission electron image of platinum on a carbon support is shown in Figure 2.5.
The contact between the catalyst, electrolyte and the gas is called the three phase boundary. To exploit the catalyst particles it is important that all the particles are in contact with both electrolyte and gas. The incoming gas is adsorbed and thereafter dissociated at the three phase boundary. The protons are transported through the membrane and the electrons are transported via the catalyst support to the external circuit. On the cathode side the protons and the electrons are combined with oxygen to produce water. [8]

2.4.1.3 Gas diffusion layer (GDL)

The gas diffusion layers are placed on each side of the membrane with the catalyst layer between the membrane and the gas diffusion layer. The gas diffusion layer consists typically of a carbon cloth or paper with a thickness of around 0.2 to 0.5 mm.

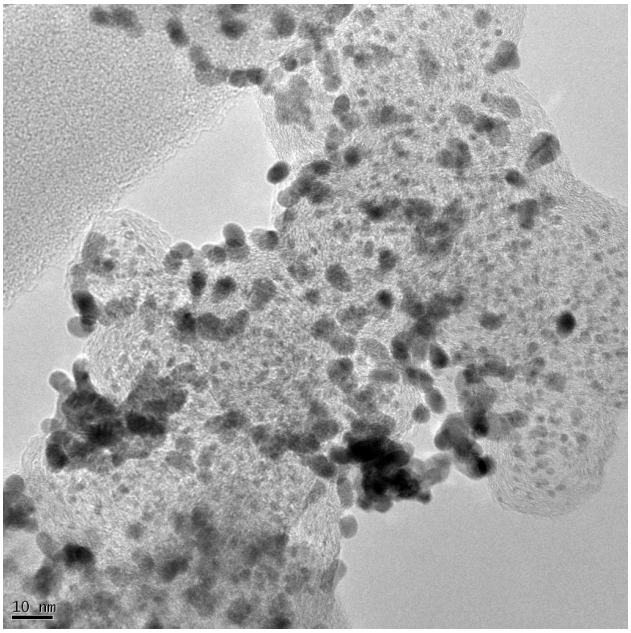

Figure 2.5: A transmission electron microscope image of platinum on a carbon support. The platinum particles are the small dark particles.

The gas diffusion layer has a number of different functions. It diffuses gas to the catalyst layer but in addition it also forms electrical contact between the carbon supported catalyst and the current collectors. Furthermore, it carries the produced water away form the electrolyte [2].

2.5 Electrocatalysis

Electrocatalysis refers to systems where a catalyst is used in an electrochemical reaction. As background a brief introduction to the areas of electrochemistry and catalysis are given.

2.5.1 Catalysis

The term catalysis was introduced by the Swedish scientist Jöns Jacob Berzelius in 1836 and further defined by Wilhelm Ostwald. A catalyst accelerates a chemical reaction without changing the equilibrium of the reaction and without being part of the final product. A catalyst provides an alternative path for the reaction where the activation energy is lower than in the reaction without the catalyst [1]. Thus, the catalyst increases the reaction rate.
A catalyst facilitates a reaction by forming bonds to the reacting molecules, allowing these to react to a product, which finally detaches from the catalyst. The catalyst is left unchanged and available for the next reaction. This is called a catalytic cycle.
An example of a free energy diagram for a reaction with and without a catalyst present is shown in Figure 2.6.
Figure 2.6 shows that the activation energy of the catalyzed reaction is lower than the activation energy of the uncatalyzed reaction. Thus, the catalyst provides an alternative reaction path with lower barriers. The catalyst cannot change the thermodynamic equilibrium of a reaction, only the kinetics of the reaction is changed. The overall change in the Gibbs free energy of the catalytic reaction equals that of the uncatalyzed reaction. The catalyst accelerates the forward and the reverse reaction to the same extent.

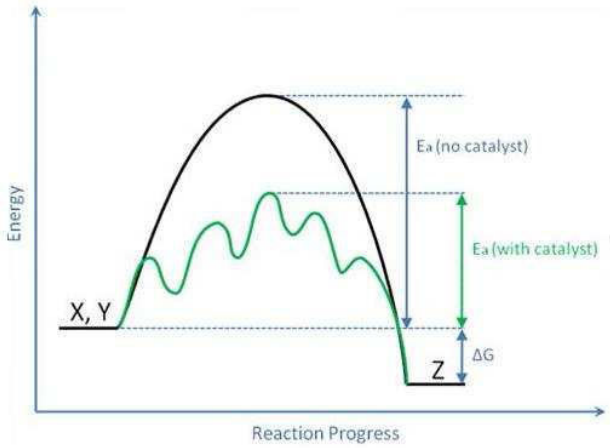

Figure 2.6: The free energy diagram for at catalyzed and a non-catalyzed reaction.

2.5.1.1 Heterogeneous Catalysis

In heterogeneous catalysis the reactants and the catalyst are in different phases [1]. Often the catalyst is solid and the reactants are in liquid or gaseous phases. In this case the surface is the catalytic active part. Economic use of the catalytic material requires a high surface area relative to the volume of the particles. The catalysts are therefore usually nanometer-sized particles supported on an inert porous structure. A specific problem encountered is the tendency of the nano particles to sinter thereby minimizing their surface energy. Thus, a lower surface area is available for the reaction.

2.5.2 Electrocatalysis

Electrocatalytic reactions are a class of reactions that involves transfer of electrons between a metal surface and a molecule adsorbed on the surface. In the simple case an electrochemical reaction can proceed over three steps. In step one an atom is adsorbed on the metal surface and an electron is transferred to the adsorbed atom. In step two the adsorbed atom takes part in a reaction and a product is formed. In the final step the product is desorbed form the surface. During the electrochemical reaction the metallic surface becomes charged resulting in a electric double layer. therefore the positively charged surface will have predominantly negative charged ions in the electrolyte close to the surface and visa versa. [9, 10]

2.6 Surface Energy

When a surface is created from a bulk material bonds are broken. Therefore, it costs energy to create a surface. When a bulk material is transformed from one piece to several smaller pieces the total energy of the system increases. Hence, the surface free energy of the system is always positive.
Minimization of the surface free energy γ is a driving force for several surface processes, i.e:

- Surfaces are always covered by a substance that lowers their surface free energy. In the case of metals they are usually covered by a monolayer of oxides.
- In order to minimize the surface energy of a clean polycrystalline metal particle they normally expose their most densely packed surface. Thereby, a minimum number of bonds have to broken to generate the surface.
- Open surfaces often reconstruct so the atoms in the surface have a maximum number of neighbors.

- In alloys the components with the lowest surface free energy segregate to the surface. Thereby, minimizing their overall energy of the surface. Hence, the surface composition of a alloy can be different from that of the bulk composition of the same alloy.
- Impurities in metals such as carbon, oxygen or sulphur segregate to the surface of the metal because impurities have a lower surface free energy. Hence, segregating to the surface of the metal lowers the overall surface energy of the metal.
- When small particles are dispersed on a surface of a support they have a tendency to sinter because loss of surface area implies lowering of the total energy.

As described in Section 2.5.1.1 heterogeneous catalysis is a surface phenomenon. In order for the catalyst material to be used in the most economical way the active catalyst particles have to be small and they are usually dispersed on a suitable support material. One of the interesting properties for catalytic active particles are there dispersion. The dispersion is the fraction of atoms located in the surface of the particle [1].
From a thermodynamic point of view the equilibrium shape of a platinum particle is determined by a minimization of the surface energy provided that edge and curvature effects are negligible. For an ideal face centered cubic structure as platinum the surface energy follow the order $\gamma\{111\}_{Pt} < \gamma\{100\}_{Pt} < \gamma\{110\}_{Pt}$ [11, 12]. The equilibrium shape of a platinum particle at zero absolute temperature is shown in Figure 2.7 [13].

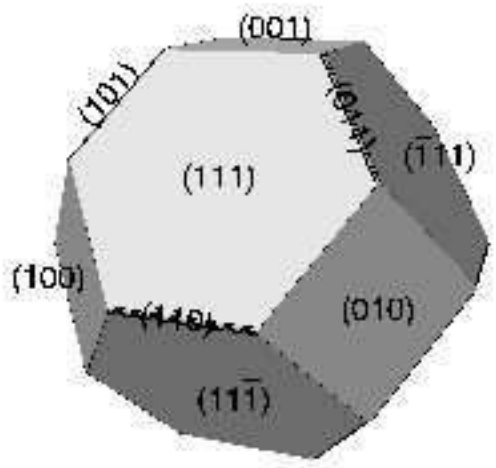

Figure 2.7: The equilibrium shape of platinum at zero temperature. [13]

The shape of the platinum particle shown in Figure 2.7 is that of a free platinum particle. However, the platinum particles used in a fuel cell are supported by carbon. Thus, the platinum particles in the fuel cell are not free and therefore they cannot minimize their free energy by merging to form larger particles. The shape of the platinum particles supported by carbon are dependent on the synthetic conditions, the energy of the platinum surface, the interface between the platinum particle and the support and the environment of the platinum particles. The synthetic conditions may vary the nucleation and growth rates of platinum clusters on the support [14].
The shape of the platinum particles are also dependent on the energy associated with the interface between the particles and the carbon support. When the interface energy increases the particles wet the surface of the support.

2.7 Catalyst degradation

The degradation of carbon supported platinum catalysts is one of the most important factors that decrease the operation lifetime of PEM fuel cells. [15–17]. The surface of platinum is the only part of the platinum metal that is electrochemically active and thus contributes to the fuel cell electrode reactions. Therefore, a high performance of the fuel cell electrodes is associated with a high electrochemically active surface area of the platinum metal. During operation the electrochemical active surface area of platinum decreases, and this results in decrease of the performance of the PEM fuel cell.

2.7.1 Degradation mechanism

The degradation of the catalyst in a fuel cell can be divided into two areas. One is the degradation of the carbon support and the other is the degradation of the platinum layer. These two areas are closely related because platinum might catalyze the oxidation of carbon and the oxidation of carbon accelerates the sintering of platinum.
The size of the platinum particles in a fuel cell is in the nanometer scale, usually between 2-6 nm. Platinum particles of that size show strong tendency to agglomerate due to there high surface energy. [16, 18, 19]. For nanoparticles the surface energy is reduced substantially by agglomeration. When platinum particles agglomerate the electrochemical active surface area decreases causing a decrease in the performance of the fuel cell. It is generally believed that the electrochemical surface area of platinum is an important parameter for characterizing a fuel cell electrode. A larger electrochemical active surface area implies that more catalytic active sites are available for the reaction, hence a higher performance of the fuel cell. Shao-Horn *et al.* [20] reported that the degradation in the performance of a fuel cell is largely due to the loss of electrochemical active surface area.

The loss of platinum surface area has been attributed to four different processes:

- Ostwald ripening of platinum particles involves dissolution of platinum from small platinum particles, transport of the dissolved platinum species and redeposition which occurs by reduction of platinum species from solution onto larger particles [21]. This process is similar to the Ostwald ripening process decribed in Refs. [22,23], that typically involves transport of atoms or small clusters from small particles to larger particles via the surface of the catalyst support layer. The mechanism is driven by the reduction of surface energy.
  This mechanism is likely to be partially responsible for the loss of electrochemical active surface area at the cathode, when it is exposed to voltages higher then 0.8 V. At this voltage the solubility of platinum is high [21].

- The particle migration and coalescence mechanism results in a log-normal shape of the particle size distribution with a tail towards the large particle sizes. The mechanism can be described by surface migration of platinum particles on the carbon surface, 2D motions of platinum particles and coalescence when the platinum particles meet [24, 25].
  From studies of platinum on carbon support in gas-phase it is seen that the platinum metal sinter when they are exposed to temperatures above 500°C but below this temperature the sintering by particle migration is insignificant [26]. Experimental evidence that this mechanism occurs in a fuel cell has not yet been reported. However, it has been proposed that this process is responsible for the loss of electrochemical active surface area when the cell voltage is lower then 0.7 V because the solubility of platinum under these conditions are low [27].

- Dissolution of the platinum particles and re-precipation in the ionomer phase forming new catalytically inactive platinum particles thereby reducing the electrochemical active surface area [20].

- Detachment of platinum particles from the carbon support. This mechanism is generally due to carbon corrosion. The extent to which this mechanism contributes to the reduction of the electrochemical

active surface area is dependent on the potential and on the nature of the interaction between the platinum particles and the carbon support [20].

It is clear that loss of platinum by either one of the four above mentioned mechanisms can be source of degradation of the cathode in a PEM fuel cells.
For a 2 nm platinum particle about half the atoms are in the surface layer, which implies that a significant amount of platinum can be lost through dissolution of only the surface layer.
There are already some evidence that manipulation of the surface structure of platinum could lead to higher stability of platinum particles in a fuel cell environment. V. Komanicky *et al.* [28] reports that surfaces containing edges and corners dissolve faster at higher potential indicating that edges and corners are the main source of dissolution. J. Greeley *et al.* [29] have performed density functional theory (DFT) calculations showing that (211)-steps have lower activity toward oxygen reduction reaction than terraces [29]. Furthermore, it is found that dissolution of edges and corners are shown not to have any effect on the activity of adjacent active sites [30].
Thus, from the literature it is predicted that for platinum the steps and edges have lower activity toward oxygen reduction reaction then terraces. Since it is predicted that the dissolution of platinum is higher from steps and edges not much activity toward oxygen reduction reaction (ORR) would be lost if the steps and edges of platinum are blocked. Zhang *et al.* [31] showed that platinum for the oxygen reduction reaction is stabilized against dissolution under potential cycling regimes by adding gold to the platinum nanoparticles. The gold atoms are deposited electrochemically on the platinum particles and thereby the platinum are stabilized toward dissolution.
Several studies [32–34] have shown that the corrosion of platinum particles are very dependent on the size of the platinum particles. Jinnouchi et al [32] have performed calculations showing that the redox potentials for platinum atoms at the edges are lower than for the platinum atoms at the flat surface. Hence, platinum atoms at the edges are easier to dissolve. A large particle has few edges per volume than a smaller particle and thus smaller particles are easier dissolved than larger particles. Furthermore, their calculations have shown that the platinum particles are not stabilized by the π-sites in the carbon support.
Holby et al [33] and Tang et al [34] have shown that particles from 2 nm to 5 nm are unstable. This suggest that an increase in the platinum particle size from the commonly used 2-3 nm particles to particles with an average diameter of 5 nm could provide an enormous gain in the stability of the platinum particles.
The results raise promising possibilities for synthesizing improved oxygen reduction reaction platinum based catalysts and also for stabilization of platinum particles.

2.7.2 Pourbaix diagrams

A Pourbaix or an equilibrium diagram maps out the possible stable phases of an aqueous electrochemical system. The Pourbiax diagrams for platinum, gold and tantalum are shown in Figure 2.8.
Common for the three diagrams are that the corrosion indicated in the diagrams denotes a reaction between the metal and the non-metalic environment which results in a continuing destruction of the metal. Furthermore, immunity in the diagrams denotes the state in which corrosion is thermodynamically impossible in a particular environment. Passivation in the diagrams denotes the process that leads to a state where the metal is protected from corrosion by a modification of the surface layer caused by the environment surrounding the metal.
From a fuel cell perceptive the interesting area is at pH around -2 to 0 and at a potentials from 0.2 to 1.2 V. This is the environment the catalyst in a fuel cell experiences during fuel cell operation. The Pourbiax diagram for platinum shows three regions at the interesting pH values. Platinum should be immune from below 0 V and up to approximately 0.9 V. Above 0.9 and up to 1.2 V platinum could undergo corrosion. Above 1.2 V and at pH higher than 2 platinum is passivated by surface oxide.
One of the metals that could be used to prevent corrosion of platinum in a fuel cell is gold. As noted from the Pourbiax diagram gold metal could be immune towards corrosion in the fuel cell environment as long as the potential is kept below approximately 1.3 V.
Another metal that could prevent corrosion of platinum is tantalum because it forms an oxide in a fuel cell

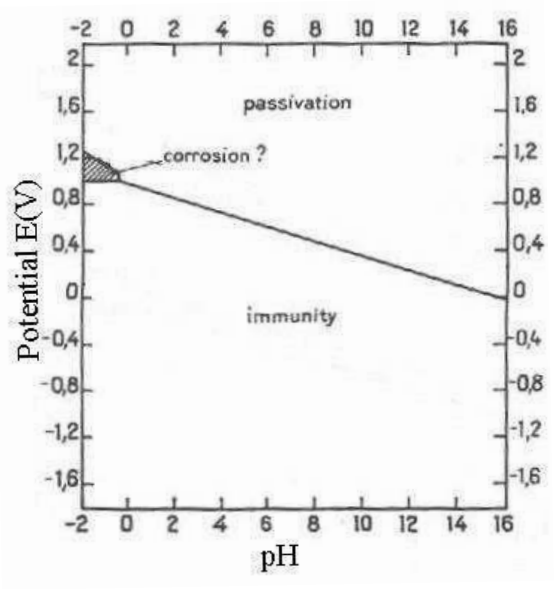

(a) Pourbaix diagram at 25°C for Platinum [10]

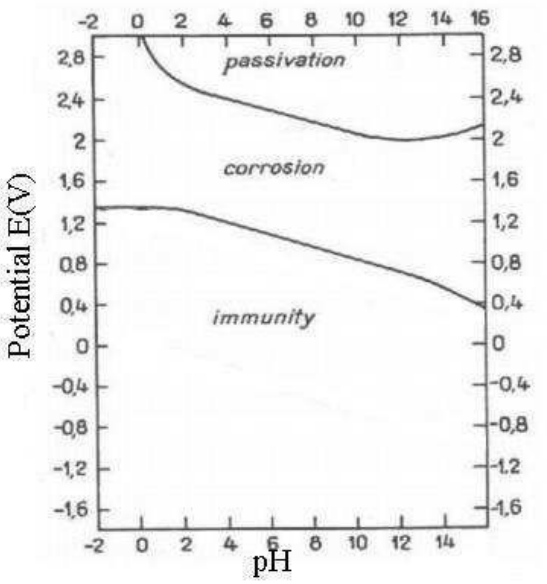

(b) Pourbaix diagram at 25°C for Gold [10]

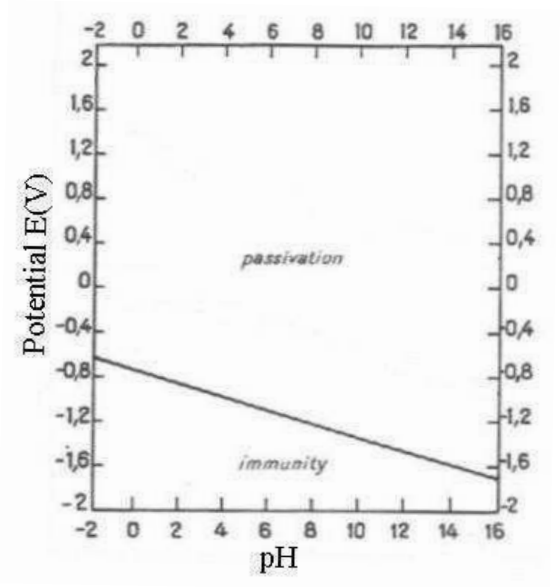

(c) Pourbaix diagram at 25°C for Tantalum [10]

Figure 2.8: Pourbaix diagrams for (a) Platinum, (b) Gold and (c) Tantalum. Corrosion denotes a reaction between the metal and the non-metalic environment which results in a continuing destruction of the metal. Immunity denotes the state in which corrosion is thermodynamically impossible in a particular environment. Passivation denotes the process that leads to a state where the metal is protected from corrosion by a modification of the surface layer caused by the environment that the metal is exposed to [10].

environment and thereby becomes immune toward corrosion in this environment.
Even though the Pourbiax diagrams indicate that the pure metals are stable in the fuel cell environment, the diagrams do not predict the behavior of the alloys. Therefore the diagrams only offer indications as to the behavior of the metals in the fuel cell.

2.7.3 Dissolution of platinum nano particles

According to Pourbiax [10] platinum can be oxidized by the following two reactions:

$$Pt(s) \rightleftharpoons Pt^{2+}(aq) + 2e^- \tag{2.3}$$

$$Pt(s) + H_2O \rightleftharpoons PtO(s) + 2H^+ + 2e^- \tag{2.4}$$

The platinum-oxide may dissolve chemically in acid to form Pt^{2+}. The equilibrium concentration of platinum can be related to the applied potential E by the Nernst equation

$$C_{Pt} = \exp \frac{2F(E - E_0(T))}{RT} \tag{2.5}$$

where C_{Pt} is the concentration of dissolved platinum in mole/L, F is the Faraday constant, E is the applied voltage vs reversible hydrogen electrode (RHE), $E_0(T)$ is the reversible voltage vs RHE, R is the gas constant and T is the temperature.
The dissolution of platinum nano particles can be significant different form that of the bulk platinum metal because platinum particles have larger surface areas per unit volume.

The change in the chemical potential can be related to the size of the platinum particles using the Gibbs-Thomson formula [35]

$$E_{GT} = \mu(d) - \mu\infty = \frac{4\gamma\Omega}{d} \tag{2.6}$$

where γ is the surface energy and Ω is the volume per atom. The Gibbs-Thomson energy is plotted as a function of the platinum particle diameter in Figure 2.9 [20]. The parameters used in deriving the plot are $\gamma = 0.148 eV/\text{Å}^2$ and $\Omega = 15.4\ \text{Å}^3/atom$ [36].

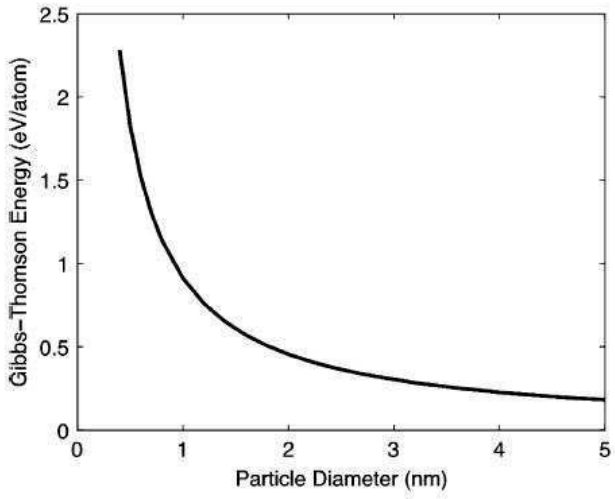

Figure 2.9: The Gibbs-Thomson energy as a function of the platinum particle diameter. Graph adapted from [20].

The Gibbs-Thomson energy can be included in the Nernst equation giving

$$C_{Pt} = \exp \frac{2F(E - E_0(T) + E_{GT}/2)}{RT} = \exp \frac{2F(E - E_0(T) + 2\gamma\Omega/d)}{RT} \tag{2.7}$$

As shown in Figure 2.9 the Gibbs-Thomson energy increases by 0.18 eV when the diameter d of the particles decrease from ∞ to 5 nm but when d decreases further from 5 nm to 1 nm the Gibbs-Thomson energy increases by 0.73 eV. Thus, as indicated by the modified Nernst equation it is expected that the Gibbs-Thomson energy should have a large impact on the solubility of small platinum particles. Therefore, the equilibrium concentration of platinum in solution should be strongly dependent on the particle diameter. However, according to Shao-Horn et al [20] there are little experimental evidence that the Gibbs-Thomson energy plays a major role in the solubility of platinum.

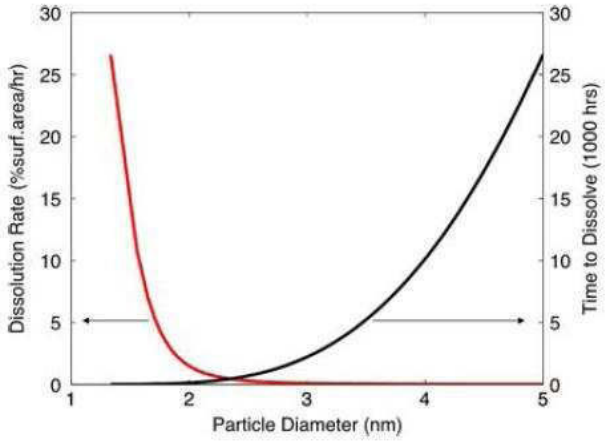

Figure 2.10: Simulated dissolution of platinum particles as function of their diameter. The simulation has been carried out by Shao-Horn et al [20] at a potential of 0.95 V vs. RHE, a platinum loading of 0.4 mg/cm^2 and with the assumption of 10 μL electrolyte close to the cathode. Graph adapted from [20].

Shao-Horn et al [20] have studies the dissolution rate of platinum particles as function of their diameters. The result of their simulations are shown in Figure 2.10. In their simulation they considered a constant potential of 0.95 V and a platinum loading of 0.4 mg/cm^2. Furthermore, 10 μL of electrolyte next to the cathode is assumed. Figure 2.10 shows a strong dependence between the particle size and the dissolution rate. This dependency is most pronounced for particles with a diameter below 5 nm. The dissolution rate can be related to a lifetime under the assumption that the dissolution flux of a particle with an initial diameter is constant. However, this assumption is not correct since the particle diameter is not constant when it dissolves. Hence, the flux is not constant and the lifetime of the particles are overestimated. The estimated lifetimes of the particles give a clear qualitative picture of the particle dissolution. Particles with a diameter around 5 nm could have the stability to last for thousands of hours as required by PEM fuel cells in the automotive applications [37]. Smaller particles, however, would according to the calculations dissolve quickly.
Thus, corrosion of platinum nano particles could depend on the size of the particles as well as on the potential of the fuel cell system.

2.8 Corrosion in Fuel cells during start and stop

Under normal fuel cell operations, the highest potential that the cathode encounters will be the open circuit voltage (OCV), which is around 1.0 V. When a fuel cell is in use its cathode potential is likely to be between 0.4 and 0.7 V. At such potentials the corrosion will not be severe. However, during start up ad shut down of the fuel cell part of the cathode could experience a potential as high as twice the OCV.
The high potential is caused by the anode which is partly filled with hydrogen and partly filled with air. The electrochemical phenomena under these conditions have been explained by Reiser et al [38] with a one dimensional electrochemical potential profile model. The model indicates that the potential of an anode

partly exposed to air drops from 0 V to 0.59 V. This results in a raise of the potential at the interface of the cathode to around 1.44 V [38–41]. A schematic drawing of the boundary is shown in Figure 2.11.

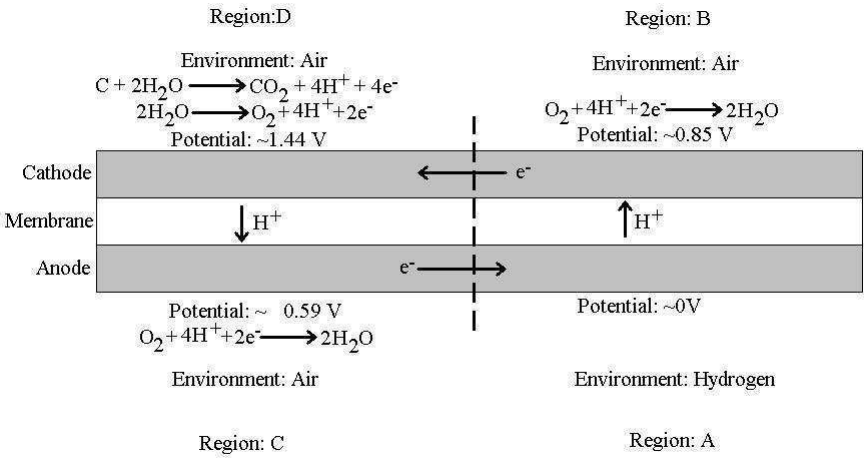

Figure 2.11: A schematic illustration of the air/fuel boundary at the anode side. Region D experiences a very high potential. Under these conditions corrosion occurs [38, 39].

After a shut down of the fuel cell un-reacted air and hydrogen are present at the cathode and the anode side, respectively. If the anode outlet is open, air will gradually diffuse into the anode side of the fuel cell where it will create a hydrogen/air boundary. This boundary will move along the flow channel until it reaches the end of the flow channel. Figure 2.11 shows four regions marked A, B, C and D. In region A the anode is filled with hydrogen and the potential is 0 V. Region C is on the anode side and filled with air, the potential of this region drops to approximately -0.59 V [38]. Region B is on the cathode side and filled with air, this region have a potential around OCV. Region D on the cathode side is also filled with air but this region experiences a higher potential due to the lower potential in region C. Hence, region D is subject to a potential around 1.44 V [38].
This situation is likely to happen during start up and shut down of the fuel cell, but it can also occur during operation if oxygen diffuses through the membrane to the anode from the cathode or if the anode is locally starved. Prevention of such air/hydrogen boundary formation at the anode during shut down and start up of a fuel cell is crucial to achieve a longer lifetime for a MEA.

Chapter 3

Experimental techniques

In this chapter the experimental techniques used in the present project are described. One technique that is used is transmission electron microscopy (TEM). The transmission electron microscope is used to determine the particle size distribution (PSD) of the catalysts investigated. The microscope that have been available during the project was a Tecnai T20 G2 Transmission Electron Microscope. Therefore, the technology described in the following section is the technology related to the Tecnai T20 G2. The technology used in this microscope is not the state of the art within transmission electron microscopy. The state of the art microscope within ex-situ transmission electron microscopy are microscopes that have a field emission gun (FEG) as the electron source. A field emission gun has an energy spread that is 5 times less than that of LaB_6 which is the one used in the Tecnai T20 G2 transmission electron microscope used in the present project. The resolution of a transmission electron microscope can be further enhanced bye spherical aberration correction resulting in reduction of the point resolution of the microscope [42]. This is not the case for the Tecnai T20 G2 transmission electron microscope used in the present project. Hence, this will not be subject to further discussions.
A short review of X-ray diffraction (XRD) is also included. The data from the XRD measurements are supplied by the manufactures of the catalysts. These data are used to support the results obtained from the transmission electron microscopic investigations.
Finally, a short review of the electrochemical method used to determined the electrochemical active surface area of the catalysts is given.

3.1 Transmission electron microscope (TEM)

In 1925 Louis de Broglie suggest that electrons had a wave-like character [43]. In 1927 Davisson and Germer as well as Thompson and Reid, independently carried out experiments that demonstrated the wave nature of electrons. Shortly after this experimental work the idea of an electron microscope was proposed. The electron microscope was developed by Ruska and Knoll in 1939. Ruska received the Nobel prize for his work in 1986. A transmission electron microscope was applied to the field of catalysis by Turkevich [44] in 1945. At that time the resolution limit of the transmission electron microscope was 5 nm. A common theme was the study of catalysts treated at high temperature, which lead to a decrease in the surface area of the catalysts. A theme that is still being subject to intense studies.

A transmission electron microscope is in many ways analogous to an optical microscope. The main difference being that electrons are used instead of photons. A sample is illuminated by a broad beam of electrons, which after passage through the sample are projected onto a two-dimensional image. The electrons are only transmitted through very thin samples, i.e. with a thickness of a maximum of 100 nm.
A schematic diagram of a TEM is shown in Figure 3.1. The electron emitting source is at the top of the microscope. A two or three stage condenser lens system permits variation of the illumination intensity of

the sample. The electron intensity distribution of the beam after passing through the sample is magnified with a three or four stage lens system onto a fluorescent screen. The image can be recorded digitally via a fluorescent screen coupled by a fiber optic plate to a camera.

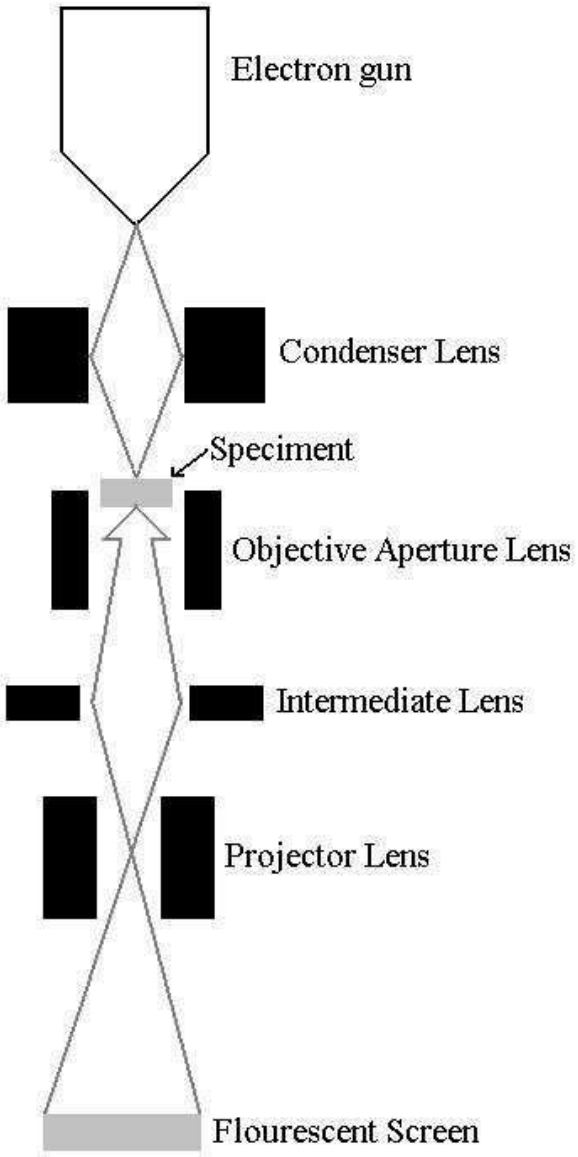

Figure 3.1: A schematic diagram of a transmission electron microscope (TEM).

The transmission electron microscope is very sensitive to the environment. Even slight vibrations in the vicinity of the microscope decreases the resolution and thereby the quality of the images. Variations in the power source give rise to changes in the lens strength and decreases the resolution of the microscope. Often transmission electron microscopes are placed in an isolated room and on a damped platform to minimize the influence of external sources thereby optimizing the resolution.

3.1.1 The electron source

To obtain the highest possible resolution, coherent and monochromatic electron sources are used. A monochromatic beam does not have an energy spread of the electron emerging from the source. In a coherent beam all the waves are in phase. [43]
In the Tecnai T20 G2 transmission electron microscope the electron source is LaB_6. Compared to tungsten used in the used in the first electron microscopes LaB_6 provides a higher brightness and a smaller energy spread [43]. When a LaB_6 electron source is used the vacuum in the microscope has to be 10^{-4} Pa.

3.1.2 The lens system

The lens systems in the transmission electron microscopes are electromagnets. Busch (1927) was the first to successfully focus an electron beam. He used an electrostatic field to focus the electron beam. When current is passing through the lens it gets heated, and therefore the lens have to be cooled. A water cooling system is an essential part of TEM lens systems. The current passing through the lens is used to adjust the strength of the lens.

3.1.3 The imaging system

The transmission electron microscope can project two different images onto a viewing screen. The microscope can project an image of the diffraction plane, which also can be considered as an image of the reciprocal space. In addition, the microscope can project an image of real space onto the viewing screen. Switching between the two projections is easily done by changing the strength of the intermediate lens. This is illustrated in Figure 3.2.
The image on the viewing screen shows the intensity of the beam. The intensity can be recorded by transmission to a camera. The difference in intensity for two adjacent areas is the contrast.
There are three different kinds of contrasts, i.e. mass-thickness, diffraction and phase contrast. In the present project only mass thickness contrast have been used and this imaging method is described in the following section.

3.1.3.1 Mass thickness contrast

Mass thickness contrast is caused by incoherent Rutherford scattering of the electron beam. The cross section for the Rutherford scattering is strongly dependent on the atoms in the sample through their atomic number Z. Hence thicker regions or regions containing heavier elements will scatter the electron beam more strongly. Such regions will therefore appear darker. Electrons coming from lighter elements or thin regions will appear bright in the image. This is illustrated in Figure 3.3.

3.1.4 The contrast transfer function

The contrast transfer function describes the performance of the imaging optics of the transmission electron microscope. The contrast transfer function oscillates in such a way that it shows bands of good transmission and bands of no transmission. Figure 3.4 shows a one dimensional projection of the contrast transfer function for the Tecnai T20 G2 microscope.
Positive contrast results when the contrast transfer function shown in Figure 3.4 is negative. In this case the atoms appear dark against a bright background. When the contrast transfer function is positive, negative contrast results, and the atoms appear bright against a dark background.
The point resolution is defined as the point where the contrast transfer function goes from negative to positive the first time. The information limit is the minimum distance in the sample that can be resolved in the image. For the Tecnai T20 G2 microscope the point resolution is 0.24 nm and the information limit is 0.14 nm.

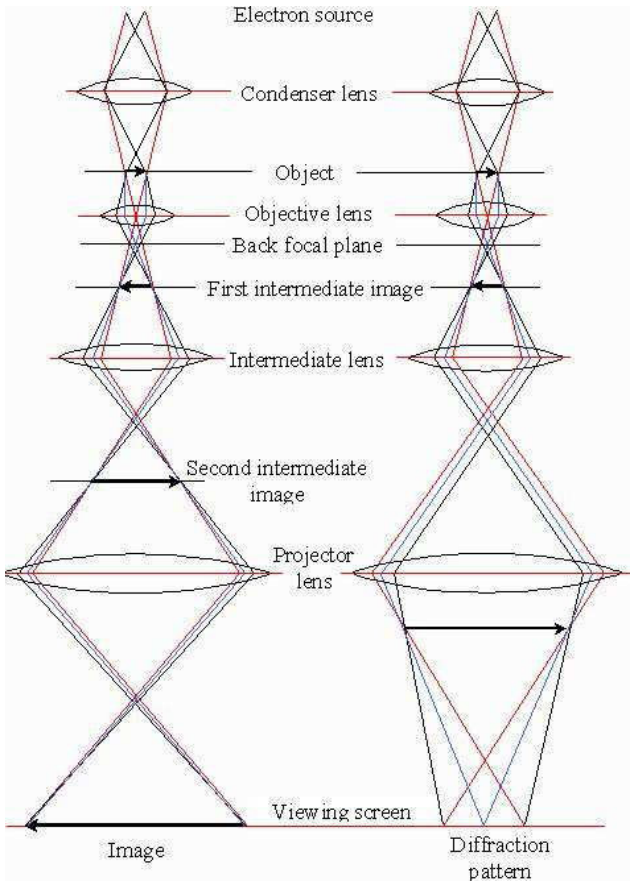

Figure 3.2: A schematic diagram of the imaging system in a TEM. The TEM images the diffraction image or the real space image depending on the strength of the intermediate lens.

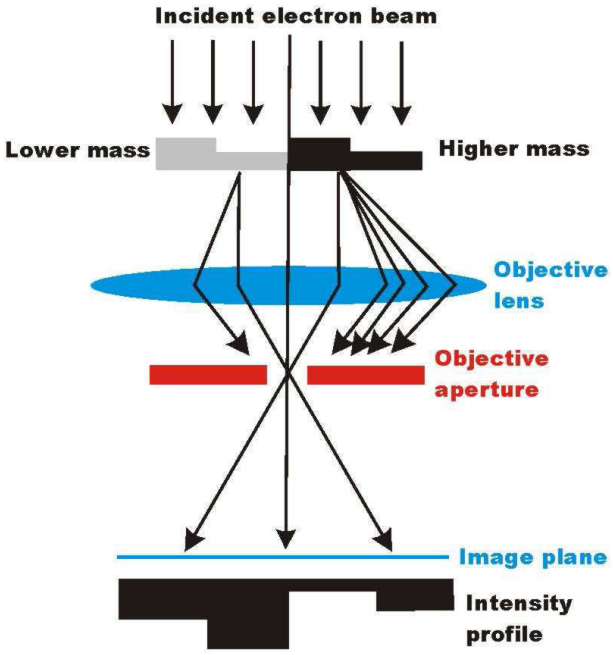

Figure 3.3: Schematic diagram of the mass thickness contrast.

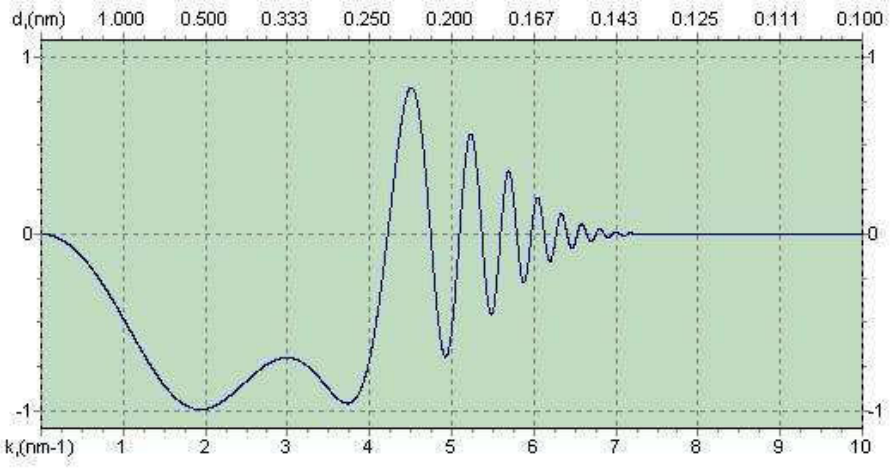

Figure 3.4: The contrast transfer function for Tecnai T20 G2 transmission electron microscope. The values used are $V = 200\,keV$, $C_s = 1.2\,nm$, $C_c = 1.2\,nm$ and a energy spread of $0.6\,eV$. The point resolution is around 0.24 nm and the information limit is 0.14 nm. [45]

3.1.5 TEM measurements of average particle diameter for a powder sample

The particle size distributions and the average diameter of the particles are determined using a transmission electron microscope. All samples used in the present work were treated by an identical experimental method. Each sample was crushed and dispersed dry on a TEM grid. The grid was mounted in a standard TEM holder and inserted in the TEM.
Since platinum has a higher atomic number Z than the carbon support, the platinum particles appear as dark spots on the carbon support.

Table 3.1: The settings of the transmission electron microscope images for different samples

Identical Location Images		
	Magnification:	195.000X
	Image area:	113.023 nm × 113.023 nm
	Resolution in pixel:	0.055 nm/pixel
	TEM Grid:	Gold
	Number of images:	20-25
Standard samples		
	Magnification:	97.000X
	Image area:	227.15 nm × 227.15 nm
	Resolution in pixel:	0.11 nm/pixel
	TEM Grid:	Copper
	Number of images:	15-20
Pt/Au		
	Magnification:	97.000X
	Image area:	227.15 nm × 227.15 nm
	Resolution in pixel:	0.11 nm/pixel
	TEM Grid:	Copper
	Number of images:	20-25
Platinum fabricated by polyol method:		
	Magnification:	195.000X
	Image area:	113.023 nm × 113.032 nm
	Resolution in pixel:	0.055 nm/pixel
	TEM Grid:	Copper
	Number of images:	20-25

The settings used in the transmission electron microscope are listed in Table 3.1. At the 195.000× magnification and 97.000× magnification the limiting parameter in the resolution is the point resolution of 0.24 nm in the contrast transfer function. This, however, does not effect the measurements since the particles are larger than 0.24 nm in diameter.

The sizes of the particles have been analyzed by manually outlining the edge of the projected particle in ImageJ version 1.41 (Wayne Rasband, National Institutes of Health, USA). ImageJ measures the projected area of the particle. The projected area was approximated by a circle, and the diameter of the particle was calculated. A histogram of the particle diameters vs. the number of particles in the bin was plotted. The width of a bin is denoted Δ and care is needed in choosing the width Δ. In case the bins are too wide all the data points fall into one bin, or if the bins are too narrow, only few of the bins contain more than one data point.
The literature is not very clear regarding the choice of Δ, but Freedman *et al.* [46] suggest a simple robust rule for choosing the bin size. This rule is

$$\Delta = 2(\mathrm{IRQ})\mathrm{N}^{-1/3} \tag{3.1}$$

N is the number of data points and IRQ is the inter quartile range of the data set i.e. the range between the third and the first quartiles. A quartile is any of the three values which divide the data set into four equal parts, with each part representing 1/4th of the sample. The above rule often gives quite reasonable results. The rule is used in the present work when generating the histograms of the particle size distributions.

The literature does not provide consensus regarding the uncertainty of the average particle diameters measured with TEM. The work presented in Refs. [27, 47–58] reports the TEM diameter of their samples.
Thus, Antolini [48] and Koutsopolos *et al.* [49, 50] report the TEM average diameter without stating any uncertainty of the average diameters.
Other authors Wilson *et al.* [27], Han *et al.* [51–53], Frelink *et al.* [54], and Prabha *et al.* [55] all report the average diameters and uncertainties of the average diameters, but they do not discuss how the uncertainties are determined.
Prabhuram *et al.* [56], Mokhonoana *et al.* [57], and Teranishi *et al.* [58] reports the uncertainties of the average diameters measured with TEM as the standard deviations. On this background it has been chosen to report the uncertainties of the average diameters of the platinum particles as the standard deviations in the present work.

3.2 X-ray diffraction

X-ray diffraction is one of the oldest and a frequently used technique for characterization of catalysts [1]. X-ray diffraction is used to identify crystal phases within catalysts and to obtain an indication of the particle size.
X-ray diffraction is due to the elastic scattering of X-ray photons by atoms in a periodic lattice. The scattered monochromatic X-rays in phase interfere constructively. The lattice spacing is obtained from the diffraction of X-rays by crystal planes using the Bragg law:

$$n\lambda = 2dsin\theta;\ n = 1, 2, ... \tag{3.2}$$

n is an integer which denotes the order of the reflection, λ is the wavelength of the X-rays, d is the distance between two lattice planes, and θ is the angle between the incoming X-ray and the normal to the reflecting lattice plane. Constructive interfering X-rays occurs at the angle 2θ. Under this condition the Bragg relation gives the corresponding lattice spacing, which is characteristic for a particular compound.
With powdered samples, an image of diffraction lines occurs because a small fraction of the particles is oriented with a certain crystal plane at the angle θ relative to the incident beam leading to constructive interference.
Narrow diffraction peaks are only observed when the sample has sufficient long range order. This implies that the peak in a diffraction spectrum carries information on the size of the reflective planes. Diffraction lines from a perfect crystal are very narrow. However, when the crystallite size is below 100 nm, line broadening occurs due to incomplete destructive interference in scattering directions, i.e. the X-rays are out of phase. The Scherrer formula relates the crystal size to the line width

$$< L > \propto \frac{1}{\beta} \tag{3.3}$$

$< L >$ is the size of the particle in the direction perpendicular to the reflecting plane and β is the full width at half maximum of the peak.
X-ray lines provide a quick but not always reliable estimate of the particle size. Since the size measured by X-ray diffraction is the size of the domain in the particle. A particle consisting of more than one domain is a poly crystalline particle.

3.2.1 X-ray diffraction measurements

The average particle diameter of the particles measured with XRD was reported by the manufacture of the catalysts.

3.3 Electrochemical method

To investigate the start op and shut down of a fuel cell a model system can be studied. The phenomena can be modeled by a thin film study. In such a study the catalyst experiences an environment similar to the environment in a fuel cell, but the sources of errors have been eliminated. Thus, the influence of the flow channels, gas diffusion layer etc. on the performance and on the corrosion of the fuel cell have all been eliminated. Hence, only the corrosion of the platinum surface in the fuel cell environment is studied. The thin film approach has been widely described in the literature [31, 59–61].

The thin film study is carried out by fabricating an ink of the catalyst material under investigations. A drop of the ink is placed on a glassy carbon electrode that is used as the working electrode in a three electrode half cell setup often used in electrochemistry. A three electrode half cell setup consists of a working electrode (WE), a counter electrode (CE) and a reference electrode (RE). The three electrodes are placed in a suitable container that contains a liquid electrolyte. Figure 3.5 shows a schematic drawing of the electrochemical setup.

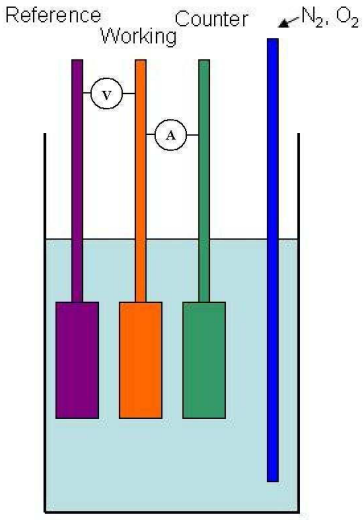

Figure 3.5: Schematic drawing of a three electrode electrochemical setup.

The three electrode setup is typically controlled by a potentiostat which makes it possible to impose a well defined potential to the working electrode. The potential is measured between the working electrode and the reference electrode while the current flows between the working electrode and the counter electrode. Electrochemical reactions can be studied when different gasses are introduced into the electrolyte. In this type of experiment it is important that the volume of the electrolyte is sufficiently large so that the reaction occurring at the electrode does not change the composition of the electrolyte.

3.3.1 Cyclic Voltametry (CV)

Cyclic voltametry is a widely used technique for acquiring qualitative information about electrochemical reactions. It can provide information on redox processes, heterogeneous electron-transfer reactions and absorbtion processes.
Cyclic voltametry consists of linearly scans of the potential form E_1 to E_2 of a working electrode. The rate by which the potential is raised is called the scan rate. During the potential sweep, the potentiostat measures the current resulting form electrochemical reactions. The resulting cyclic voltagram is the response of the current as a function of the applied potential.

3.3.1.1 Cyclic Voltagram for a platinum surface

The interactions between the platinum surface and the surrounding media introduce a chemical reaction which can be studied by cyclic voltametric (CV) measurements in an inert environment. Bett *et al.* [62] have studied chemisorption of hydrogen on a platinum surface. Figure 3.6 shows a voltagram for a platinum sample from the work of Bett *et al.* reported in [62].

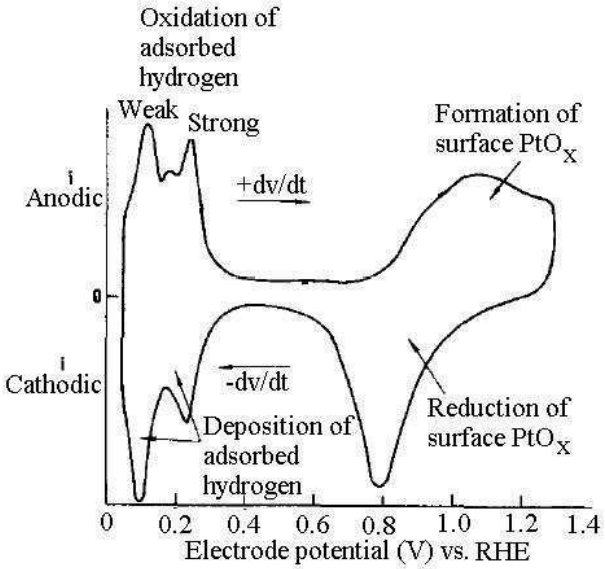

Figure 3.6: Voltagram of platinum. The voltagram is recorded in 20% H_2SO_4 with nitrogen bobbled through. The graph shows adsorption and desorption of hydrogen and the formation and reduction of platinum surface oxides.

In the forward scan oxidation of weakly and strongly adsorbed species occur below 0.4 V vs reversible hydrogen electrode (RHE). Formation of surface platinum oxides occurs at potentials above 0.8 V vs RHE, in the forward scan. In the reverse scan reduction of the platinum surface oxides occur at a potential above approximately 0.6 V vs RHE. Hydrogen is adsorbed at potentials below 0.4 V vs RHE on the reverse scan. The integrated peak charge below the oxidation of adsorbed hydrogen can be used to evaluate the electro chemical active area. For platinum a full mono layer of hydrogen is assumed to correspond to 210 $\mu C/cm^2$ [63].
In the present work all the potentials have been measured using a $HgHgSO_4$ reference electrode with a potential of 0.720 V vs RHE in 0.1 M $HClO_4$. All the potentials in the present work reported refer to RHE.

3.3.1.2 Cyclic Voltagram of single crystal platium

Cyclic voltagrams of platinum single crystals have been recorded by Markovic *et al.* [64]. Figure 3.7 shows cyclic voltagrams of platinum (111), (100) and (110) surfaces. Graphs adapted from Markovic *et al.* [64].
The cyclic voltagram for platinum (111) in 0.1 M H_2SO_4 gives broad nearly flat hydrogen desorption/adsorbtion peaks at potentials below approximately 0.4 V in 0.1 M H_2SO_4. At higher potentials anomalous peaks are observed. In 0.1 M H_2SO_4 adsorption and desorption of (bi)sulfate anions occur between approximately 0.4 V and 0.6 V. In 0.1 M $HClO_4$ adsorption and desorption of hydroxyl species occur at potentials between approximately 0.6 V and 0.85 V.
The cyclic voltagram for platinum (100) in 0.1 M H_2SO_4 shows two well defined peaks at 0.4 V and 0.25 V which correspond to the coupled processes of hydrogen adsorption and bisulfate anion desorption. The main characteristic of a platinum (100) surface in $HClO_4$ is that hydrogen adsorption/desorption and hydroxyl anion adsorbtion/desorbion are not completely decoupled process. Hence, desorption of hydrogen at

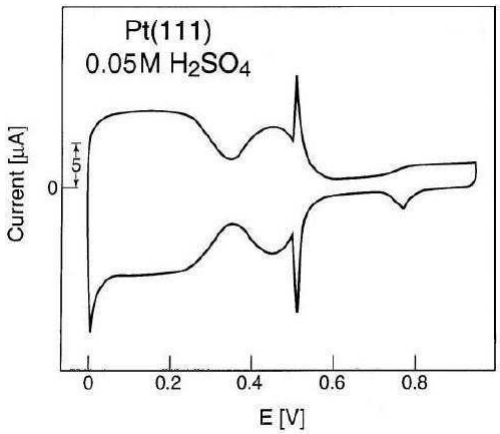

(a) Cyclic voltagram for a platinum (111) surface in H_2SO_4. The voltagram gives broad nearly flat hydrogen desorption/adsorbtion peaks at potentials below approximately 0.4 V in 0.1 M H_2SO_4. At potentials between 0.4 V and 0.6 V adsorption/desorbtion of (bi)sulfates are observed.

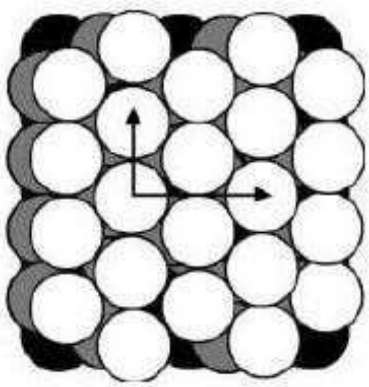

(b) The platinum (111) surface

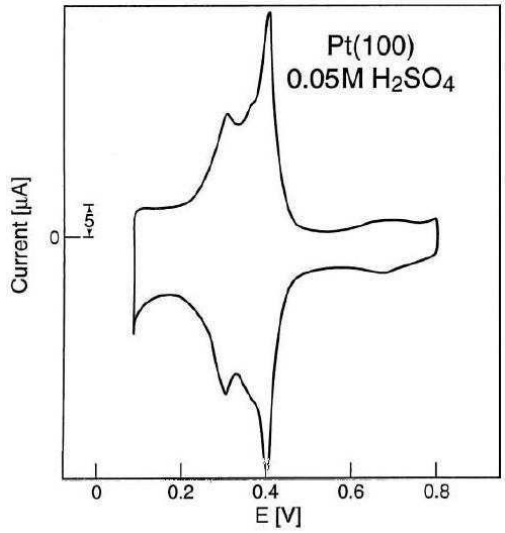

(c) Cyclic voltagram for a platinum (100) surface in H_2SO_4. Two well defined peaks at 0.4 and 0.25 V corresponding to the coupled processes of hydrogen adsorption and (bi)sulfate anion desorption.

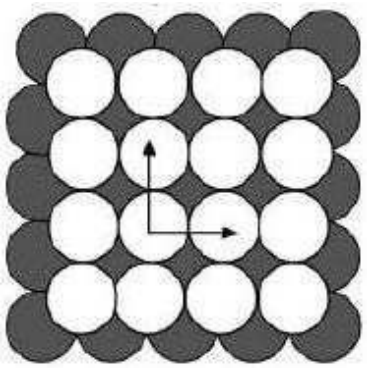

(d) The platinum (100) surface

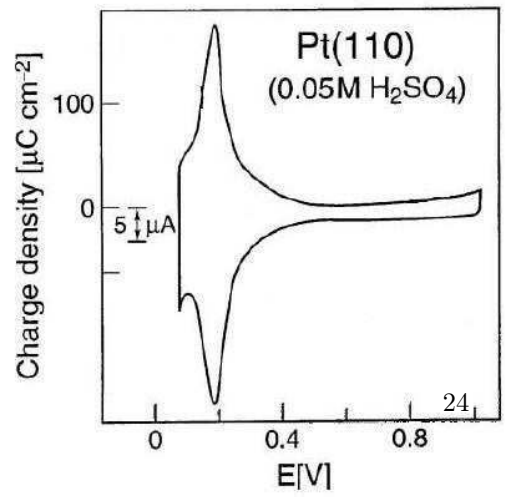

(e) Cyclic voltagram for a platinum (110) surface in H_2SO_4. The voltagram shows coupled processes for hydrogen adsorption/desorbtion with the hydroxyl anion adsorbtion/desorbtion at potentials between approximately 0.05 V and 0.35 V.

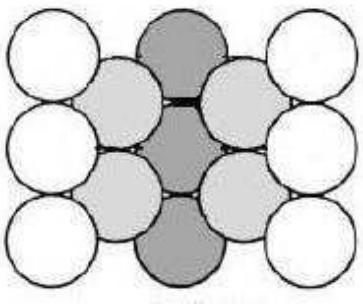

(f) The platinum (110) surface

Figure 3.7: Cyclic voltagrams and schematic drawings of platinum (111), (111) and (110) surfaces. Graphs adapted from [64].

a potential between 0.05 V and 0.25 V is immediately followed by adsorption of hydroxyl anions.
The cyclic voltagram for platinum (100) in 0.05 M H_2SO_4 shows coupled processes for hydrogen adsorption/desorbtion with the hydroxyl anion adsorbtion/desorbtion at potentials between approximately 0.05 V and 0.35 V. Similar voltagrams are observed for platinum (100) in $HClO_4$. [64].

3.3.1.3 Cyclic Voltagram of a MEA

Cyclic voltagrams have been recorded of MEAs by Chen *et al.* [65]. The cyclic voltagrams for MEAs are obtained by feeding hydrogen on the anode side and nitrogen on the cathode side. Hence, the anode will acts as the combined counter and reference electrode while the cathode is the working electrode in the three electrode setup. Figure 3.8 shows cyclic voltagrams for two MEAs with two different commercial catalysts used to manufacture them.

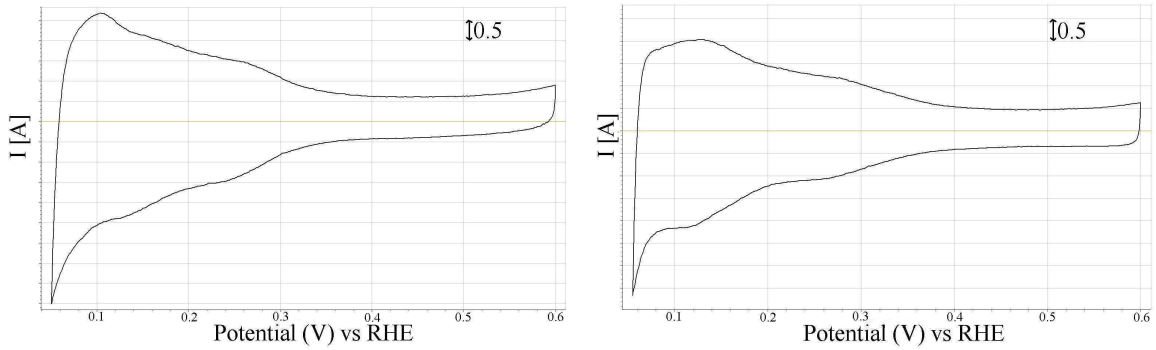

(a) Cyclic voltagram for commercial catalyst from Company 1. The voltagram shows hydrogen adsorption at a potential below 0.4 V.

(b) Cyclic voltagram for commercial catalyst from Company 2. The voltagram shows hydrogen adsorption at a potential below 0.4 V.

Figure 3.8: Cyclic voltagrams for two commercial catalysts. The MEA area is 180 cm^2 and the loading is 1.8 g/cm^2.

The cyclic voltagrams for the MEAs show hydrogen adsorption peaks at potentials below 0.4 V. The potential is limited to 0.6 V in order to protect the MEA form corrosion during the potential cycling. The area of the MEAs are 180 cm^2 and the loading of the MEAs are 1.8 g/cm^2. Generally, the MEAs manufactured at IRD fuel cells have utilization of the catalyst surface area of 20-30%. This leaves room for improvement of the utilization degree of the catalyst surface area.

A cyclic voltagram for platinum particles dispersed on a carbon surface contains contributions form all the different platinum planes.

Chapter 4

Identical location TEM studies of Pt/C electrocatalyst

It is important for new alloy catalysts to elucidate the mechanism for losing activity during the oxygen reduction reaction (ORR). By understanding the fundamentals behind catalyst instability it should be possible to develop new catalysts that are more corrosion resistant.
In the present work the experiments performed are mainly focussed on two issues, i.e. one is to elucidate the mechanism for platinum corrosion, the other is to establish a corrosion test method in which only the catalyst is tested and not the support of the particles.
The corrosion stability of a platinum gold catalyst was tested by Zhang *et al.* [31]. The catalyst was cycled between 0.6 V and 1.1 V for 30.000 cycles with a scan rate of 50 mVs^{-1}. This takes around 7 days. Thus, it is desirable to develop a corrosion test where the experiment time is reduced.
Mayrhofer *et al.* [66–68] have described an identical location transmission electron microscope technique. Using this technique they could image the same location of a sample before and after an electrochemical experiment. The experiments carried out by Mayrhofer *et al.* [67, 68] focussed on the size distribution of the platinum particles and corrosion of carbon. Degradation of the platinum catalyst was only observed when the samples were cycled to potentials of 1.4 V vs RHE. The catalyst degradation was subscribed to detachment of the particles from the support. The platinum particles investigated by Mayrhofer *et al.* [66] have an average size of 5.0 ± 0.1 nm .
In the present experiment described below the focus is on the corrosion of particles with an average size of approximately 2.3 ± 0.4 nm. The smaller particles are interesting because they are inherently less stable implying that their corrosion stability should be easier to observe. Furthermore, the smaller particle size is closer to the optimal size for maximum ORR mass activity. According to Gasteiger *et al.* [3] the optimal size for ORR mass activity is around 3 nm.
In the present experiment the identical location technique by Mayrhofer *et al.* [66–68] have been modified to use the TEM grid as the only working electrode in the three electrode setup. In the experiments carried out by Mayrhofer *et al.* the TEM grid was used in parallel with another working electrode. By using the TEM grid as the solo working electrode it is possible to make a more direct comparison between the electrochemical measurements and the TEM analysis.
By combining the corrosion test described by Zhang *et al.* [31] and the identical location transmission electron microscopy technique it is possible to investigate the corrosion of platinum particles supported by carbon in an environment that is similar to the start/stop of a fuel cell where the platinum particles are subjected to high potentials.

4.1 Method

The Pt/C catalyst was prepared by the inverse micelle method which gives a narrow particle size distribution [69, 70]. In short, the H_2PtCl_6 precursor (0.005 M Pt concentration) was introduced into a solution containing a micro-heterogeneous environment of droplet-like inverse micelles formed by the surfactant didodecyldimethyl ammonium bromide (DDAB), 5% DDAB in toluene. A solution of $LiBH_4$ in tetrahydrofuran was added in excess. The $LiBH_4$ is added while stirring to achieve a complete reduction of the platinum salt to metal particles inside the inverse micelles.
Following this a carbon black (Vulcan XC72, Cabot) - DDAB - toluene solution suspension was prepared, with the appropriate weight of carbon to obtain a final metal content of 10 wt%. The mixture was sonicated for 30 min which resulted in a homogenous suspension. Thereafter, the nano particle solution was slowly added to the carbon black suspension. After 4 h of stirring ethanol was added dropwise to the nanoparticle solution. Ethanol (99.9%) works as a destabilizing agent which breaks the droplet-like inverse micelle structure and precipitate the platinum particles. This solution was continuously stirred to avoid agglomeration of the particles. The mixture was allowed to settle overnight. The solid sample was recovered, and washed several times with ethanol by centrifugation and finally dried at 60°C overnight.

A BioLogic Instrument VMP2 potentiostat was used for the electrochemical experiments and a rotation disk electrode setup supplied by Pine Instrument Corporation. A standard three electrode setup was used. The electrolyte was 0.1 M $HClO_4$ (Aldrich, TraceSELECT Ultra) prepared using Millipore water (18.2MΩcm, TOC<5 ppb). The counter electrode was a carbon cloth and the reference was a $Hg/HgSO_4$ electrode. The reference electrode was separated form the working electrode by a ceramic frit.
The ink used in these experiments consist of isopropyl alcohol with a concentration of 1.5 $mg_{catalyst}mL^{-1}$. The ink had been sonicated for 30 min before 5 μL of the suspension was pippeted onto a lacey carbon 300 mesh on gold TEM grid.
The TEM grid was placed in direct contact with a glassy carbon electrode and this was used as the working electrode in the electrochemical experiments. Figure 4.1 shows the working electrode.

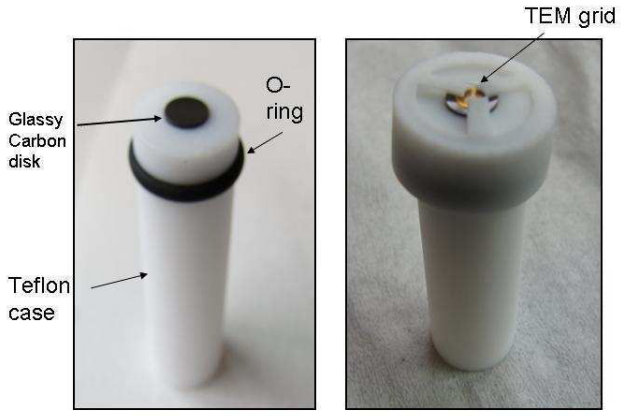

Figure 4.1: The working electrode used in the electrochemical experiments.

The corrosion effect on the platinum particles was elucidated by investigating the effect of scan rate, number of cycles and upper potential. In total five different experiments were carried out. The different experiments and the settings used are listed in Table 4.1.
Before and after the corrosion test the sample was investigated by TEM. Identical areas on the TEM grid was located by using the appropriate coordinates. The particle size distribution before and after the corrosion test is determined.

Table 4.1: The electrochemical settings for the five experiments preformed

Experiment	Potential	Scan rate	Cycles
1	0.6->1.1V	50 mVs^{-1}	3000 cycles
2	0.6->1.1V	200 mVs^{-1}	3000 cycles
3	0.6->1.2V	50 mVs^{-1}	3000 cycles
4	0.6->1.2V	200 mVs^{-1}	3000 cycles
5	0.6->1.1V	200 mVs^{-1}	30.000 cycles

Table 4.2: The electrochemical settings for the three thin film experiments preformed

Experiment	Potential	Scan rate	Cycles
1	0.6->1.1V	200 mVs^{-1}	3000 cycles
2	0.6->1.2V	200 mVs^{-1}	3000 cycles
3	0.6->1.1V	200 mVs^{-1}	30.000 cycles

4.1.1 Thin film experiments

The use of a TEM grid as a working electrode gives a more direct comparison between the electrochemical treatment and the TEM analysis. However, the loading of the TEM grid is too small to give a voltagram that could determined the electrochemically active surface. In over to support the results obtained by the TEM studies a traditional thin film experiment with a higher catalyst loading on the working electrode was performed.
An ink containing 1.8 mg catalyst per liter was fabricated by ultrasonic mixing of platinum on carbon catalyst with Milipore water, isopropyl alcohol and a 5 wt% Nafion solution. 20 μL of the suspension was pippetted onto a polished glassy carbon electrode. This glassy carbon electrode was used as the working electrode.
Three experiments were performed to verify the results obtained from the identical location TEM studies. The experiments are listed in Table 4.2.

4.2 Results

The results for the five experiments listed in Table 4.1 are treated in the same way. Figures 4.2, 4.3, 4.4, 4.5 and 4.6 show the identical location TEM images of the samples.

The particle size distribution has been calculated from both the identical locations and other locations to rule out the beam effect from the experiments. Figure 4.7 shows the particle size distributions for the platinum particles derived from the five experiments.
From the TEM images of experiment 1 shown in Figure 4.2 it is noted that there are some particle movement and mild sintering. These observations are supported by the particle size distribution.

The TEM images resulting from experiment 2 are shown in Figure 4.3. The images show some particle movement and mild sintering. Specific examples are marked with blue circles in Figure 4.3. These observations are supported by the particle size distribution shown in Figure 4.7(b).
Under the assumption that the particles are spherical it is possible to calculate the total platinum surface and volume area before and after the corrosion experiment from the identical location TEM images. This results in a reduction of the surface area of approximately 8% while the total volume of the platinum remains unchanged. The small reduction in surface area could manly be subscribed to particle coalescence. This is further supported by the oxygen reduction reaction (ORR) activity, which shows no significant deactivation.

The TEM images from experiment 3 is shown in Figure 4.4. The images show that the total number of particles have decreased and that there was some sintering of platinum particles. These phenomena are also

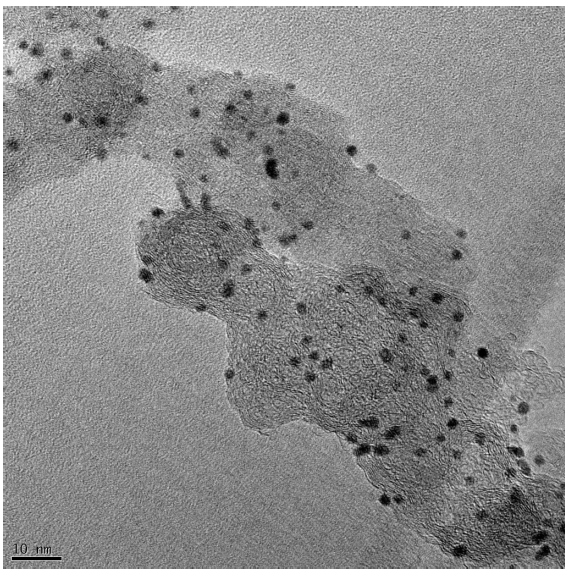

(a) TEM image of Pt/C before corrosion test. Image size: 113.023 nm × 113.023 nm

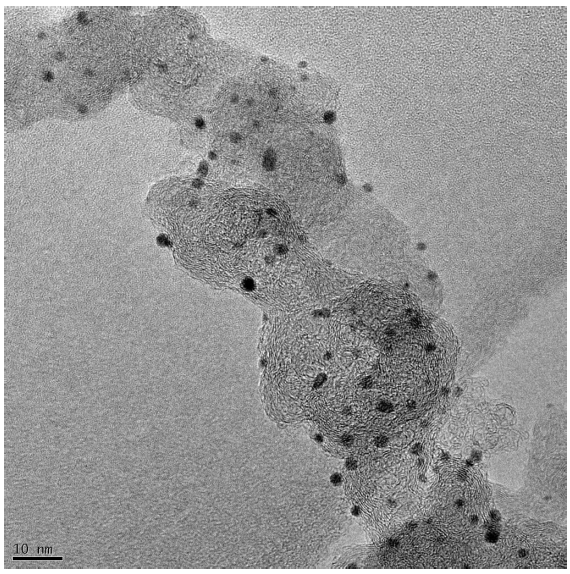

(b) TEM image of Pt/C after corrosion test, the location is identical to the location on TEM image (a). Image size: 113.023 nm × 113.023 nm

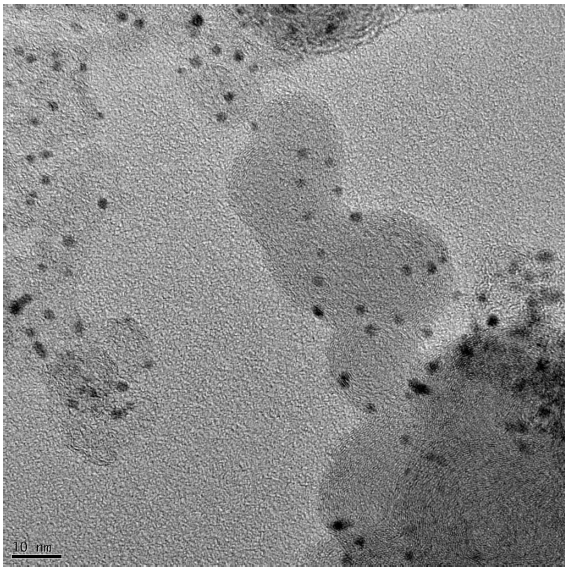

(c) TEM image of Pt/C before corrosion test. Image size: 113.023 nm × 113.023 nm

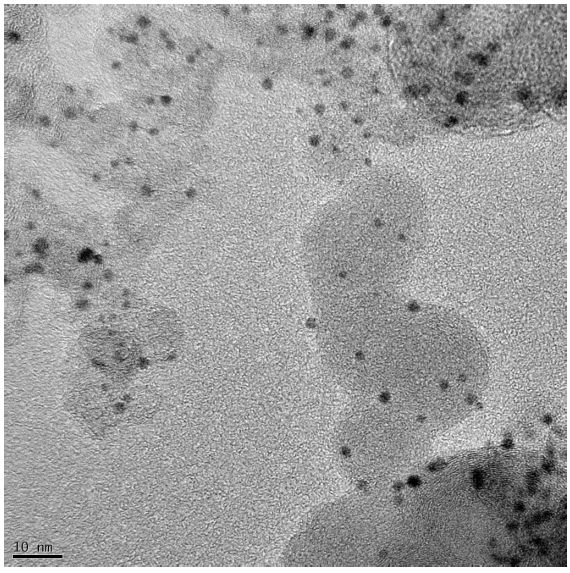

(d) TEM image of Pt/C after corrosion test, the location is identical to the location on TEM image (c). Image size: 113.023 nm × 113.023 nm

Figure 4.2: TEM images of Pt/C before and after corrosion test in experiment 1 in Table 4.1. The TEM images after the corrosion test show some particle movement and mild sintering.

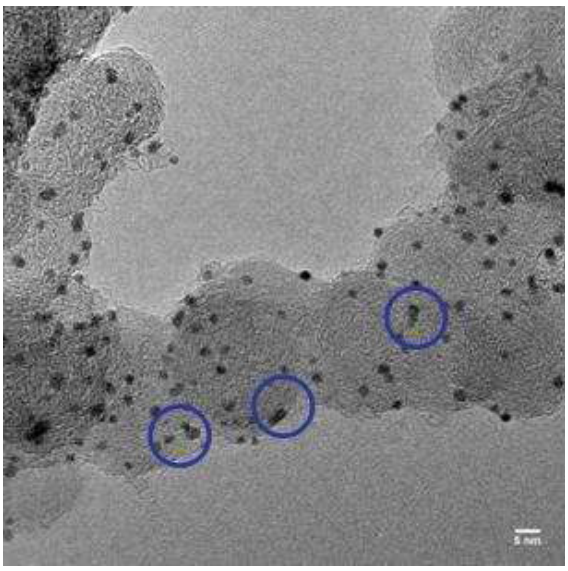

(a) TEM image of Pt/C before corrosion test. Image size: 113.023 nm × 113.023 nm

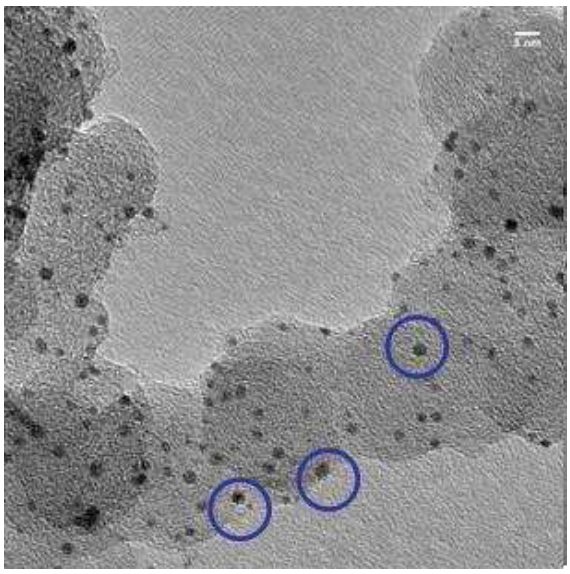

(b) TEM image of Pt/C after corrosion test, the location is identical to the location on TEM image (a). Image size: 113.023 nm × 113.023 nm

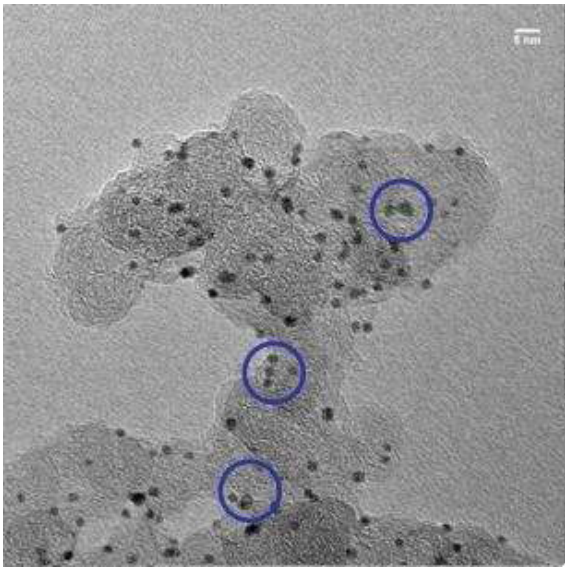

(c) TEM image of Pt/C before corrosion test. Image size: 113.023 nm × 113.023 nm

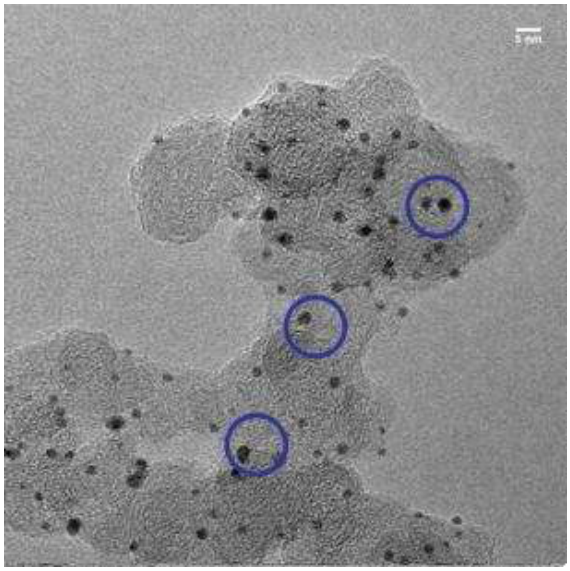

(d) TEM image of Pt/C after corrosion test, the location is identical to the location on TEM image (c). Image size: 113.023 nm × 113.023 nm

Figure 4.3: TEM images of Pt/C before and after corrosion test in experiment 2 in Table 4.1. The TEM images after the corrosion test show some particle movement and mild sintering, examples are marked with blue circles.

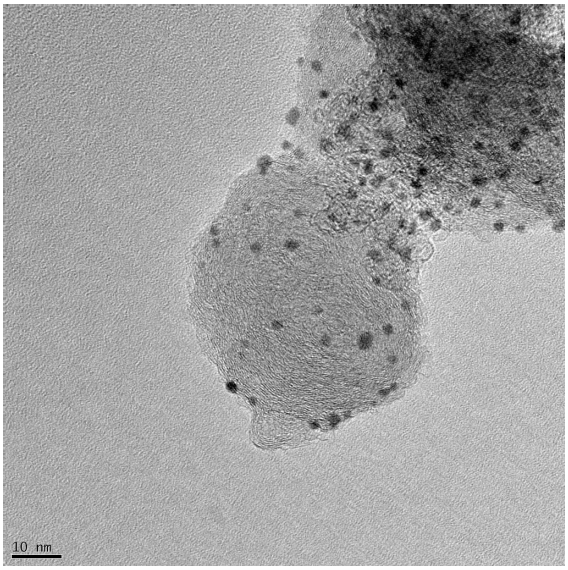

(a) TEM image of Pt/C before corrosion test. Image size: 113.023 nm × 113.023 nm

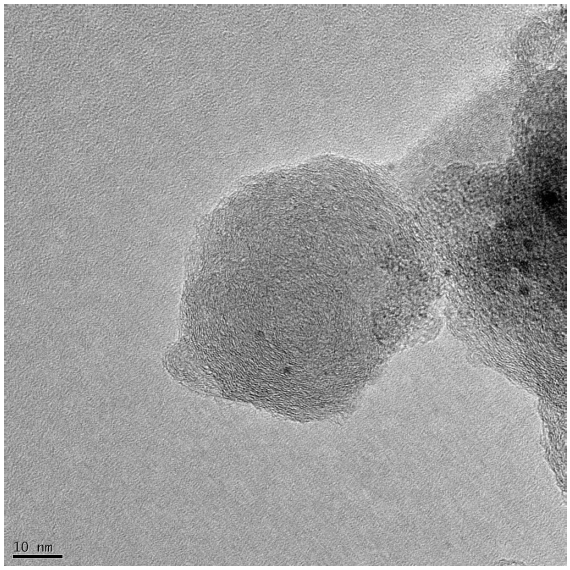

(b) TEM image of Pt/C after corrosion test, the location is identical to the location on TEM image (a). Image size: 113.023 nm × 113.023 nm

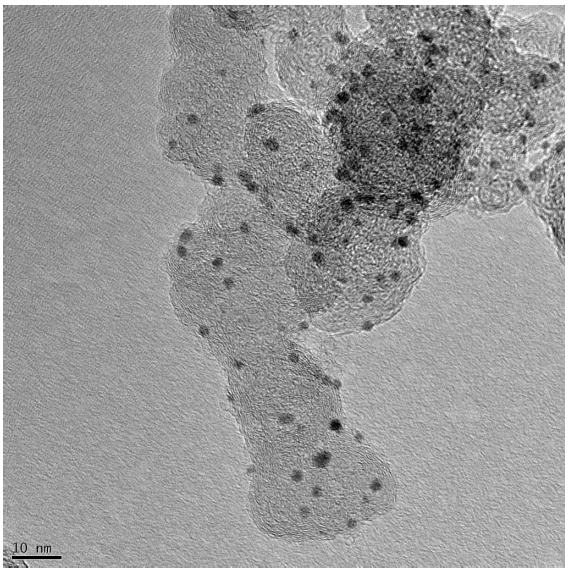

(c) TEM image of Pt/C before corrosion test. Image size: 113.023 nm × 113.023 nm

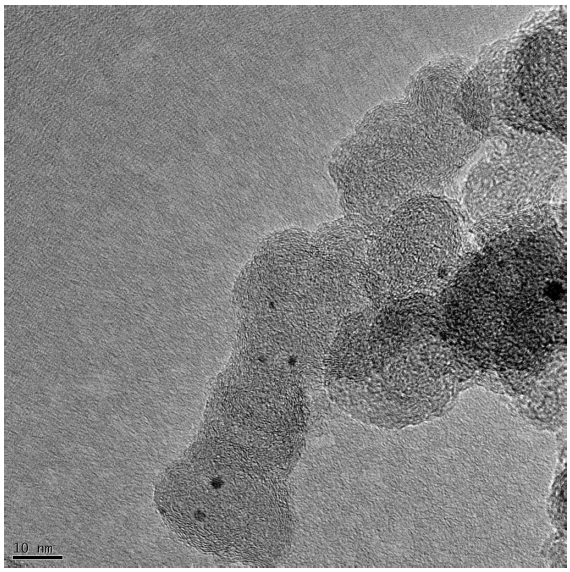

(d) TEM image of Pt/C after corrosion test, the location is identical to the location on TEM image (c). Image size: 113.023 nm × 113.023 nm

Figure 4.4: TEM images of Pt/C before and after corrosion test in experiment 3 in Table 4.1. The TEM images show that the total number of particles have decreased and that there was some sintering of platinum particles. The reduction in size and the disappearance of particles strongly suggest that platinum dissolves under the experimental conditions.

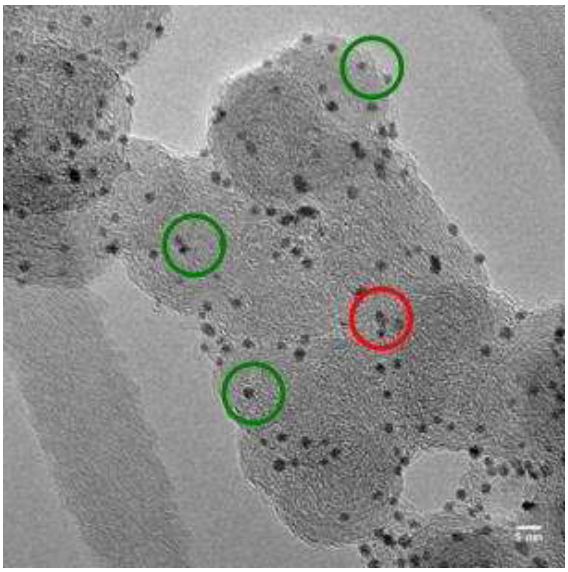

(a) TEM image of Pt/C before corrosion test. Image size: 113.023 nm × 113.023 nm

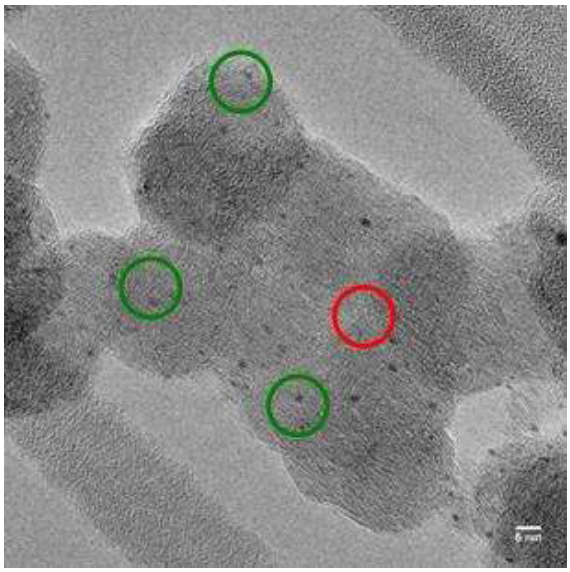

(b) TEM image of Pt/C after corrosion test, the location is identical to the location on TEM image (a). Image size: 113.023 nm × 113.023 nm

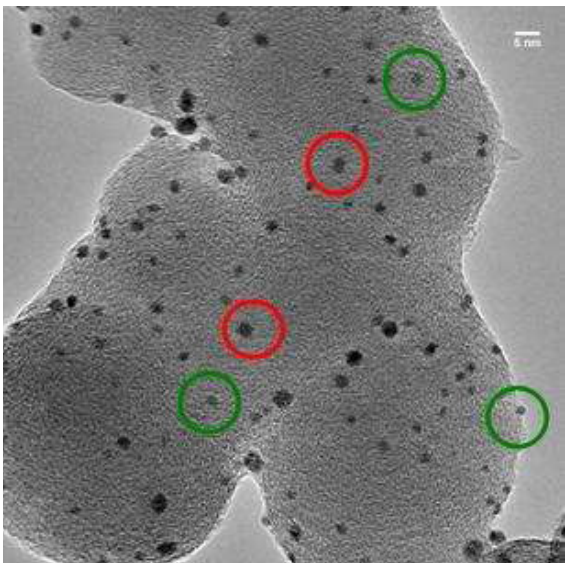

(c) TEM image of Pt/C before corrosion test. Image size: 113.023 nm × 113.023 nm

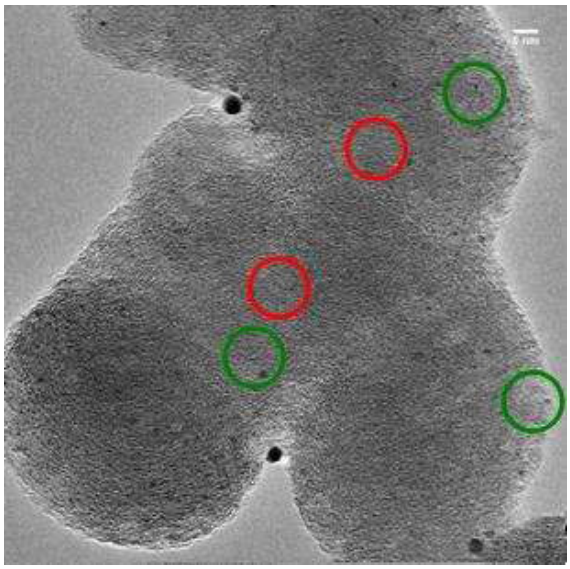

(d) TEM image of Pt/C after corrosion test, the location is identical to the location on TEM image (c). Image size: 113.023 nm × 113.023 nm

Figure 4.5: TEM images of Pt/C before and after corrosion test in experiment 4 in Table 4.1. The TEM images show that the total number of particles have decreased as result of the corrosion experiment. Some examples of particles disappearance are marked with red circles. Furthermore, reduction in size are observed, examples are marked with green circles. The reduction in size and the disappearance of particles strongly suggest that platinum dissolved under these experimental conditions.

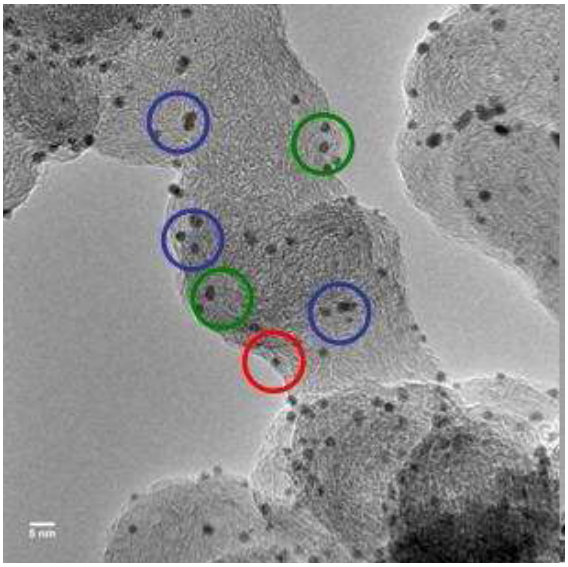

(a) TEM image of Pt/C before corrosion test. Image size: 113.023 nm × 113.023 nm

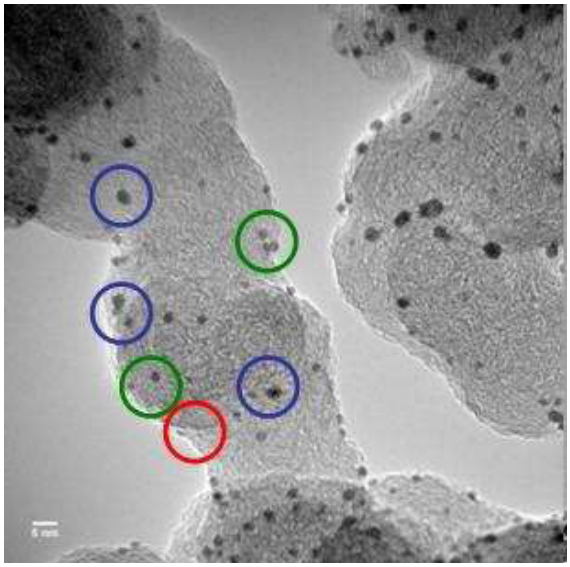

(b) TEM image of Pt/C after corrosion test, the location is identical to the location on TEM image (a). Image size: 113.023 nm × 113.023 nm

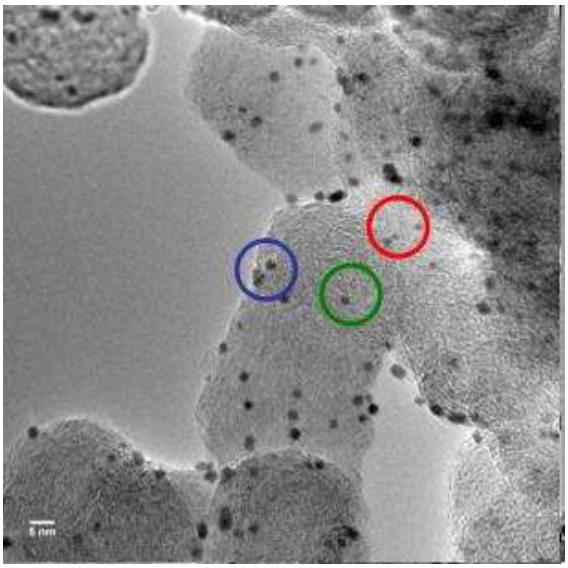

(c) TEM image of Pt/C before corrosion test. Image size: 113.023 nm × 113.023 nm

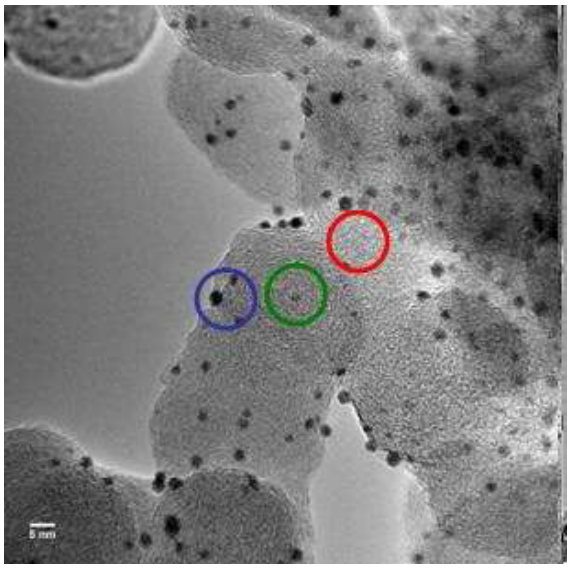

(d) TEM image of Pt/C after corrosion test, the location is identical to the location on TEM image (c). Image size: 113.023 nm × 113.023 nm

Figure 4.6: TEM images of Pt/C before and after corrosion test in experiment 5 in Table 4.1. The TEM images show that that there are some reduction in particle size indicated with green circles. Furthermore, disappearance of particles are observed this is marked with red circles. Mild sintering is marked with blue circles. The reduction in size and the disappearance of particles strongly suggest that platinum dissolved under these experimental conditions.

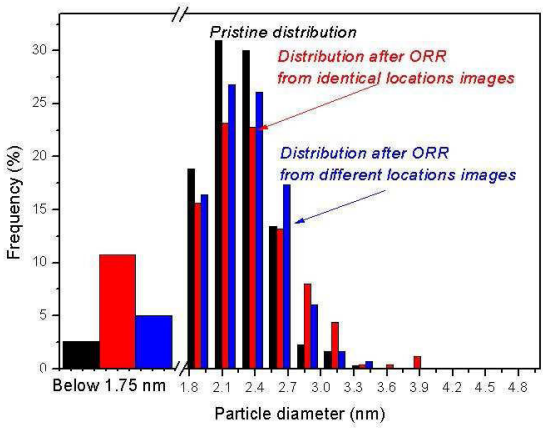

(a) The particle size distribution for the platinum particles in experiment 1 in Table 4.1. The black histogram is the distribution from pristine sample, particle count is 313. The red histogram is the distribution after accelerated corrosion test from identical locations, the particle count is 250. The blue histogram is the distribution after accelerated corrosion test from different locations, particle count 300

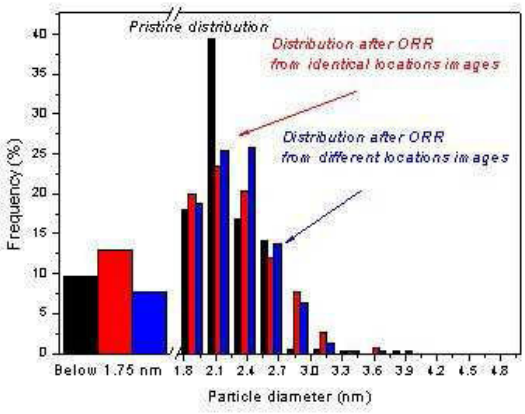

(b) The particle size distribution for the platinum particles in experiment 2 in Table 4.1. The black histogram is the distribution from pristine sample, particle count is 367. The red histogram is the distribution after accelerated corrosion test from identical locations, the particle count is 311. The blue histogram is the distribution after accelerated corrosion test from different locations, particle count 315

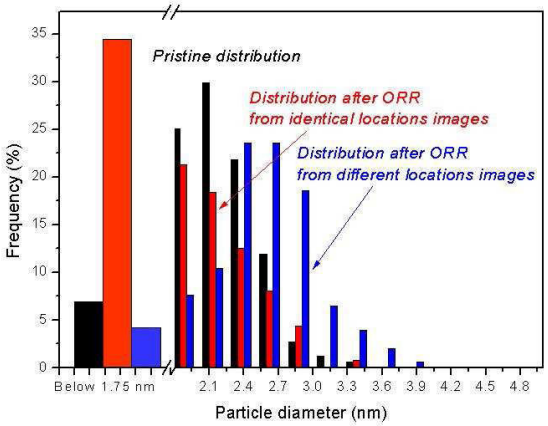

(c) The particle size distribution for the platinum particles in experiment 3 in Table 4.1. The black histogram is the distribution from pristine sample, particle count is 335. The red histogram is the distribution after accelerated corrosion test from identical locations, the particle count is 136. The blue histogram is the distribution after accelerated corrosion test from different locations, particle count 356

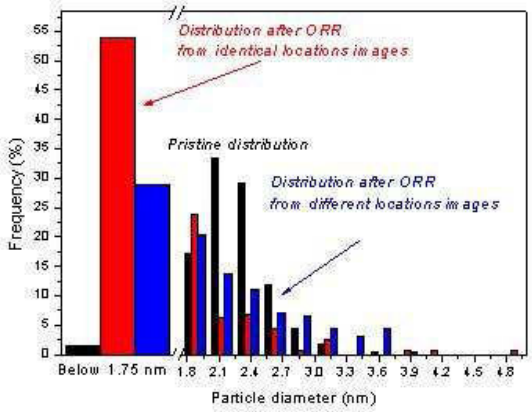

(d) The particle size distribution for the platinum particles in experiment 4 in Table 4.1. The black histogram is the distribution from pristine sample, particle count is 303. The red histogram is the distribution after accelerated corrosion test from identical locations, the particle count is 156. The blue histogram is the distribution after accelerated corrosion test from different locations, particle count 256

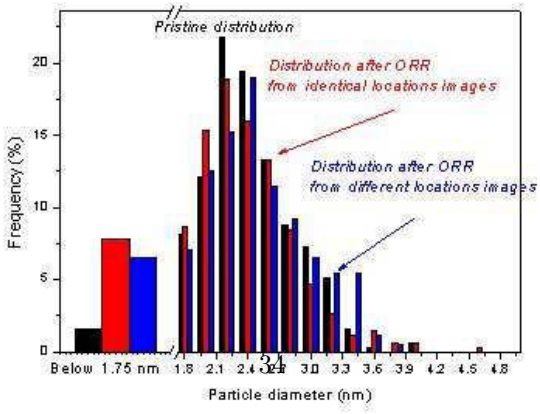

(e) The particle size distribution for the platinum particles in experiment 5 in Table 4.1. The black histogram is the distribution from pristine sample, particle count is 303. The red histogram is the distribution after accelerated corrosion test from identical locations, the particle count is 233. The blue histogram is the distribution after accelerated corrosion test from different locations, particle count 230

Figure 4.7: The particle size distribution from identical and different locations for the five experiments.

confirmed by the particle size distribution shown in Figure 4.7(c). The reduction in size and the disappearance of particles strongly suggest that platinum dissolves under the experimental conditions.

The TEM images of experiment 4 are shown in Figure 4.5. The images show that the total number of particles have decreased as result of the corrosion experiment. Some examples of particles disappearance are marked with red circles in Figure 4.5. Furthermore, it was observed from the images that the particles had decreased in size. Some examples of that are marked with green circles in Figure 4.5. These phenomena are also confirmed by the particle size distribution shown in Figure 4.7(d). Assuming the particles are spheres it is possible to calculate the total platinum surface area and volume before and after the corrosion experiment from the identical location TEM images. The results show that the corrosion has caused a decrease of approximately 60% in the surface area and volume of the platinum particles. The significant decrease of the platinum surface area observed can mainly be subscribed to dissolution of platinum particles. This is further supported by the oxygen reduction reactivity (ORR) results that were measured before and after the corrosion experiment. The ORR result shows a pronounced deactivation of 69 mV at the half wave potential, $\Delta E_{\frac{1}{2}}$.

The TEM images from experiment 5, shown in Figure 4.6, show some reduction in particle size as indicated with green circles in Figure 4.6. Furthermore, Figure 4.6 shows particle disappearance marked with red circles and mild sintering marked with blue circles. These phenomena are also confirmed by the particle size distribution shown in Figure 4.7(e). A decrease in the volume of platinum particles of approximately 30% and a decrease in the surface area of approximately 22% are observed. The reduction in size and the disappearance of particles strongly suggest that platinum particles dissolve under these experimental conditions. This is further supported by a reduction in the ORR activity of 35 mV at $\Delta E_{\frac{1}{2}}$.

In experiments 1, 2, 4 and 5 the particle size distributions from the identical and different TEM locations are roughly the same. This indicates that the beam effect on the sample are negligible.
In experiment 3 differences are observed in the particle size distributions resulting from identical location and different locations, respectively. However, since a high number of particles had disappeared altogether, the particle count from identical locations were much less then the particle count from different location. Thus, the results indicate that there are no beam effect.

4.2.1 Thin film experiment

In the thin film experiments the electrochemical active surface area was measured by cyclic voltametry before and after the corrosion experiments. The electrochemical results are shown in Figure 4.8.

4.3 Discussion

According to the identical location TEM results the degradation of the platinum on carbon catalyst used in these experiments are primarily due to platinum dissolution with mild sintering.

4.3.1 Effect of scan rate

Experiments 1 and 2 only differ by the scan rate. Therefore, the results of these experiments elucidate the effect of the scan rates. In experiment 1 the scan rate was 50 mVs^{-1} and in experiment 2 the scan rate was 200 mVs^{-1}. In both experiments the potential was cycled up to 1.1 V. In this potential window the same dissolution and mild sintering of platinum particles are observed and this indicate that the phenomena are independent of the scan rate.

To ensure that the potential window did not influence the results of the experiments the experiments were also carried out with a potential between 0.6 V and 1.2 V. These experiments confirm that the scan rate does not influence the results of the corrosion experiment.

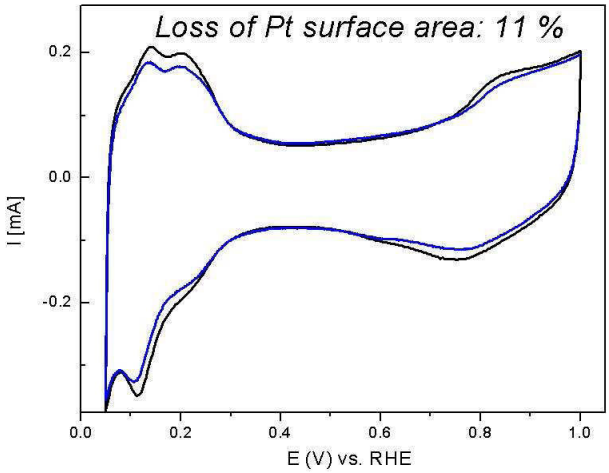

(a) Thin film experiment 1, Corrosion test: 3000 cycles between 0.6 V and 1.1 V, scan rate 200 mVs^{-1}

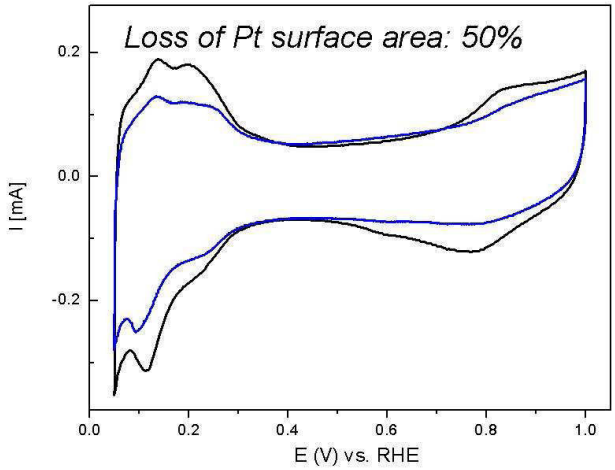

(b) Thin film experiment 2, Corrosion test: 3000 cycles between 0.6 V and 1.2 V, scan rate 200 mVs^{-1}

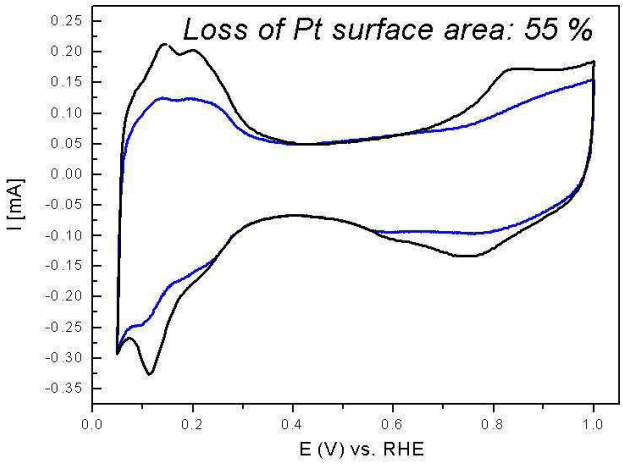

(c) Thin film experiment 3, Corrosion test: 30.000 cycles between 0.6 V and 1.1 V, scan rate 200 mVs^{-1}

Figure 4.8: Results from the three thin film corrosion experiments. The results from the thin film experiments are in excellent agreement with the results form the identical location TEM studies.

4.3.2 Effect of potential

Comparison of the results obtained in experiments 1 and 3 or in 2 and 4 shows that the upper voltage limit plays an important role during the accelerated corrosion test. Higher potential accelerates the dissolution of platinum particles. However, similar effects were observed when the sample was subject to potential cycling between 0.6 V and 1.1 V for 30.000 cycles.
In the literature there are experimental evidence suggesting that platinum dissolution should be enhanced considerably when the electrode is cycled to 1.2 V instead of 1.1 V [36]. This is in agrement with the results obtained in the present work.

4.3.3 Effect of number of cycles

Comparison of experiments 2 and 5 reveals that the platinum dissolution is much more pronounced when the platinum particles are cycled 30.000 times between 0.6 V and 1.1 V then when they are cycled 3000 times. When the platinum particles are subjected to 30.000 cycles the dissolution approach the dissolution observed at higher potential limits.

4.3.4 Comparison of results obtained from corrosion experiments

The thin film measurement of the platinum particles, experiment 2, showed that the samples cycled up to 1.2 V for 3000 cycles had a loss in surface area of approximately 50%. In comparison the identical location TEM study presented in experiment 4 showed a reduction of surface area of approximately 60%.
The thin film experiment 1 showed that the platinum particles cycled between 0.6 V and 1.1 V for 3000 cycles lost approximately 11% of the electrochemical active surface area. In comparison the identical location TEM study, experiment 2, showed a decrease in the surface area of approximately 10%. Thus, the results of these two types of experiments are in excellent agrement.
In the thin film experiment 3 where the sample was cycled between 0.6 V and 1.1 V 30.000 times showed a decrease in the electrochemical active surface area of 55% was observed. This is much larger then the decrease of approximately 30% obtained in the identical location TEM experiment 5. The observed difference could be caused by the differences in the volume of catalyst material used in the two types of experiments.

4.4 Conclusion

The platinum catalyst was subject to potential cycling simulating the start up and shut down of a fuel cell. All of the results obtained showed that electrochemical dissolution of platinum particles is the major factor limiting the catalytic durability towards potential cycling for extended time.
The corrosion of the platinum particles was accelerated when the potential was increased from 1.1 V to 1.2 V. The same effect was observed when the upper limit was 1.1 V and the sample was cycled for 30.000 times.

Chapter 5

Degradation study of Pt/C commercial electrocatalysts during oxygen reduction reaction

The corrosion stability of three commercial catalysts are studied and compared to each other. The method established in Section 4.4 is used to study the corrosion stability of the commercial catalysts. In addition, the catalysts are characterized by TEM.
The study of the three commercial catalysts are carried out to establish a baseline for the alternative catalysts synthesized during the project.

5.1 Method

An ink consisting of 2.5 mg of the catalyst and 800 μL demineralized water (33 MΩcm), 200 μL isopropanol (99%) and 20 μL of 5 wt% Nafion in demineralized water (33 MΩcm) was dispersed ultrasonically for 45 min.
10 μL of the ink is pippetted onto the glassy carbon that is used as the working electrode and thereafter the solvents are evaporated. The glassy carbon electrode is transferred into the electrochemical setup.
The electrochemical experiments were performed with BioLogic Instrument SP150 potentiostat. The electrochemical setup described in Section 3.3 was used. The electrolyte, 0.1 M $HClO_4$ (Sigma-Aldrich, ACS reagent, Puriss, p.a.) was prepared using demineralized water (33 MΩcm). A platinum wire was used as the counter electrode and the reference electrode was $Hg/HgSO_4$. Both were separated from the electrolyte by a ceramic frit. All measurements were carried out at 34°C.
For the corrosion test the working electrode was cycled in a oxygen saturated electrolyte between 0.6 V vs RHE and 1.2 V vs RHE, without rotation and with a scan rate of 200 mVs^{-1} for 3000 cycles.
The electrochemical active surface area was measured by cyclic voltametry before and after the corrosion experiment in a nitrogen saturated electrolyte between 0.09 V vs RHE and 1.1 V vs RHE, without rotation and with a scan rate of 20 mVs^{-1}.
To establish the size of the nanoparticles the catalysts are investigated with TEM, as described in Section 3.1.5.

5.2 Results

The data obtained from three catalysts were treated identically for direct comparison to each other. The TEM images of the three commercial catalysts are shown in Figures 5.1, 5.2, and 5.3.
As noted from Figure 5.3 the platinum particles supplied by Company 3 were not well dispersed on the

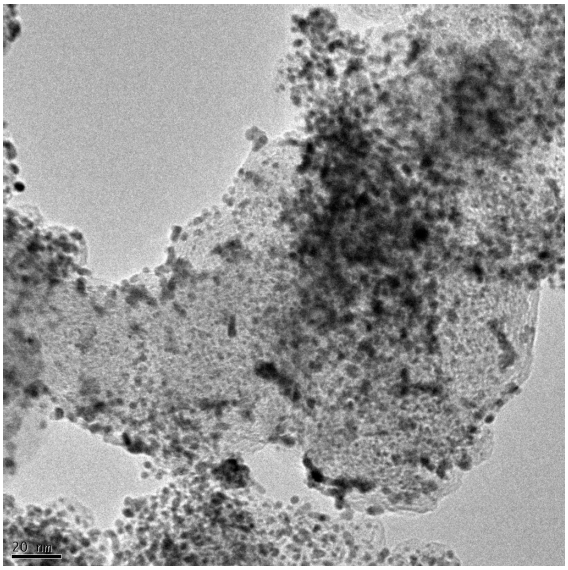

(a) TEM image of Company 1 catalyst. Image size: 227.15 nm × 227.15 nm

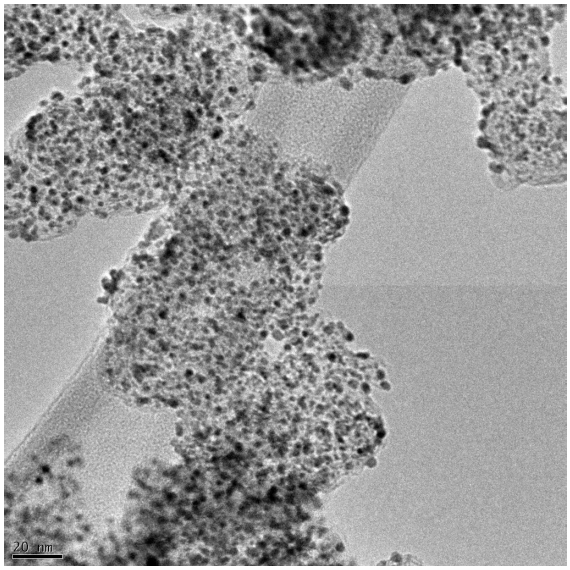

(b) TEM image of Company 1 catalyst. Image size: 227.15 nm × 227.15 nm

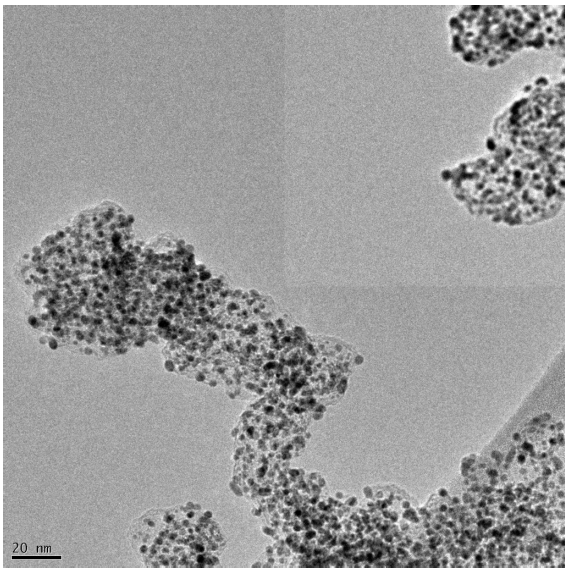

(c) TEM image of Company 1 catalyst. Image size: 227.15 nm × 227.15 nm

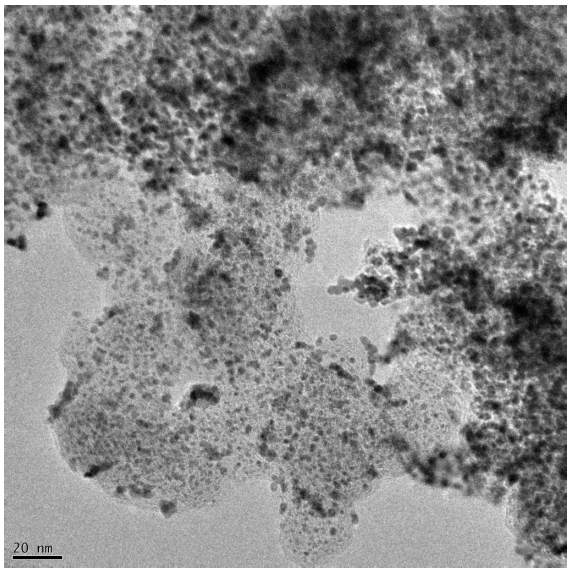

(d) TEM image of Company 1 catalyst. Image size: 227.15 nm × 227.15 nm

Figure 5.1: TEM images of different areas of Company 1 catalyst before corrosion experiment. The distribution of the platinum particles vary in some areas the particles are uniform in size and they are uniformly distributed on the support. In other areas, images (a) and (d), the particles are not uniformly distributed on the support and the size of the particles vary.

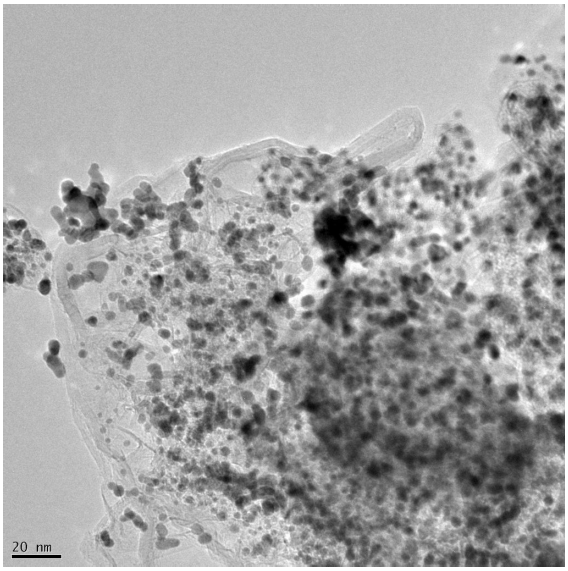

(a) TEM image of Company 2 catalyst. Image size: 227.15 nm × 227.15 nm

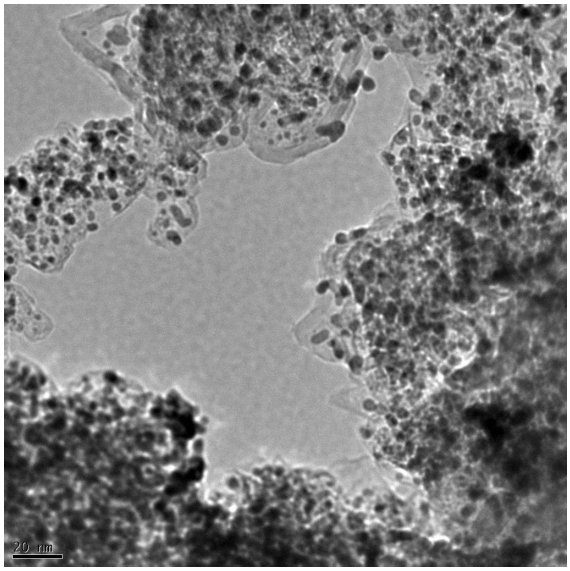

(b) TEM image of Company 2 catalyst. Image size: 227.15 nm × 227.15 nm

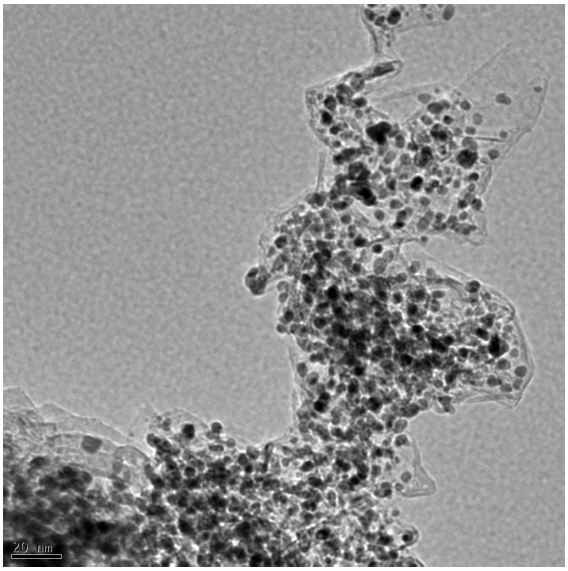

(c) TEM image of Company 2 catalyst. Image size: 227.15 nm × 227.15 nm

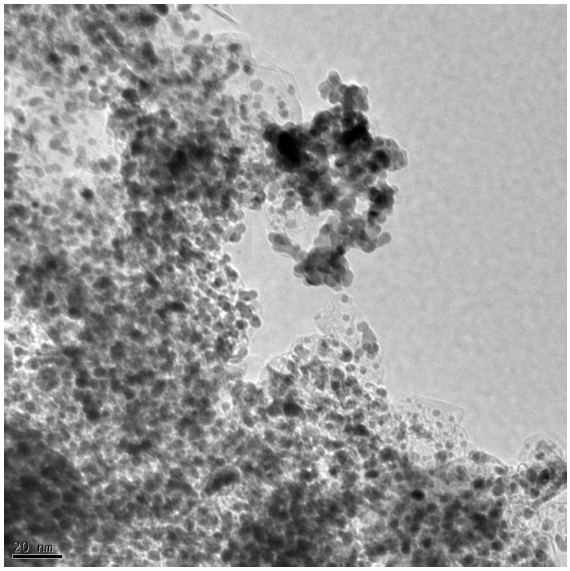

(d) TEM image of Company 2 catalyst. Image size: 227.15 nm × 227.15 nm

Figure 5.2: TEM images of different areas of Company 2 catalyst before corrosion test. It is observed that the platinum particles are of uniform size and shape. Futhermore, they are uniformly distributed on the carbon support.

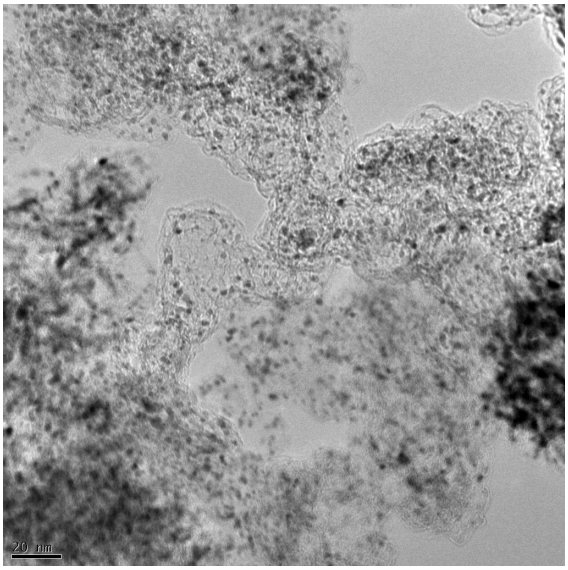

(a) TEM image of Company 3 catalyst. Image size: 227.15 nm × 227.15 nm

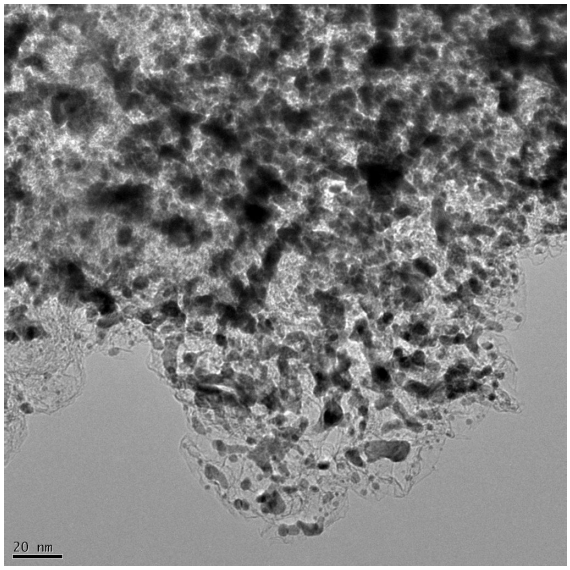

(b) TEM image of Company 3 catalyst. Image size: 227.15 nm × 227.15 nm

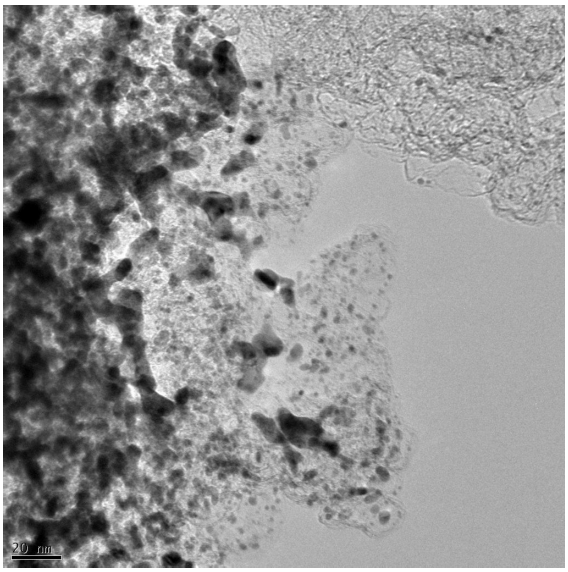

(c) TEM image of Company 3 catalyst. Image size: 227.15 nm × 227.15 nm

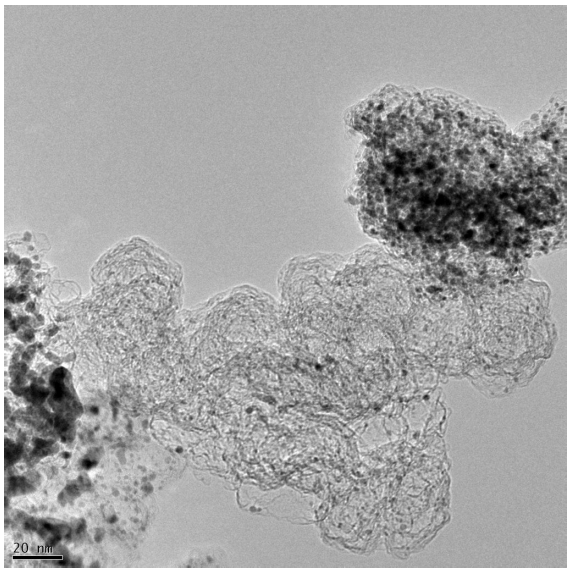

(d) TEM image of Company 3 catalyst. Image size: 227.15 nm × 227.15 nm

Figure 5.3: TEM images of different areas of Company 3 catalyst before corrosion test. The Figures show that the platinum particles are not uniformly distributed on the carbon support. There are areas where the platinum particles agglomerate, image (b) and (c). Furthermore, there are areas where the loading of platinum particles is very low, image (a) and (d).

carbon support. Therefore, the TEM images from the catalyst manufactured by Company 3 could not be analyzed according to the method described in Section 3.1.5. Hence, the particle size distribution for the platinum particles from Company 3 could not be established.
The TEM images were analyzed according to the method described in Section 3.1.5. A histogram of the size distributions for catalysts from Company 1 and Company 2 are shown in Figure 5.4.

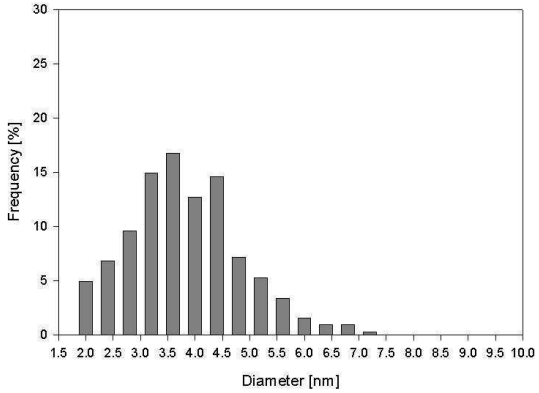

(a) The particle size distribution of Company 1 catalyst before corrosion experiment. The average diameter of the platinum particles are 3.6 ± 1 nm, this is close to the maximum of the particle size distribution. Particle count is 332.

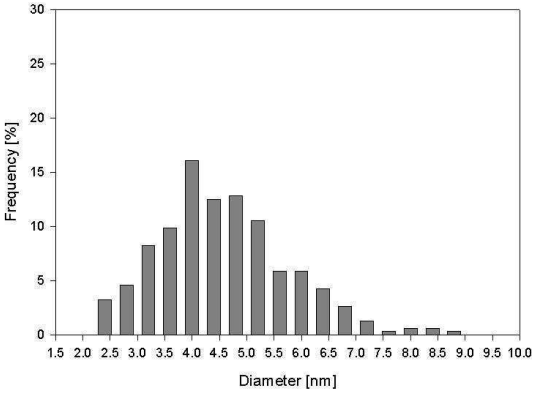

(b) The particle size distribution of Company 2 catalyst before corrosion experiment. The average diameter of the catalyst is 4.4 ± 1.2 nm hence the average diameter is a bit larger then the maximum point of the distribution, this could be caused by a over estimation of the diameter when the particles are measured using TEM. Particle count is 304.

Figure 5.4: Particles size distribution for the Company 1 and Company 2 catalysts.

The average particle diameter obtained from TEM and obtained by the manufacture from XRD for the three commercial catalysts are shown in Table 5.1. Company 1 has specified that the diameter of their catalyst particles measured by XRD should be less then or equal to 3.0 nm. From Table 5.1 it is noted that the average diameter measured by XRD is 3.2 nm. Thus, the catalyst from Company 1 does not comply with the specifications given. This, however, does not have influence on the results of the present study.

Table 5.1: The average diameters for the three commercial catalysts

Catalyst	Loading	Average TEM diameter [nm] (Present work)	Average XRD diameter [nm] (Stated by the manufactures)
Company 1	56.8 wt%	3.6 ± 1 nm	3.2 nm
Company 2	57.9 wt%	4.4 ± 1.2 nm	3.8 nm
Company 3	65 wt%	Not measurable	4 nm

The total theoretical surface area of the platinum particles can be calculated under the assumption that the particles are spherical. This have been carried out on basis of the results obtained from the TEM measurements and also from the XRD data provided by the manufactures. The details of these calculations are given in Appendix A. The theoretical calculated surface areas for the three catalysts are shown in Table 5.2.
The catalysts were subject to an accelerated corrosion experiment according to the description in Section 5.1. Cyclic voltagrams were recorded between 0.09V vs RHE and 1.1V vs RHE. The voltagrams for the three catalysts are shown in Figure 5.5.
The electrochemical active surface area of the platinum particles before and after corrosion can be calculated

Table 5.2: Theoretical calculated surface areas for the three commercial catalysts

Catalyst	Theoretical surface area obtained from TEM data	Theoretical surface area obtained from XRD data
Company 1	10.8 cm^2 $^{+4.2cm^2}_{-2.3cm^2}$	12.2 cm^2
Company 2	9 cm^2 $^{+3.4cm^2}_{-1.9cm^2}$	10.5 cm^2
Company 3	Not measurable	11.5 cm^2

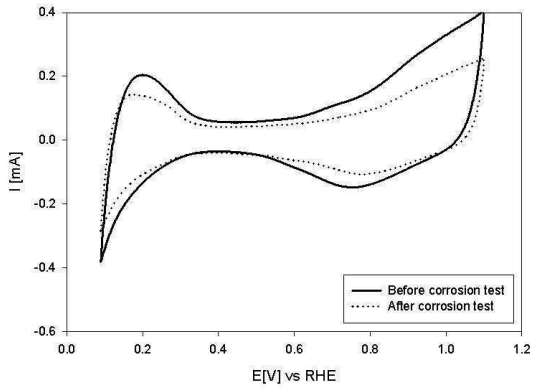

(a) Cyclic voltagram of Company 1 catalyst before (solid line) and after (dotted line) accelerated corrosion experiment. The utilization of the platinum surface area is 43% before the corrosion test. The electrochemical active surface area decreases to 28% after the corrosion test.

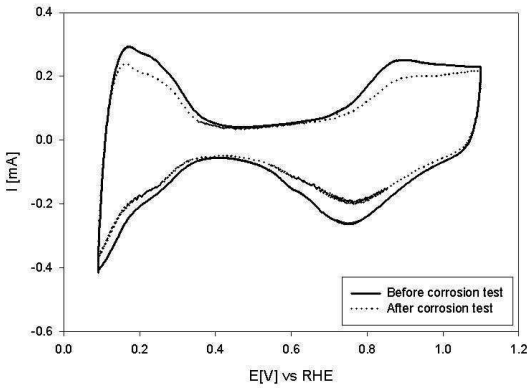

(b) Cyclic voltagram of Company 2 catalyst before (solid line) and after (dotted line) accelerated corrosion experiment. The utilization of the platinum surface area before the corrosion test is 96%. After the corrosion test the electrochemical active area is reduced to 73%.

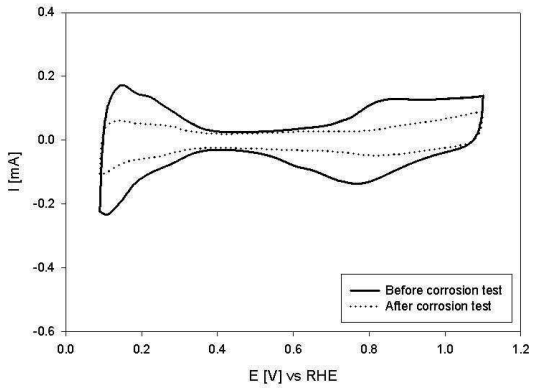

(c) Cyclic voltagram of Company 3 catalyst before (solid line) and after (dotted line) accelerated corrosion experiment. The electrochemical active area before the corrosion test is 48%. The electrochemical active surface area is reduced to 14% after the corrosion test.

Figure 5.5: Cyclic voltagram before and after corrosion test for the three commercial catalysts.

using the hydrogen under potential deposition (Hupd) area and the equivalence $210\frac{\mu C}{cm^2}$ platinum as described in Section 3.3. The electrochemical active areas are listed in Table 5.3.

Table 5.3: The electrochemical surface activity for the three commercial catalysts before and after accelerated corrosion experiment and compared to the theoretical surface areas calculated from TEM and XRD data.

Catalyst	Before (TEM)	Before (XRD)	After (TEM)	After (XRD)
Company 1	$43\ ^{+19\%}_{-8\%}$	43%	$28\%\ ^{+12\%}_{-5\%}$	28%
Company 2	$111 \pm 30\%$	96%	$85\% \pm 23\%$	73%
Company 3	Not measurable	48%	Not measurable	14%

5.3 Discussion

As shown in Table 5.1 the average particles diameters of the three commercial catalysts do not differ significantly.
From the TEM images shown in Figure 5.2 it is noted that the Company 2 catalyst particles have uniform sizes and uniform shapes. Furthermore, the particles are uniformly distributed on the carbon support. The TEM images shown in Figure 5.1 from Company 1 catalyst show platinum particles that are unevenly distributed in some areas of the carbon support. Furthermore, in some areas the particles vary in size. In the TEM images shown in Figure 5.3 of the Company 3 catalyst mixtures of large and small particles are observed. Thus, the distribution of the platinum particles in the Company 3 catalyst is not uniform, there are large areas without particles as well as areas with agglomeration of particles. The platinum loading in the three catalysts are similar. The difference in the distributions of the platinum particles may be due to differences in the surface areas of the carbon support used in the three catalysts.

Table 5.3 shows the Electrochemical active surface areas for the three commercial catalysts. From Table 5.3 it is noted that the utilization of the Company 2 catalyst is very high and that it maintains a high surface activity after the corrosion experiment. This is not the case for the Company 1 and Company 3 catalysts, both of them have a utilization of the surface area below 50% and their surface activity after the corrosion experiment is further reduced.
Table 5.3 shows that the electrochemical active surface area of the catalyst from Company 2 is larger than the 100% of the theoretical surface area when calculated from the TEM data. This implies that the average diameter measured with TEM is overestimated. This postulate is supported by the particle size distribution shown in Figure 5.4(a), from which it is noted that the particle size distribution it not a perfect Gaussian distribution. Hence, the average diameter is shifted towards the high end of the distribution.
In addition Table 5.3 shows that the measured electrochemical active surface area for the Company 2 catalyst is very close to the theoretical value obtained from XRD characterization. This indicates a high utilization of the Company 2 catalyst presumably caused by low agglomeration of the nanoparticles on the carbon support.
The difference in the electrochemical surface area activity of the three commercial catalysts investigated could be due to differences in the platinum particle size distributions and/or to differences in the distribution of platinum particles on the carbon support. Furthermore, the differences could be caused by the difference in the carbon supports. The manufactures of the catalysts do not state the surface areas of the carbon supports.
The hypothesis regarding differences in the carbon supports and the dispersion of the platinum particles on the carbon supports are further supported by recent work of Liu *et al.*. [71]. Liu *et al.* have shown that platinum particles are more uniformly dispersed on high surface area carbon support, resulting in higher platinum surface area available for the oxygen reduction reaction. This is also supported by Janssen *et al.* [59] who have shown that the Company 1 catalyst has a higher utilization of the platinum surface area then platinum supported by vulcan XC72.

Another difference between the catalysts investigated is the average diameter of the platinum particles. The Company 1 and Company 3 catalysts are both equal to or below 4 nm while the Company 2 catalyst is around 4.4 nm. This rather small difference could according to Tang *et al.* [34] result in different corrosion paths, therefore a different corrosion stability. According to Tang *et al.* [34] particles that have diameters less then 4 nm dissolve via direct electrochemical dissolution pathways while larger particles form an oxide at the same potential. Hence, larger particles are more corrosion stable.

The corrosion stability obtained for the three commercial catalysts can be compared to the corrosion stability study reported by Zhang *et al.* [31]. Zhang *et al.* tested platinum particles supported by carbon (Pt/C) and platinum with 10-11% gold (AuPt/C) supported by carbon. The corrosion test used by Zhang *et al.* consisted of 30.000 cycles from 0.6 to 1.1 V under oxidizing conditions. They measured the electrochemical active surface area before and after the corrosion experiment. The corrosion test employed in the present study involves 3.000 cycles from 0.6 to 1.2 V under oxidizing conditions. From the identical location study performed it has been established that platinum particles supported by carbon cycled between 0.6 V and 1.1 V 30.000 times gives similar results as when platinum particles supported by carbon are cycled between 0.6 V to 1.2 V 3.000 times. On this background the results obtained in the present investigation are comparable to the results reported by Zhang *et al.* The remaining electrochemical activities of the three catalysts investigated in the present work are compared to the data from Zhang *et al.* in Table 5.4.

Table 5.4: The remanning electrochemical activities after corrosion test of the three commercial catalysts tested in the present work and the catalysts from Zhang *et al.* [31].

Catalyst	Remanning electrochemical activity (XRD data used)
Company 3	29%
Company 2	77 %
Company 1	65 %
Pt/C from [31]	55%
AuPt/C from [31]	96%

From the remanning electrochemical activities shown in Table 5.4 it is noted that the Company 1 and the Company 2 catalysts have higher corrosion stability than the Pt/C tested by Zhang *et al.* [31]. It is noted that the Company 3 catalyst only has 29% remanning activity after the corrosion test. Non of the commercial catalysts have the same corrosion stability as the AuPt/C sample tested by Zhang *et al.* [31].

5.4 Conclusion

The three commercial catalysts that have been investigated in the present work have different corrosion stabilities even thought they have similar data specifications. From an industrial point of view it is interesting that the Company 2 catalyst is more corrosion stable and has higher utilization of the platinum surface area than the Company 1 and the Company 3 catalysts.
The differences in the corrosion stabilities could be attributed to differences in the carbon supports, differences in the platinum particle size or differences in the distribution of platinum particles on the carbon support.

The corrosion experiments based on the commercial catalysts have been reproduced several times and the same trends have been observed.

Chapter 6

Degradation Study of PtAu/C electrocatalysts during oxygen reduction reaction

Recently Zhang *et al.* [31] showed that 3 to 5 nm platinum particles with gold supported on carbon are more stable toward corrosion than pure platinum particles of the same size supported on carbon. The gold was deposited on the platinum particles via underpotential deposition of copper. The copper layer was galvanic displaced by gold.
According to the results obtained by Zhang *et al.* [31] gold has a stabilizing effect on platinum particles against corrosion.
In the present work an experiment was performed to elucidate the possible stabilizing effect of gold deposited on the platinum particles. Four samples were prepared and investigated i.e. platinum particles on carbon support (Pt), one third mono layer gold on platinum particles supported by carbon (Pt_1/3), two third mono layer gold on platinum particles supported by carbon (Pt_2/3) and finally one mono layer gold on platinum particles supported by carbon (Pt_1). The four samples were characterized by TEM before carrying out the corrosion experiments. The electrochemical stabilities of the samples toward corrosion were tested by the method described in Chapter 4.

6.1 Method

6.1.1 Syntheses of the samples

The Pt/C catalyst was prepared by the inverse micelle method which gives a narrow particle size distribution [69, 70]. In short, the H_2PtCl_6 precursor (0.005 M Pt) was introduced into a solution containing a micro-heterogeneous environment of droplet-like inverse micelles formed by the surfactant didodecyldimethyl ammonium bromide (DDAB), 5% DDAB in toluene was used. Thereafter, $LiBH_4$ in tetrahydrofuran solution was added in excess. For the Pt sample the $LiBH_4$ solution was added while stirring to achieve a complete reduction of the platinum particles.
For the platinum gold samples a gold-precursor $HAuCl_4$ was introduced into a 5% DDAB in toluene solution. The gold-precursor was added dropwise to the platinum solution. The amount of gold added to the platinum was calculated to reach a final coverage of the platinum particles of 1/3, 2/3 and 1 mono layer of gold, respectively. Simultaneously with the gold-precursor the reducing $LiBH_4$ solution was added.

A carbon black (Vulcan XC72, Cabot) - DDAB - toluene solution suspension was prepared, with the appropriate weight of carbon to obtain a final metal content of 10 wt%. The mixture was sonicated for 30 min

which resulted in a homogenous suspension. Thereafter, the nano particle solution was slowly added to the carbon black suspension. After 4 h of stirring ethanol was added dropwise to the nanoparticles. Ethanol acts as a destabilizing agent which breaks the droplet-like inverse micelle structures and precipitates the platinum particles. The solution was continuously stirred to avoid agglomeration of the particles. The mixture was allowed to settle overnight. The solid sample was recovered, and washed several times with ethanol by centrifugation and finally dried at 60°C overnight.

6.1.2 Characterization of the samples

The samples were characterized by TEM to establish the nanoparticle size distribution. This was carried out according to the method described in Section 3.1.5.

6.1.3 Electrochemical experiments

An ink consisting of 2.5 mg of the catalyst and 800 μL demineralized water (33 MΩcm), 200 μL isopropanol (99%) and 20 μL of 5 wt% Nafion in demineralized water (33 MΩcm) was dispersed ultrasonically for 45 min.
20 μL of the ink was pippetted onto the glassy carbon that was used as the working electrode and thereafter the solvents were evaporated. The glassy carbon electrode was transferred into the electrochemical setup.
The electrochemical experiments were performed with BioLogic Instrument SP150 potentiostat. The electrochemical setup described in section 3.3 was used. The electrolyte, 0.1 M $HClO_4$ (Sigma-Aldrich, ACS reagent, Puriss, p.a.) was prepared using demineralized water (33 MΩcm). A platinum wire was used as the counter electrode and the reference electrode was $Hg/HgSO_4$. Both were in contact with the electrolyte through a ceramic frit. All measurements were carried out at 34°C.
For corrosion test the working electrode was cycled in a oxygen saturated electrolyte between 0.6 V vs RHE and 1.2 V vs RHE, without rotation and with a scan rate of 200 mVs^{-1} for 3000 cycles.
The electrochemical active surface area was measured by cyclic voltametry before and after the corrosion experiment in a nitrogen saturated electrolyte between 0.09 V vs RHE and 1.1 V vs RHE, without rotation and with a scan rate of 20 mVs^{-1}.

6.2 Results

Figures 6.1, 6.2, 6.3 and 6.4 show the TEM images of the sample platinum on carbon support (Pt), one third monolayer of gold on platinum supported by carbon (Pt_1/3), two third monolayer of gold on platinum supported by carbon (Pt_2/3) and one monolayer of gold supported by carbon support (Pt_1), respectively.

The TEM images were analyzed according to the method described in Section 3.1.5. Histograms of the size distributions for the four samples are shown in Figure 6.5.
The average diameter obtained from the TEM images of the platinum and platinum gold particles are shown in Table 6.1.

Table 6.1: The average diameter for the four samples

Sample	TEM diameter
Pt	2.9 ± 0.6 nm
Pt_1/3	2.9 ± 0.4 nm
Pt_2/3	3.1 ± 0.7 nm
Pt_1	3.2 ± 0.5 nm

The catalysts were subject to the accelerated corrosion experiment as described in Section 6.1.3. At this point it should be noted that only 1.9 mg Pt catalyst was available, and this amount was used for the

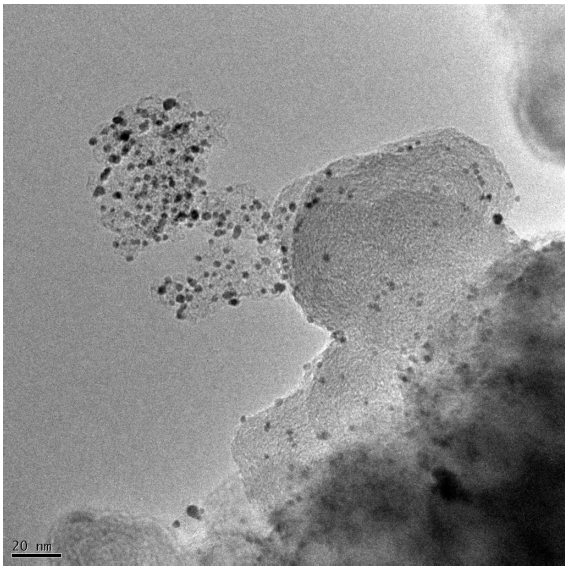

(a) TEM image of Pt catalyst. Image size: 227.15 nm × 227.15 nm

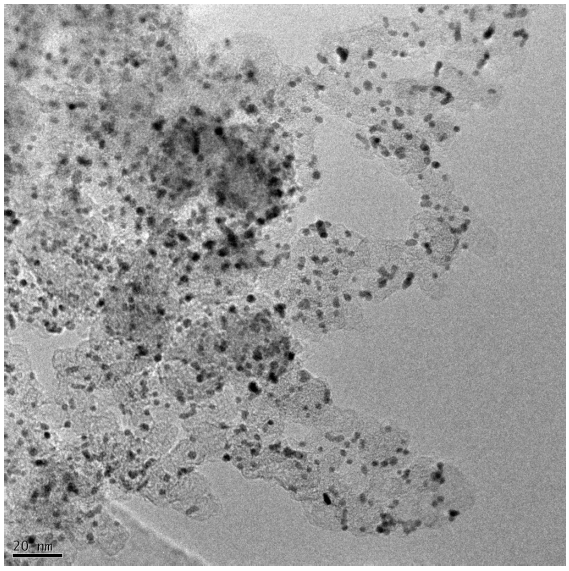

(b) TEM image of Pt catalyst. Image size: 227.15 nm × 227.15 nm

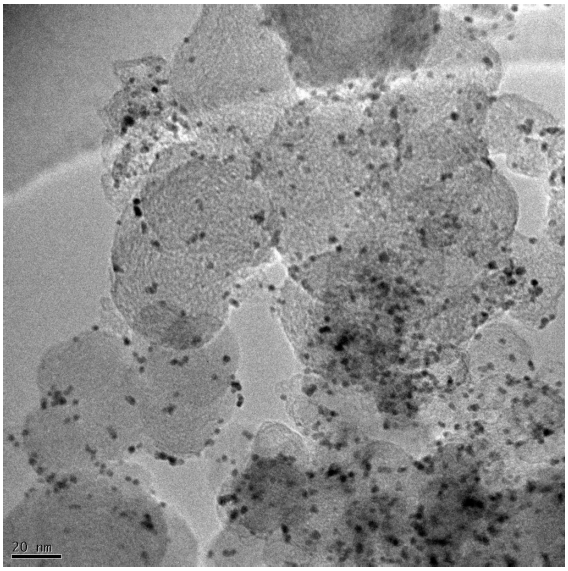

(c) TEM image of Pt catalyst. Image size: 227.15 nm × 227.15 nm

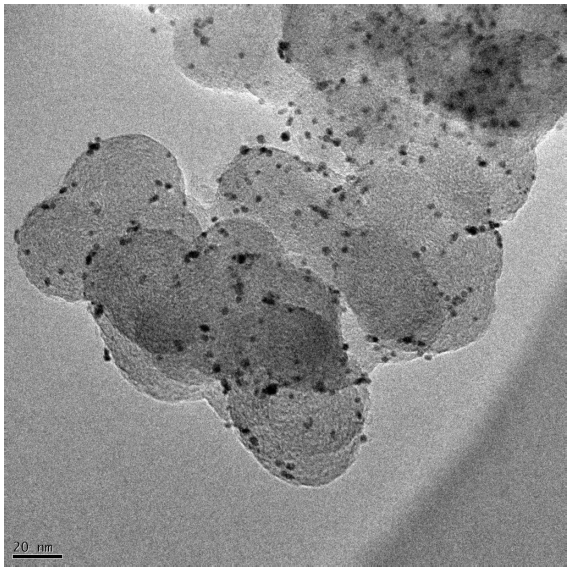

(d) TEM image of Pt catalyst. Image size: 227.15 nm × 227.15 nm

Figure 6.1: TEM images of Pt before corrosion stability experiment. The platinum particles have an average diameter of 2.9 ± 0.6 nm. The platinum particles, the dark spots, are uniformly distributed on the carbon support.

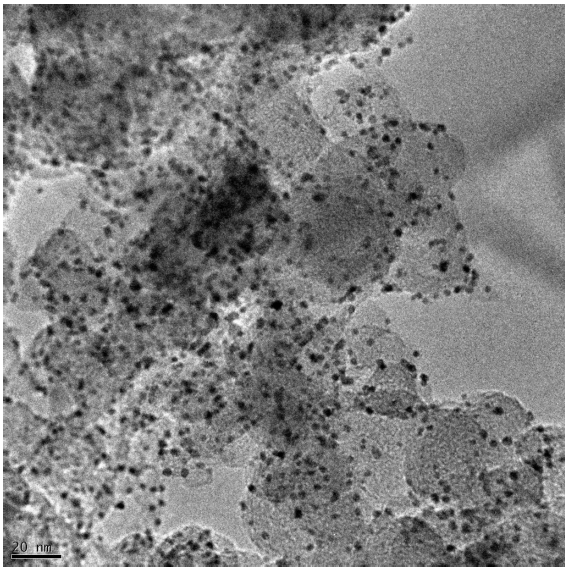

(a) TEM image of Pt_1/3 catalyst. Image size: 227.15 nm × 227.15 nm

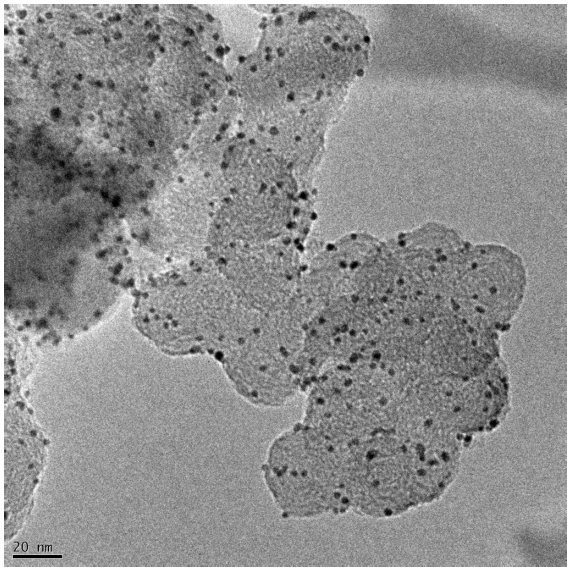

(b) TEM image of Pt_1/3 catalyst. Image size: 227.15 nm × 227.15 nm

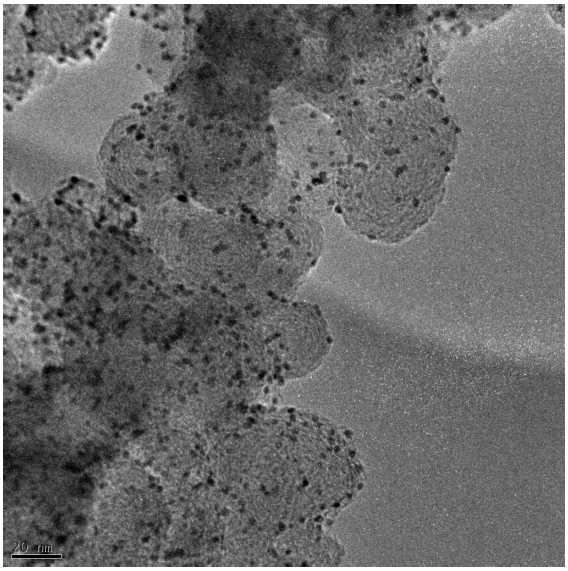

(c) TEM image of Pt_1/3 catalyst. Image size: 227.15 nm × 227.15 nm

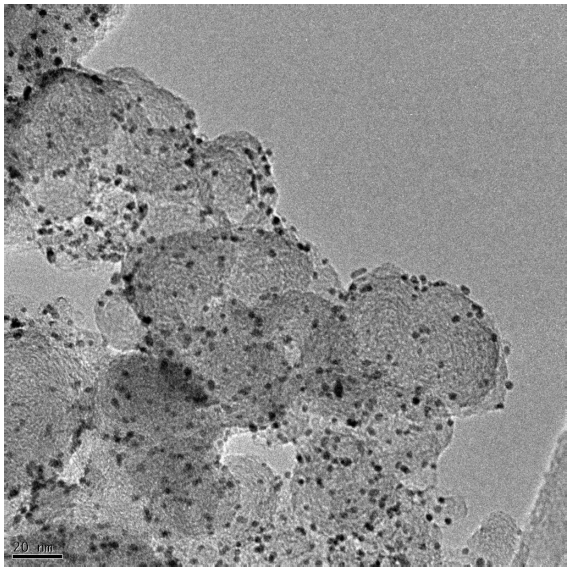

(d) TEM image of Pt_1/3 catalyst. Image size: 227.15 nm × 227.15 nm

Figure 6.2: TEM images of Pt_1/3 catalyst. The average diameter of the platinum particles are 2.9 ± 0.4 nm. The platinum particles, the dark sports, are uniformly distributed on the carbon support.

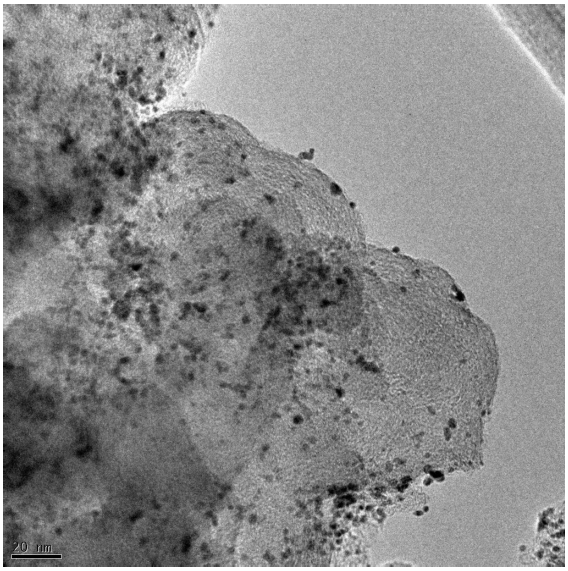

(a) TEM image of Pt_2/3 catalyst. Image size: 227.15 nm × 227.15 nm

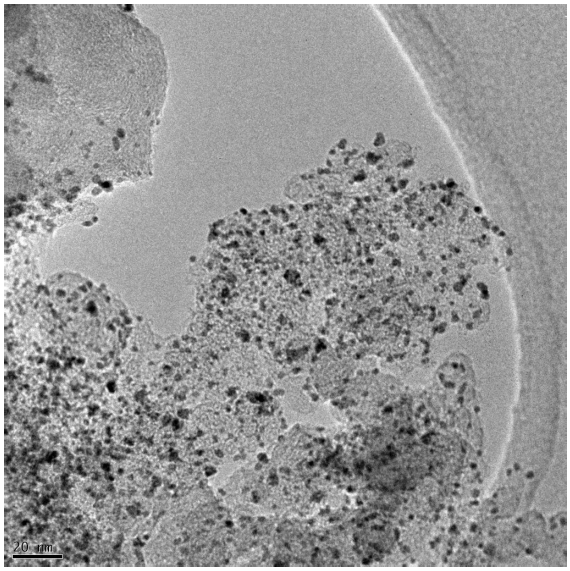

(b) TEM image of Pt_2/3 catalyst. Image size: 227.15 nm × 227.15 nm

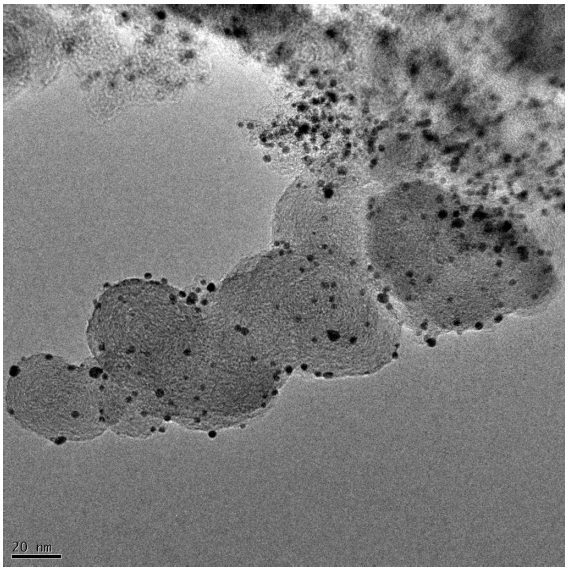

(c) TEM image of Pt_2/3 catalyst. Image size: 227.15 nm × 227.15 nm

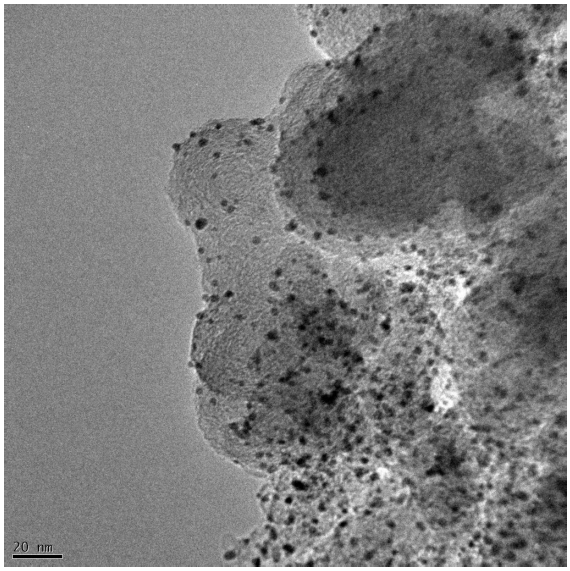

(d) TEM image of Pt_2/3 catalyst. Image size: 227.15 nm × 227.15 nm

Figure 6.3: TEM images of Pt_2/3 catalyst. The average diameter of the particles are 3.1 ± 0.7 nm. The platinum particles are uniformly distributed on the carbon support.

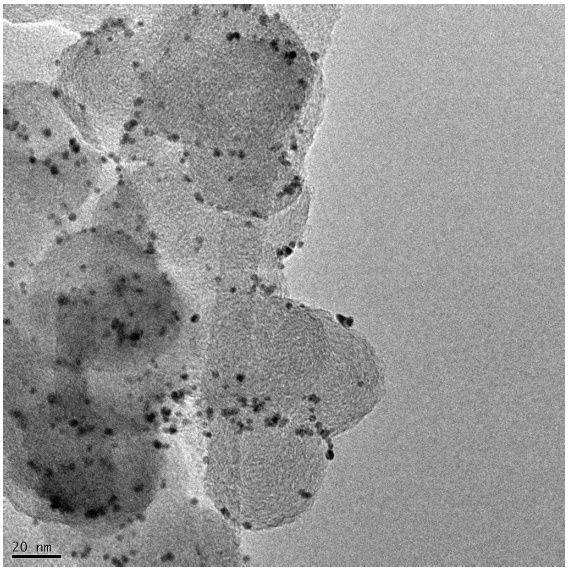

(a) TEM image of Pt_1 catalyst. Image size: 227.15 nm × 227.15 nm

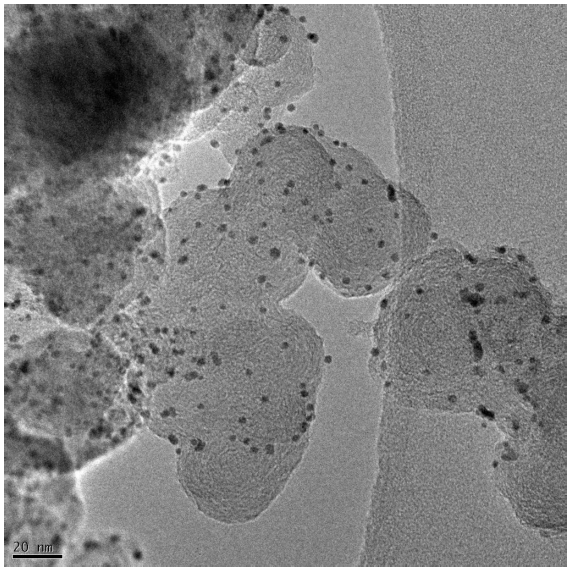

(b) TEM image of Pt_1 catalyst. Image size: 227.15 nm × 227.15 nm

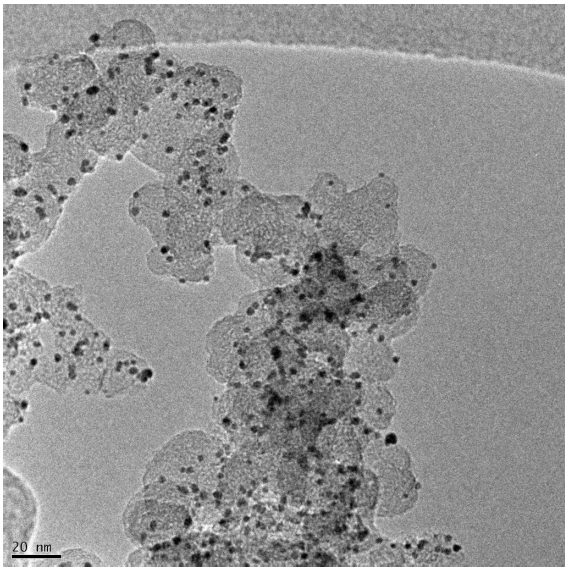

(c) TEM image of Pt_1 catalyst. Image size: 227.15 nm × 227.15 nm

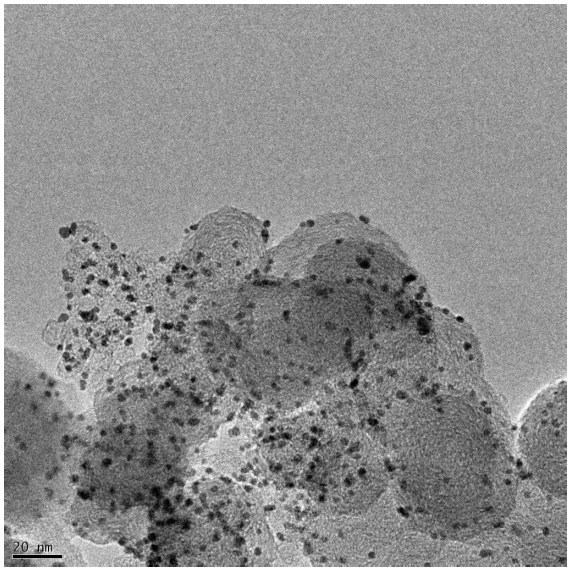

(d) TEM image of Pt_1 catalyst. Image size: 227.15 nm × 227.15 nm

Figure 6.4: TEM images of Pt_1 catalyst. the average diameter of the particles are 3.2 ± 0.5 nm. The platinum particles are uniformly distributed on the carbon support.

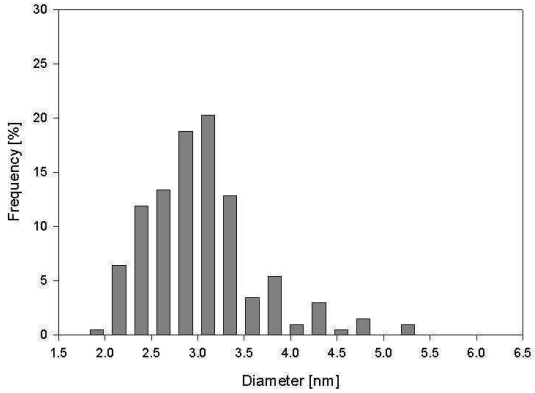

(a) The particle size distribution of Pt catalyst. Particle count is 202.

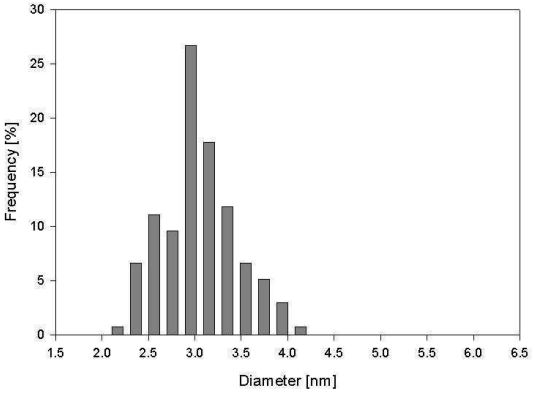

(b) The particle size distribution of Pt_1/3 catalyst. Particle count is 135.

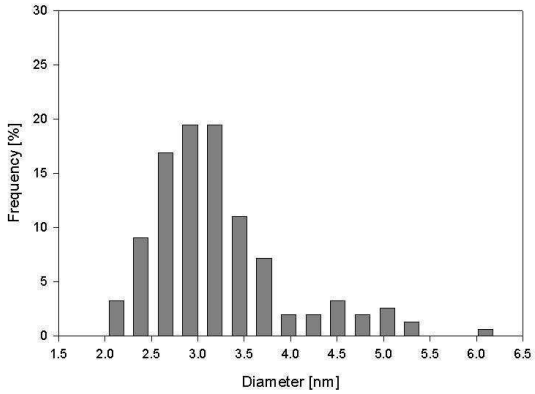

(c) The particle size distribution of Pt_2/3 catalyst. Particle count is 154.

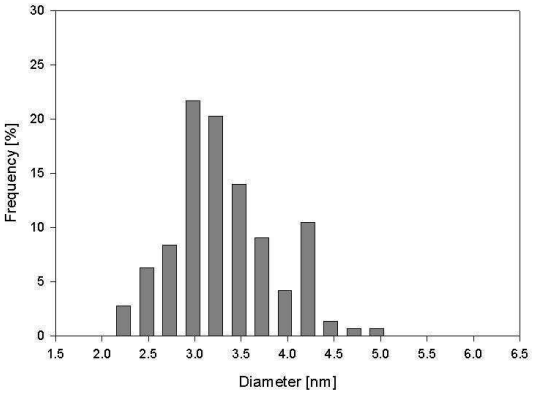

(d) The particle size distribution of Pt_1 catalyst. Particle count is 143.

Figure 6.5: The particle size distributions for the four samples. The bin size have been optimized according to the method described in Section 3.1.5.

ink preparation. For all the other samples 2.5 mg catalyst were used to produce the ink. The theoretical surface area of the platinum particles on the carbon support was derived as described in Appendix A. The electrochemical cyclic voltagrams were recorded before and after the corrosion experiment between 0.09 V vs RHE and 1.1 V vs RHE. The resulting voltagrams for all samples are shown in Figure 6.6.

The electrochemical active surface area before and after the corrosion test can be calculated using the Hupd area and the equivalent $210\frac{\mu C}{cm^2}$. This is described in details in Section 3.3. The electrochemical active surface areas are listed in Table 6.2.

Table 6.2: The electrochemical active surface area of the catalysts before and after accelerated corrosion experiments and compared to the theoretical surface area calculated from TEM characterizations.

Sample	TEM diameter	Theoretical surface area	Electrochemical active surface area before corrosion test	Electrochemical active surface area after corrosion test	Remaining activity
Pt	2.9 ± 0.6 nm	3.6 cm^2 $^{+0.9cm^2}_{-0.6cm^2}$	0.8 cm^2	0.2 cm^2	25%
Pt_1/3	2.9 ± 0.4 nm	4.7 cm^2 $^{+0.8cm^2}_{-0.6cm^2}$	1.2 cm^2	0.9 cm^2	75%
Pt_2/3	3.1 ± 0.7 nm	4.4 cm^2 $^{+1.3cm^2}_{-0.8cm^2}$	0.9 cm^2	0.5 cm^2	56%
Pt_1	3.2 ± 0.5 nm	4.3 cm^2 $^{+0.8cm^2}_{-0.6cm^2}$	0.9 cm^2	0.6 cm^2	67%
Pt/C from [31]					55%
AuPt/C from [31]					96%

6.3 Discussion

The results of the four corrosion experiments are shown in Table 6.2. This table shows that adding gold to the platinum nanoparticles have increased the stability of the electrocatalyst toward corrosion substantially. The present work presents a new synthesis based on the micro emulsion technique to prepare the electrocatalysts. However, the small electrochemical surface areas of the platinum particles observed in all the experiments could indicate that part of the surface areas are blocked by surfactants.
The corrosion stability of the platinum/gold catalyst obtained in this experiment can be compared to the corrosion stability study reported by Zhang *et al.* [31] taking in to account the same cations as in the experiments considering the commercial catalysts. The remaining activity for the four catalysts tested in the present work and the data obtained by Zhang *et al.* are summarized in Table 6.2.
As noted from Table 6.2 the platinum and platinum/gold particles supported by carbon synthesized in the present experiments have lower corrosion stabilities then the platinum and the platinum/gold particles tested by Zhang *et al.* This could be due to the differen testing methods used. However, the same trend is observed in the two experiments, i.e. gold enhances the corrosion stability of platinum particles.

The increased stability of the platinum gold catalysts relative to the platinum catalyst toward corrosion could be due to gold blocking the steps. This theory is supported by recent DFT calculations by Greeley [72]. He showed correlation between coordination number and dissolution potential of the platinum particles. Hence, the edge and corner atoms are expected to dissolve at low potentials and facilitate the corrosion of the entire particles.
Recent results by Fang *et al.* [73] have shown that PEM fuel cells with nano engineered platinum gold catalysts have excellent stability.
In the literature there are substantial body of theoretical and experiment evidence that connect the stability of platinum particles to their sizes [20, 34, 74]. Thus, as the size of the platinum and platinum gold particles are enlarged their stability should be further enhanced.

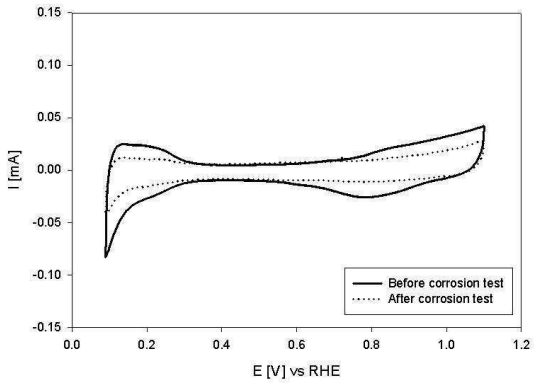

(a) Voltagrams of Pt catalyst before (solid line) and after (dotted line) accelerated corrosion experiment. The electrochemical surface area is reduced from 0.8 cm^2 to 0.2 cm^2 during the corrosion test.

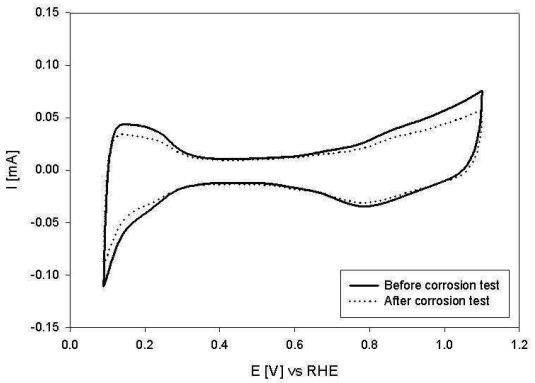

(b) Voltagrams of Pt_1/3 catalyst before (solid line) and after (dotted line) accelerated corrosion experiment. The electrochemical active surface area is reduced from 1.2 cm^2 to 0.9 cm^2 during the corrosion test.

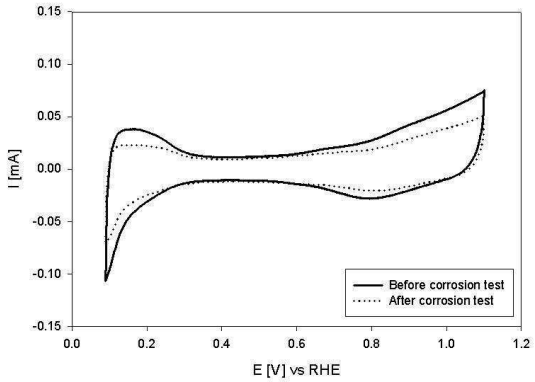

(c) Voltagrams of Pt_2/3 catalyst before (solid line) and after (dotted line) accelerated corrosion experiment. The electrochemical active surface area is reduced from 0.9 cm^2 to 0.5 cm^2 during the corrosion test.

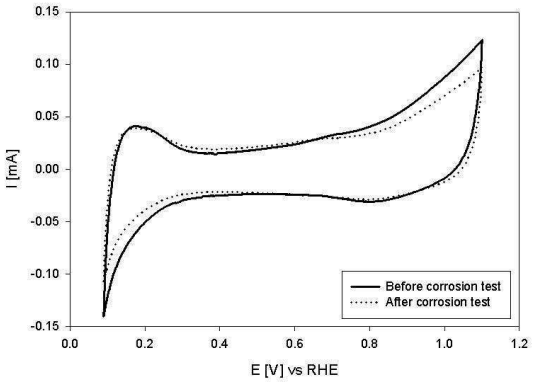

(d) Voltagrams of Pt_1 catalyst before (solid line) and after (dotted line) accelerated corrosion experiment. The electrochemical active surface area is reduced from 0.9 cm^2 to 0.6 cm^2 during the corrosion test.

Figure 6.6: Voltagrams of the four samples before and after the accelerated corrosion tests.

6.4 Conclusion

The experiments performed showed that platinum particles can be stabilized toward corrosion by adding gold to the platinum particles. The results obtained did not show any substantial difference between the 1/3, 2/3 and 1 monolayer of gold on platinum particles.
It has been shown that the electrochemical active surface areas of the platinum and platinum gold particles were low compared to the theoretical calculated surface areas. It is suggested that the surfactant used in the synthesis of the platinum particles are blocking part of the surface.

The experiments have not been repeated because the results were in agrement with results reported in the literature. Furthermore, the electrochemical active surface areas were very small possibly resulting from surfactant blocking the surface. Thus, a new synthesis method should be considered.

Chapter 7

Synthesis of 5 nm platinum particles

In the previous experiment it was shown that the 3 nm platinum gold particles are more stable than 3 nm platinum particles. It was proposed that the stabilizing effect could be further enhanced if the platinum particles were larger. To show if this is indeed the case larger platinum and platinum gold particles should be synthesized and electrochemically tested.
The aim of the experiments was to synthesize platinum nano particles with an average diameter of 5 nm. In total three different synthetic approaches were employed. These will be described in the following sections.

The inverse micelle method described in Section 6.1.1 resulted in particles of an average diameter around 3 nm. It is relatively difficult to alter the inverse micelle method to obtain larger platinum particles. Furthermore, the electrochemical active surface area of the platinum and platinum gold particles were very small compared to the theoretical values. This could be caused by the surfactant used in the inverse micelle method. Therefore, a new method was considered for synthesizing the platinum and platinum gold nanoparticles.

Lim *et al.* [75], Li *et al.* [76], and Long *et al.* [77] have synthesized platinum particles using the polyol method. The produced particles were shown to be electrochemically active. Li *et al.* [76] synthesized nano particles with a core shell structure. Therefore, it is anticipated that the polyol method can be used to synthesize platinum gold particles. Based on the work reported in Refs. [75–77] it was decided to use the polyol method in attempts to synthesize 5 nm platinum particles. Furthermore, the polyol method has the potential to be used to add gold or tantalum to the platinum particles.
In the polyol method a Pt-salt is reduced by acetaldehyde produced by oxidizing ethylene glycol (EG). The reaction scheme for the polyol method is described by Larcher *et al.* [78]. The first step is dehydration of ethylene glycol leading to acetaldehyde. In the next step acetaldehyde is oxidized and diacetyl is formed. As acetaldehyde is oxidized to diacetyl the platinum salt is reduced to platinum particles. The process is schematically illustrated in Figure 7.1.

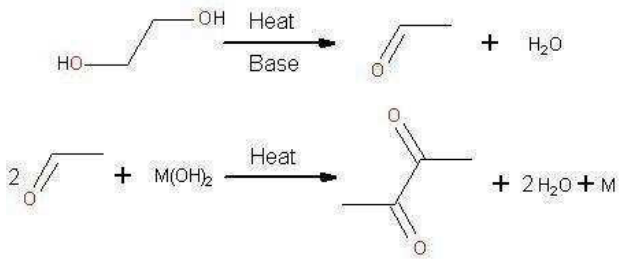

Figure 7.1: The reaction path for the polyol synthesis

The polyol method is very simple and does not require a stabilizing agent. However, the different parameters i the synthesis, such as pH, water to ethylene glycol ratio, time and temperature, could have great influence on the resulting nano particles.

7.1 Polyol experiment 1

The first procedure was inspired by the work of Lim *et al.* [75] who had obtained particles with an average size of 4.9 nm.
A mixture of 45 mL ethylene glycol (>99%, Sigma-Aldrich) and 5 mL of demineralized water (<33 Mωcm) was used to dissolve 20 mg H_2PtCl_6. A solution of carbon black XC72 and ethylene glycol was prepared by ultrasonic treatment. The average particle diameter of the carbon support was measured using Malvern Mastersizer E measuring the particle size distribution by laser diffraction to have a bi-normal distribution with peaks at $\sim$1 μm and $\sim$3.5 μm.
The Pt-precursor was added to the ethylene glycol water solution and stirred for one hour under N_2 flow. The solution was adjusted to above pH 10 with 15 mL 0.1 M NaOH (>97%) in demineralized water (<33 Mωcm). The mixture was heated according to the parameters presented in Table 7.1. The process was carried out under a flow of N_2. In the samples denoted distilled in Table 7.1 the water phase was removed by continues distillation through the entire synthesis.

Table 7.1: The parameters used in polyol experiment 1, part one

Sample	Pt	Temperature	Time [Hour]	Distilled/ Reflux	TEM-image
Pt_130_1	5 w%	130°C	1	Reflux	Recorded
Pt_130_2	5 w%	130°C	2	Reflux	
Pt_130_3	5 w%	130°C	3	Reflux	
Pt_130_4	5 w%	130°C	4	Reflux	Recorded
Pt_130_1_D	20 w%	130°C	1	Distilled	
Pt_130_2_D	20 w%	130°C	2	Distilled	
Pt_130_3_D	20 w%	130°C	3	Distilled	Recorded
Pt_130_4_D	20 w%	130°C	4	Distilled	

After heating the platinum samples the carbon solution was added to the mixture and stirred over night. A flow diagram of the process is presented in Figure 7.2.
The mixture was centrifuged until the carbon precipitated and thereafter the ethylene glycol solution was removed. The product was washed twice with ethanol and dried at 60°C. A flow diagram of the cleaning process is shown in Figure 7.3.
The platinum samples that were distilled during the heating process were easier to separate in the cleaning process.
The TEM images were recorded as described in Section 3.1.5. The TEM images of samples Pt_130_1, Pt_130_4 and Pt_130_3_D are shown in Figure 7.4.
The images show that the particles have diameters of approximately 2 nm. There are not much size difference between the particles that have been heated for one hour and the particles that have been heated for four hours. Furthermore, the particles have approximately the same size in the distilled samples as in the samples that were refluxed. Since the samples that were distilled were easier to clean, this method was used to investigate the effect of the temperature on the particle size.

The above described polyol procedure was used to investigate the temperature effect on the particle size. The temperature was raised to 145°C and 160°C and the nucleation time was varied between one and four hours. These temperatures were chosen since 160°C is the highest temperature used in the literature and 145°C is between 130°C and 160°C. An overview of the parameters used in the experiment is shown in Table

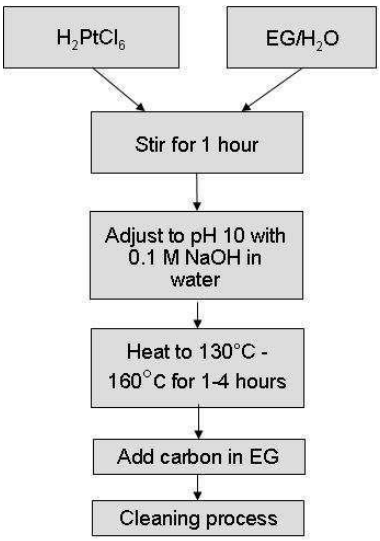

Figure 7.2: Flow diagram for polyol experiment one

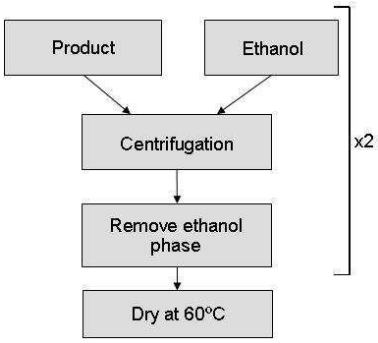

Figure 7.3: Flow diagram of the cleaning process

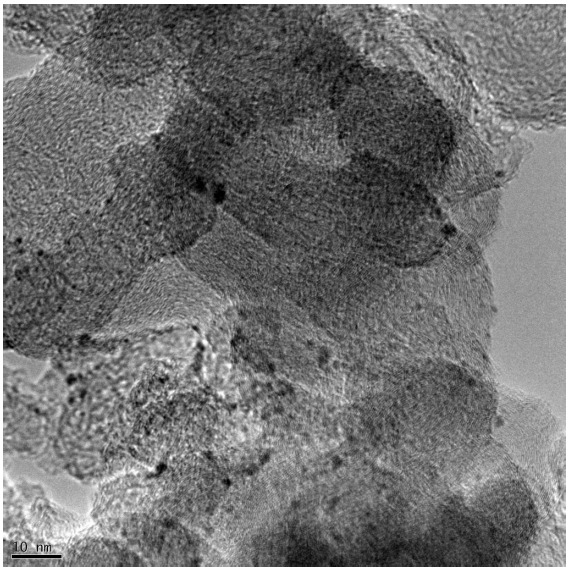

(a) TEM image of Pt_130_1. Image size: 113.023 nm × 113.023 nm. The images show that the platinum particles have diameters around 2 nm. The platinum loading is 5 w%. The platinum particles have been heated to 130°C for one hour.

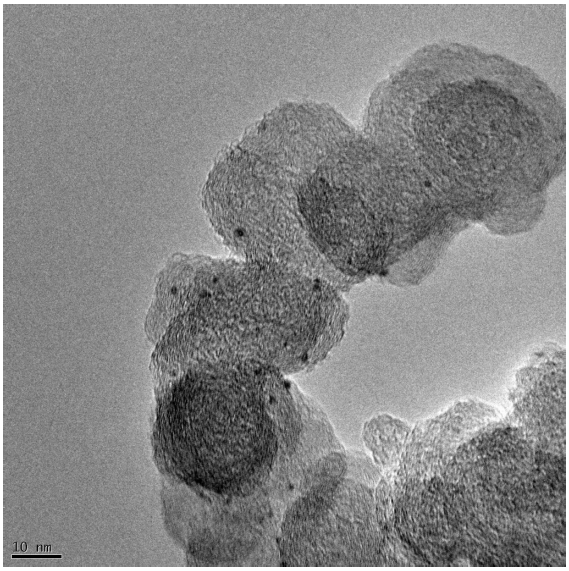

(b) TEM image of Pt_130_4. Image size: 113.023 nm × 113.023 nm. The images show that the platinum particles have diameters around 2 nm. The loading is 5 w%. The platinum particles have been heated to 130°C for 4 hours.

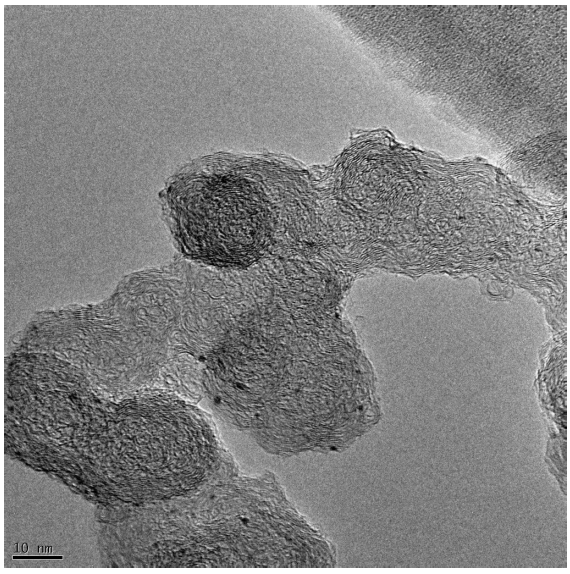

(c) TEM image of Pt_130_3_D. Image size: 113.023 nm × 113.023 nm. The images show that the platinum particles have diameters around 2 nm. The loading is 20 w%. The platinum particles have been heated to 130°C for 3 hours during which the water phase was removed by distillation.

Figure 7.4: TEM images of platinum particles synthesized with polyol method 1. The images show sample (a) Pt_130_1, (b) Pt_130_4 and (c) Pt_130_3_D. The images do not show appreciable size differences between the samples that are heated to 130°C for either one or four hours. Thus, the time does not have the anticipated effect on the sizes of the platinum particles. Furthermore, the particles where the water phase have been removed during the synthesis by distillation have the same sizes as the particles synthesized with reflux.

7.2.

Table 7.2: The parameters used in polyol experiment 1, part two

Sample	Pt w%	Temperature	Time [Hour]	Distilled/ Reflux	TEM-image
Pt_145_1_D	20 w%	145°C	1	Distilled	Recorded
Pt_145_1_D	20 w%	145°C	2	Distilled	Recorded
Pt_145_1_D	20 w%	145°C	3	Distilled	Recorded
Pt_145_1_D	20 w%	145°C	4	Distilled	Recorded
Pt_160_1_D	20 w%	160°C	1	Distilled	Recorded
Pt_160_2_D	20 w%	160°C	2	Distilled	
Pt_160_3_D	20 w%	160°C	3	Distilled	
Pt_160_4_D	20 w%	160°C	4	Distilled	Recorded

TEM images of samples Pt_145_1_D, Pt_145_4_D, Pt_160_1_D and Pt_160_4_D are shown in Figure 7.5.
The images show that the particle diameters are approximately 2 nm. There are not much difference in the sizes of the particles heated to 160°C and to 140°C. Furthermore, the TEM images shows that there are not much difference in the sizes of the particles heated for one and four hours.

7.1.1 Conclusion of polyol experiment 1

In the above described experiment particles with diameters of approximately 2 nm were obtained. It is noted that the different temperatures and times employed did not generate large variations in the particle sizes.
Long *et al.* [77] found that the total amount of water content used in the synthesis influences the final particle sizes. According to Li *et al.* [76] the water content of the solution should be around 5 vol% in order to obtain particles with an average diameter of 5 nm. The final water content in the above described synthesis was 30.8 vol% due to the addition of 0.1 M NaOH used to raise the pH to 10. Furthermore, the water content was not constant throughout the synthesis because the water phase was removed by distillation. In the experiments described below the water content is kept constant by refluxing. The solid NaOH will be dissolved in ethylene glycol which allows for a much more controlled level of water during the synthesis.

7.2 Polyol experiment 2

In the present experiment 68.9 mg of H_2PtCl_6 was dissolved in 130 ml ethylene glycol and the mixture was stirred for one hour. The carbon ethylene glycol dispersion identical to the one used in polyol experiment 1 was added to the mixture to obtain a final coverage of 20 wt% platinum on XC72. The mixture was stirred over night with a continuous flow of nitrogen.
According to Li *et al.* [76] a pH above 13 is desired. pH is difficult to measure in the mixture since pH is only defined for a system containing water. The NaOH solution used to adjust the pH in the work by Li *et al.* [76] is 2.5 M NaOH in ethylene glycol. The pH can be calculated under the assumption that the strong base NaOH dissociates completely in ethylene glycol:

$$pH = 14 - \left(-log\left(\frac{V_1 C_1}{V_1 + EG}\right)\right) \tag{7.1}$$

V_1 is the unknown volume of the 2.5 M NaOH solution that should be added to the mixture to obtain the desired pH, C_1 is the concentration of the 2.5 M NaOH solution, EG is the total volume of the mixture. Figure 7.6 shows a plot of pH as a function of ml 2.5 M NaOH added to the mixture.
In order to obtain a pH of 13, 24 ml of 2.5 M NaOH was added to the mixture. At this point the mixture

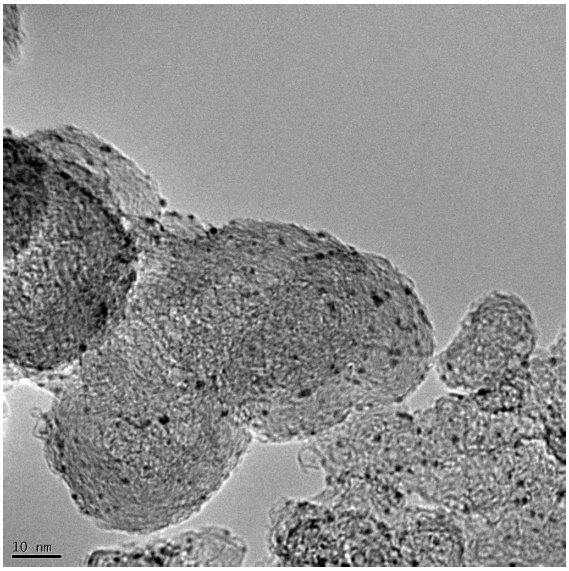

(a) TEM image of Pt_145_1_D. Image size: 113.023 nm × 113.023 nm. The platinum particles have been heated to 145°C for one hour during which the water phase was removed by distillation.

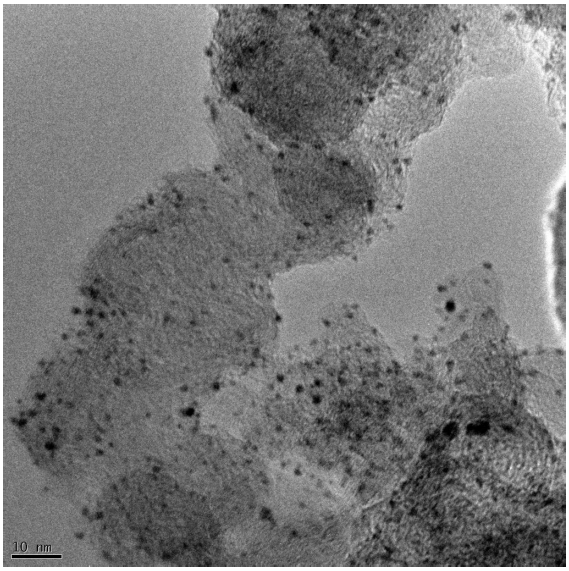

(b) TEM image of Pt_145_4_D. Image size: 113.023 nm × 113.023 nm. The platinum particles have been heated to 145°C for four hours during which the water phase was removed by distillation.

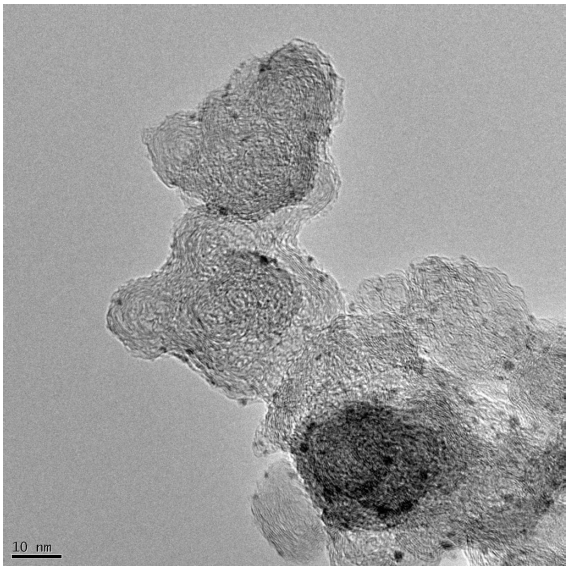

(c) TEM image of Pt_160_1_D. Image size: 113.023 nm × 113.023 nm. The platinum particles have been heated to 160°C for one hour during which the water phase was removed by distillation.

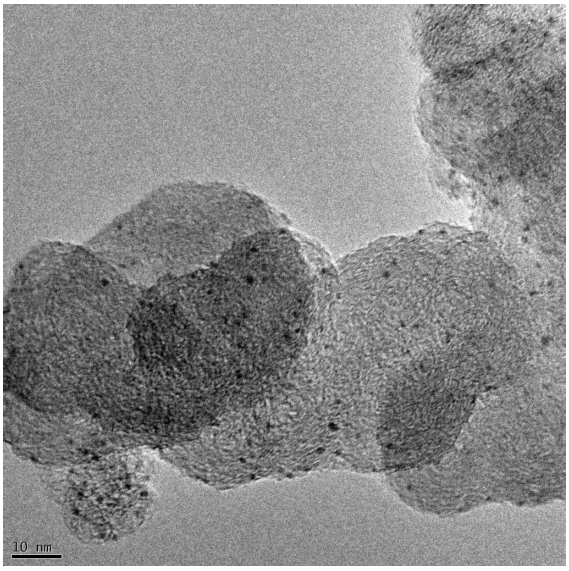

(d) TEM image of Pt_160_4_D. Image size: 113.023 nm × 113.023 nm. The platinum particles have been heated to 160°C for four hours during which the water phase was removed by distillation.

Figure 7.5: TEM images of Pt_145_1_D, Pt_145_4_D, Pt_160_1_D and Pt_160_4_D. Common for all the images is that the platinum particles all have a diameter around 2 nm. Hence, the synthesis temperature and the heating time does not have the anticipated effect on the sizes of the platinum particles.

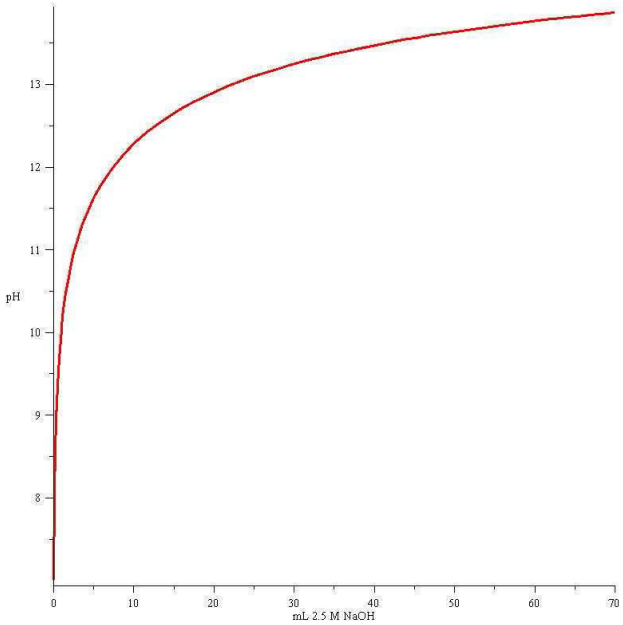

Figure 7.6: pH as function of added ml 2.5 M NaOH. The pH of the synthesis should be above 13 therefore 24 mL of 2.5 M NaOH is added.

was divided into three samples and water was added to each sample to obtain final water contents of 5 v/v%, 7.5 v/v% and 10 v/v%, respectively. The samples were heated for 3 hours at 140°C. A flow diagram of the synthesis is shown in Figure 7.7.
The cleaning procedure was identical to the one described in Section 7.1. An overview of the samples are shown in Table 7.3.

Table 7.3: The parameters used in polyol experiment 2

Sample	Pt	Temperature	Water	Distilled/ Reflux	TEM-image
Pt_5	20 w%	140°C	5 v/v %	Reflux	Recorded
Pt_7.5	20 w%	140°C	7.5 v/v %	Reflux	Recorded
Pt_10	20 w%	140°C	10 v/v %	Reflux	Recorded

The TEM images of Pt_5, Pt_7.5 and Pt_10 are shown in Figure 7.8.
The TEM images of the samples show small particles with diameters of approximately 4 nm and some very large particles with diameters of approximately 19 nm.

7.2.1 Conclusion of polyol experiment 2

The sizes of the platinum particles in the present experiments were not optimal. Some small particles were obtained but also some large particles. This bi-normal distribution could be due to the the addition of the carbon dispersion to the solution before the mixture is heated. Therefore, it is not advisable to add carbon at the beginning of the synthesis.

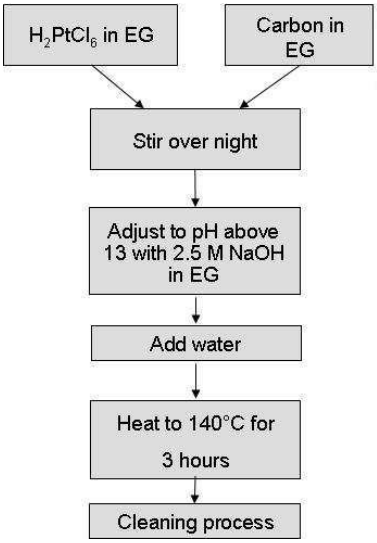

Figure 7.7: Flow diagram for polyol experiment 2. The differences form experiment 1 is that the carbon dispersion is added at the beginning of the synthesis and water is added just before the heating step. Furthermore, the water content of the synthesis is controlled because the pH is adjusted with 2.5 M NaOH in ethylene glycol rather than 0.1 M NaOH in water.

7.3 Polyol experiment 3

Experiment 2 revealed that the carbon dispersion added before the heating step resulted in particles with a bi-normal distribution. Experiment 1 revealed that the carbon dispersion added after the heating step resulted in a normal distribution of platinum particles with an average diameter of approximately 2 nm. Therefore, experiment 3 was carried out in an attempt to synthesize 5 nm platinum particles. In this experiment the carbon dispersion is added after the heating step and the water content is controlled during the process.
78 mg of H_2PtCl_6 was dissolved in 130 ml ethylene glycol and the mixture was stirred for one hour. As in experiment 2 the pH of 13 was obtained by adding 24 ml of 2.5 M NaOH to the mixture. The resulting mixture was divided into three samples containing 5 v/v% water, 7.5 v/v% water and 10 v/v% water, respectively. The samples were heated for 3 hours at 140°C. At the end of the heating step a precipitate was observed in each of the mixtures.
The carbon ethylene glycol dispersion as used in experiment 1 was added to the mixtures to obtain a final coverage of 20 wt% platinum on XC72. A flow diagram of the process is reported in Figure 7.9.
The cleaning procedure was identical to the one described in Section 7.1. An overview of the samples are shown in Table 7.4.

Table 7.4: The parameters used in polyol experiment 3

Sample	Pt	Temperature	Water	Distilled/ Reflux	TEM-image
Pt_5	20 w%	140°C	5 v/v %	Reflux	Recorded
Pt_7.5	20 w%	140°C	7.5 v/v %	Reflux	Recorded
Pt_10	20 w%	140°C	10 v/v %	Reflux	Recorded

The TEM images of Pt_5, Pt_7.5 and Pt_10 are shown in Figure 7.10.
The average diameters of the produced platinum particles are reported in Table 7.5 and the particle size distribution of the samples are shown in Figure 7.11.

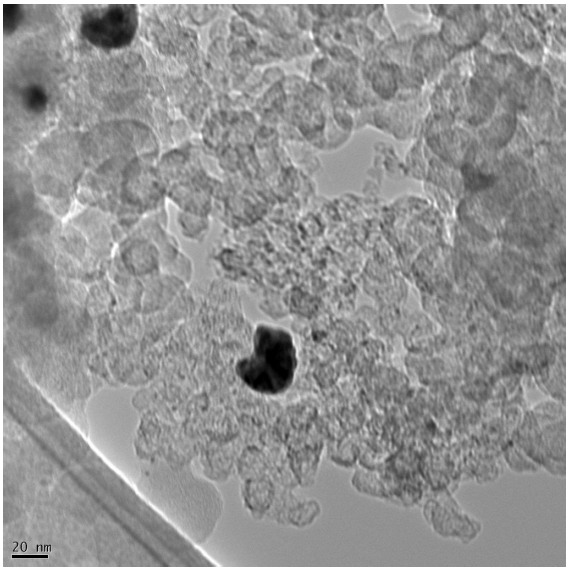

(a) TEM image of Pt_5. Image size: 113.023 nm × 113.023 nm. The water content of the synthesis is 5 v/v%.

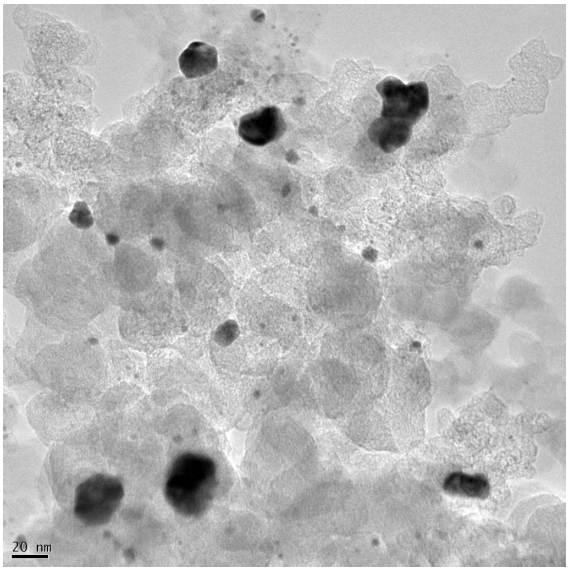

(b) TEM image of Pt_7.5. Image size: 113.023 nm × 113.023 nm. The water content of the synthesis is 7.5 v/v%

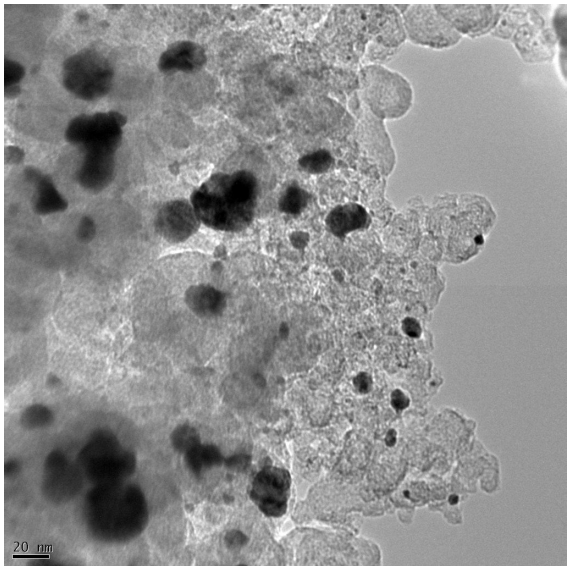

(c) TEM image of Pt_10. Image size: 113.023 nm × 113.023 nm. The water content of the synthesis is 10 v/v%

Figure 7.8: TEM images of (a) Pt_5, (b) Pt_7.5 and (c) Pt_10. For all water the different water contents bi-normal distributions of platinum particles on the carbon support are observed. This could be due to the addition of the carbon dispersion in the beginning of the synthesis.

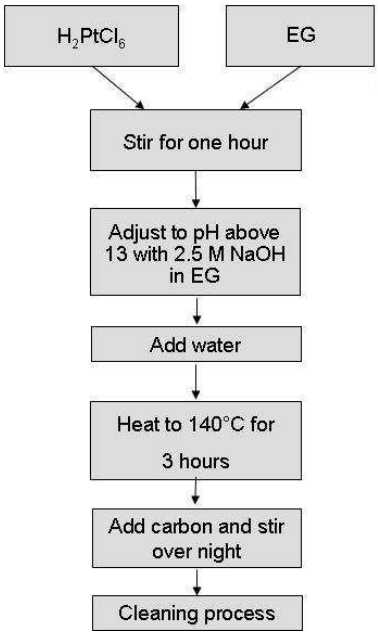

Figure 7.9: Flow diagram for polyol experiment 3. The synthesis differ form the method used in experiment 2 by the addition of the carbon dispersion after the heating step instead of in the beginning of the synthesis.

Table 7.5: The average TEM diameters of the platinum particles from experiment 3

Sample	Average diameter (TEM)
Pt_5	1.6±0.3 nm
Pt_7.5	1.8±0.4 nm
Pt_10	1.9±0.3 nm

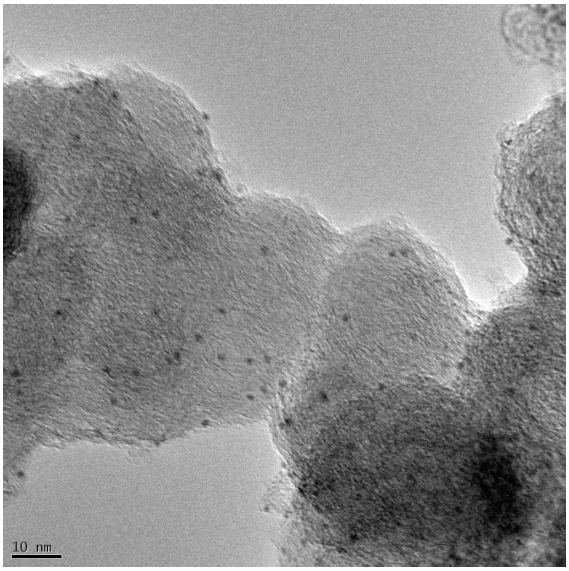

(a) TEM image of Pt_5. Image size: 113.023 nm × 113.023 nm. The water content of the synthesis is 5 v/v%. The average diameter of the platinum particles are 1.6 ±0.3 nm.

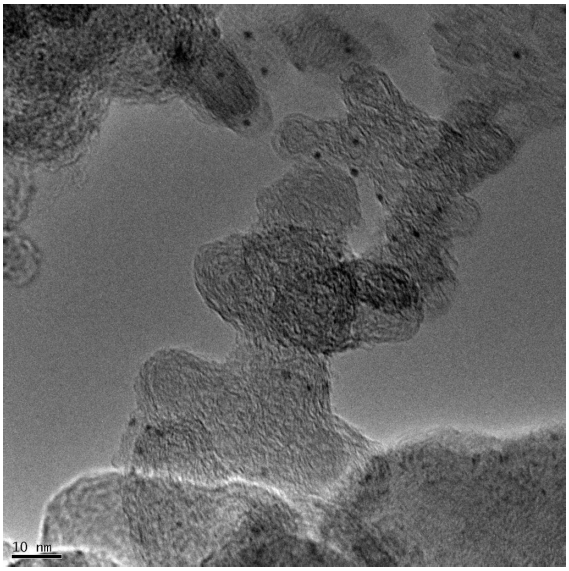

(b) TEM image of Pt_7.5. Image size: 113.023 nm × 113.023 nm. The water content of the synthesis is 7.5 v/v%. The average diameter of the platinum particles are 1.8±0.4 nm.

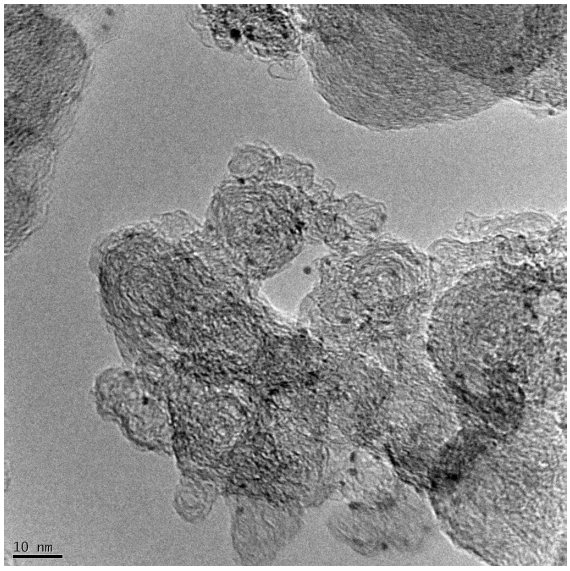

(c) TEM image of Pt_10. Image size: 113.023 nm × 113.023 nm. The water content of the synthesis is 10 v/v%. The average diameter of the platinum particles are 1.9±0.3 nm.

Figure 7.10: TEM images of (a) Pt_5, (b) Pt_7.5 and (c) Pt_10. For all three samples the platinum particles are uniformly distributed on the carbon support. The average diameters do not very much. Thus, the water content does not have the anticipated effect on the average diameter of the platinum particles.

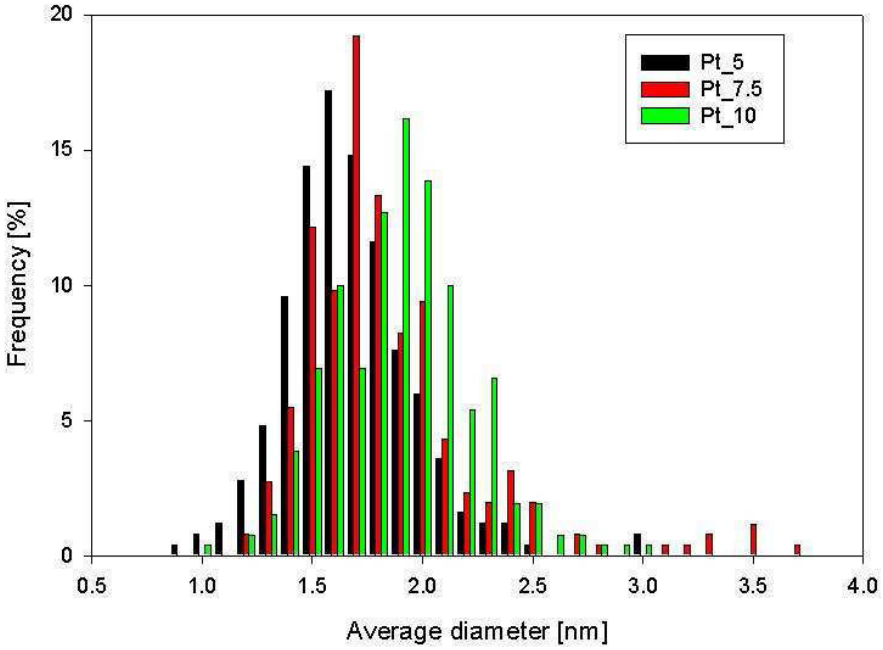

Figure 7.11: Particle size distributions for Pt_5 (black) counts 250, Pt_7 (red) counts 255 and Pt_10 (Green) counts 260. The particle size distributions for all samples is quit narrow the only difference between the three samples is that the top point shifts slightly to larger values when the water content is increased.

7.3.1 Conclusion of polyol experiment 3

The results of experiment 3 show that the platinum particles on the support are well dispersed, but the average size of the particles is smaller than required. Furthermore, during the synthesis of the particles sediment was observed. This sediment could be platinum particles that precipitate from the solution. The sedimentation could possibly be avoided by more vigorous stirring during the synthesis.
The amount of water does not appear to have the anticipated effect on the particle size distribution. From the particle size distribution it is noted that there are only minor variations around the center of the distribution. To further investigate the influence of the water on the platinum particle sizes distribution the amount of water was increased to 70%. The experimental method was identical to the one used in experiment 3. The particles obtained in this experiment was approximately 2 nm $\pm$ 0.4 nm. Thus, the water amount does not appear to influence the average size of the platinum particles significantly.

7.4 Conclusion of the polyol experiments

The goal of the polyol experiments, i.e. production of 5 nm platinum particles was not obtained during the experiments performed. When the carbon dispersion was added after the reduction to platinum the experiments revealed that a narrow particle size distribution of platinum particles was obtained. If the carbon dispersion was added before the reduction to platinum a bi normal distribution of platinum particles was obtained. The level of water does not appear to have the anticipated effect on the platinum particle size distribution.
From the TEM images of the platinum particles it is noted that the surface coverage of platinum on carbon is not very high. Therefore, it should be possible to increase the wt% of platinum as long as the dispersion of the particles on carbon is controlled.
As illustrated in Figure 7.1 one of the possible reaction paths for the polyol method is the oxidation of

ethylene glycol to acetaldehyde which reduces the platinum salt to platinum. In case the formation of the acetaldehyde is slow many platinum nucleation sites can be created leaving insufficient platinum for particle growth. Hence, the platinum particles formed are small. The platinum nucleation sites could possibly be created faster if the initial reduction was carried out by direct addition of acetaldehyde. The addition should take place under vigorous stirring. This suggestion might lead to creation of larger platinum particles.

The experiments have not been repeated since the desired 5 nm platinum particles were not obtained in any of the experiments performed.

Chapter 8

Summary and outlook

The start up and shut down of fuel cells have been simulated by potential cycling of platinum and platinum based catalyst.
The degradation mechanism of platinum particles on carbon support has been elucidated by TEM investigations of identical locations on a TEM grid before and after performing the corrosion experiment. The results obtained showed that electrochemical dissolution of platinum is one of the major factors limiting the durability of platinum nano particles towards potential cycling. The corrosion of the platinum particles was accelerated by increasing the upper voltage in the potential cycling experiment from 1.1 V to 1.2 V vs RHE. However, the same effect was observed when the upper limit was 1.1 V vs RHE and the sample was cycled for an extended period of time.

Three alternative commercial oxygen reduction reaction platinum catalysts have been characterized. The three commercial catalysts that were investigated have different corrosion stabilities even though they have similar data specs. From an industrial point of view it is interesting that one of the catalysts is more corrosion stable and has a higher utilization of the platinum surface area than the other ones.

Three different platinum/gold catalysts for the oxygen reduction reaction were synthesized and characterized. The platinum/gold systems were interesting since Zhang *et al.* [31] showed that gold could prevent platinum from corrosion in a fuel cells. The experiments performed showed that platinum particles can be stabilized toward corrosion by addition of gold to the platinum particles. In the present work the gold/platinum systems were synthesized using the inverse micelle method. However, the degree of gold coverage on the platinum particles revealed no substantial difference in the corrosion stability of the particles. It was shown that the electrochemically active surface areas of the platinum and platinum gold particles were very low compared to the theoretical values. This might be due to blockage of part of the surface area by the surfactant used in the synthesis of the particles.

In the literature there ia a substantial body of theoretical and experiment evidence that suggest that the stability of platinum particles is determined by there sizes [20, 34, 74]. Thus, if the sizes of the platinum and platinum gold particles are enlarged their stability could be enhanced.

In the final part of the project platinum particles were synthesized using the polyol method. This method was chosen because the particles synthesized using the inverse micelle method exhibited low accessible surface areas for the electrochemical reaction. However, the desired 5 nm platinum particles were not obtained during the synthesis performed. The point of addition of the carbon dispersion influences the platinum particle size distributions considerably. Thus when the carbon dispersion was added after the platinum salt was reduced to platinum particles a narrow particle size distribution was obtained. On the hand if the carbon dispersion was added before the reduction reaction bi-normal size distributions of the platinum particles were obtained. Reports in the literature claim the water content during the synthesis is important for the

size of the platinum particles produced. However, in the present work the amount of water did not have the anticipated effect on the particle sizes.
The TEM images of the platinum particles show that the surface coverage of platinum on carbon is not very high. Therefore, it should be possible to increase the wt% of platinum on the support as long as the dispersion of the particles on carbon is controlled.
According to Larcher *et al.* [78] the platinum particles are reduced by acetaldehyde. The acetaldehyde is formed by oxidation of ethylene glycol. Slow formation of acetaldehyde could resolve in numerous platinum nucleation sites and therefore insufficient platinum is left for the particle growth leading to formation of platinum particles with sizes less than the desired 5 nm. The platinum nucleation points could possibly be generated faster by direct addition of acetaldehyde during the reduction process. This might be a way to create larger particles.

Corrosion of platinum particles could be prevented by addition of gold to the steps and edges of the platinum particles. Another possibility is addition of tantalum to the platinum particles. According to the Pourbiax diagram for tantalum a stable surface layer of tantalum oxide is formed when tantalum is exposed to oxygen at low pH at potentials relevant to a fuel cell environment. Therefore, it could be interesting to synthesize platinum particles with a diameter above 5 nm and with tantalum decorating the steps and edges of the platinum particles.

References

[1] J. W. Niementsverdriet I. Chorkendoff. *Concept of modern Catalysis and Kinetics*. Wiley-VCH, 2003.

[2] A. Dicks J. Larminie. *Fuel Cell Systems Explained*. Wiley, 2003.

[3] B. Sompalli F. T. Wagner H. A. Gasteiger, S.S. Kocha. *Applied Catalyst B - Environmental*, 56:9, 2005.

[4] C. J. Yang. *Energy policy*, 37(5):1805, 2009.

[5] W. Grove. *London and Edinburgh Philosophical magazine and journal of science*, 14:127, 1839.

[6]

[7] http://www.optics.rochester.edu/workgroups/cml/opt307/spr05/eric/.

[8] S. J. Lee. Effects of nafion impregnaion on performance of pemfc electrodes. *Electrochemica Acta*, 43:3693, 1998.

[9] W. Vielstich C. H. Hanann, A. Hamnett. *Electrochemistry*. Wiley-VCH, 2004.

[10] Marcel Pourbaix. *Atlas of Electrochemical Equilbria*. Cebelcor, 1974.

[11] N. M. Rosengaard H. L. Skriver. *Physical Review B*, 46:7157, 1992.

[12] M. S. Daw S. M. Foiles, M. I. Baskes. *Physical Review B*, 33:7983, 1986.

[13] P. Stolze J. W. M. Frenken. *Physical Review Letter*, 82:3500, 1999.

[14] Y. Shao-Horn P. J. Ferreira. *Electrochemical Solid-State Letters*, 10:B60, 2007.

[15] E. Antolini. *Journal of Material Science*, 38:2995, 2003.

[16] K. L. More P. Atanassov R. L. Borup J. Xie, D. L. Wood. *Journal of the Electrochemical Society*, 152:A1011, 2005.

[17] C. Peng Z. W. Chen Y. Zhang Q. B. Fan X. Chang, L. Chen. *Journal of the Electrochemcal Society*, 151:A48, 2004.

[18] F. Charlot F. Maillard M. Chatenet E. Guilminot, A. Corcella. *Journal of the Electrochemical Society*, 154:B96, 2007.

[19] J. Z. Wang H. K. Liu S.X. Dou G. X. Wang, L. Yang. *Journal of Nanoscience and Nanoteknology*, 5:1135, 2005.

[20] S. Chen P. J. Ferreira E. F. Holby D. Morgan Y. Shao-Hrn, W. C. Sheng. *Topics in Catalysis*, 46:285, 2007.

[21] K. Tamura Y. Hishinuman A. Honji, T. Mori. *Journal of the Electrochemical Society*, 135:355, 1988.

[22] I. N. Remediakis H. Bengaard J. Nørskov J. Sehested, J. A. P. Gelten. *Journal of Catalysis*, 223:432, 2004.

[23] V. V. Slyozov I. M. Lifshitz. *Journal of Physics and Chemistry of Solids*, 19:35, 1961.

[24] B Pulvermacher E. Ruckenstein. *Journal of Catalysis*, 29:224, 1973.

[25] R. A. Buhrman C. C. Grandvist. *Journal of Catalysis*, 42:477, 1976.

[26] P. Stonehart J. A. Bett, K. Kinoshita. *Journal of Catalysis*, 35:307, 1974.

[27] K. E. Sickafus S. Gottesfeld M. S. Wilson, F. H. Garzon. *Journal of the Electrochemical Society*, 140:2872, 1993.

[28] A. Menzel N. M. Markovic H. You X. Wang D. Myers V.Komanicky, K. C. Chang. *Journal of the Electrochemical Society*, 153:B446, 2006.

[29] A. Hellman J. K. Nørskov J. Greeley, J. Rossmeisl. *Zeitschrift für Physikalishe Chemie*, 221:1209, 2007.

[30] J. Rossmeisl J. K. Nørskov G. A. Tritsaris, J. Greeley. *Catalysis Lettes*, 141:909, 2011.

[31] E. Sutter R. R. Adzic J. Zhang, K. Sasaki. *Science*, 315:220, 2007.

[32] T. Hatanaka Y. Morimoto R. Jinnouchi, E. Toyoda. *Journal of Physical Chemistry C*, 114:17557, 2010.

[33] D. Morgan E. F. Holby, W. Sheng. Y. Shao-Horn. *Energy & Environmental Science*, 2:865, 2009.

[34] R. C. Cammarata-C. Friesen K. Sieradzki L. Tang, X. Li. *Journal of the American Chemical Society*, 132:11722, 2010.

[35] N. A. Gjostein P. Wynblatt. *Acta Metallurqica*, 24:1165, 1976.

[36] J. P. Meyers R. M. Darling. *Journal of the Electrochemical Society*, 150:A1523, 2003.

[37] R. Makharia S. Kocha T. Fuller M. Matthias, H. Gasteiger. *Preprints of papers - American Chemical Society, Division of Fuel Chemistry*, 49:471, 2004.

[38] T. W. Patterson J. S. Yi J. D. Yang M. Perry T. D. Jarvi C. A. Reiser, L. Bregoli. *Electrochemical and Solid-State Letters*, 8:A273, 2005.

[39] M. Ramani J. F. Elter H. Tang, Z. Qi. *Journal of Power Sources*, 158:1306, 2006.

[40] B. Pivovar Y. S. Kim R. Mukundan N. Garland D. Myers M. Wilson F. Garzon D. Wood P Zelenay K. More K. Stroh T. Zawodzinski J. Boncella J. E. McGrath M. Inaba K. Miyatake M. Hori K. Ota Z. Ogumi S. Miyata A. Nishikata Z. Siroma Y. Uchimoto K. Yasuda K-I. Kimijima N. Iwashita R. Borup, J. Meyers. *Chemical Reviews*, 107:3904, 2007.

[41] R. M. Darling J. P. Meyers. *Journal of The Electrochemical Society*, 8:A1432, 2006.

[42] E. Schwan H. Rose B. Kabius K. Urban M. Haider, S. Uhlemann. *Nature*, 392:768, 1998.

[43] C. B. Carter D. B. Williams. *Transmission electron microscopy*. Plenum Press, 1996.

[44] J. Turkevich. *Journal of Chemical Physics*, 13:235, 1945.

[45] www.maxsidorov.com/cftexplorer.

[46] P Diaconis D Freedman. *Zeitschrift für Wahrscheinlichkeitstheorie und verwandte Gebiete*, 57:453, 1981.

[47] R. M. Curtis R. G. Meisenheimer C. R. Adams, H. A. Benesi. *Journal of Catalysis*, 1:336, 1962.

[48] E. Antolini. *Journal of Material Science*, 38:2995, 2003.

[49] K. M. Eriksen R. Fehrmann S. Koutsopoulos, T. Johannessen. *Journal of Catalysis*, 238:206, 2006.

[50] K. M. E. R. F. S. Koutsopoulos. *Journal*, 238:270, 2006.

[51] O. H. Han K. J. Hwang I. Kim H. Kim K. S. Han, Y. S. Moon. *Electrochemistry Communications*, 9:317, 2007.

[52] O. H. Han K. S. Han. *Bull. Korean Chem.*, 27:1121, 2006.

[53] P. K. Babu K. S. Han, O. H. Han. *Journal of the Electrochemical Society*, 152:J131, 2005.

[54] J. A. R. van Veen T. Frelink, W. Visscher. *Journal of Electroanalytical Chemistry*, 382:65, 1995.

[55] J. Panyam V. Labhasetwar S. Prabha, W-Z. Zhou. *International Journal of Pharmaceutics*, 244:105, 2002.

[56] C. L. Hui I-Ming Hsing J. Prabhuram, X. Wang. *Journal of Physical Chemistry B*, 107:11057, 2003.

[57] A. K. Datye M. P. Mokhonoana, N. J. Coville. *Catalysis Lettes*, 135:1, 2010.

[58] T. Tanaka M. Miyake T. Teranishi, M. Hosoe. *Journal of Physical Chemistry B*, 103:3818, 1999.

[59] E. F. Sitters G. J. M. Janssen. *Journal of Power Sources*, 171:8, 2007.

[60] A. Joly R. Goeke A. Datye P. Atanassov Y. Gu, J. St-Pierre. *Journal of the Electrochemical Society*, 154:B485, 2009.

[61] S. Swathirajan B. Merzougui. *Journal of the Electrochemical Society*, 153:A2220, 2006.

[62] K. Routsis P. Stonehart J. Bett, K. Kinoshita. *Journal of Catalysis*, 29:160, 1973.

[63] R. Woods T. Biegler, D. A. Rand. *Journal of the Electroanalytical Chemistry*, 29(2):269, 1971.

[64] P. N. Ross Jr. N. M. Markovic. *Surface Science Reports*, 45:117, 2002.

[65] K. Hayakawa T. Tada Y. Shao-Horn S. Chen, H. A. Gasteiger. *Journal of The Electrochemical Society*, 157:A82, 2010.

[66] J. C. Meier G. K. H. Wiberg M. Hanzlik M. Arenz K. J. J. Mayrhofer, S. J. Ashton. *Jounal of Power Sources*, 185:734, 2008.

[67] S. J. Ashton G. K. H. Wiberg F. Kraus M. Hanzlik M. Arenz K. J. J. Mayrhofer, J. C. Meier. *Electrochemistry Communications*, 10:1144, 2008.

[68] M. Arez K. J. J. Mayrhofer, M. Hanzlik. *Electrochimica Acta*, 54:5018, 2009.

[69] B. L. Abrams J. P. Wilcoxon. *Chemical Society Reviews*, 35:1162, 2006.

[70] P. Ocon J. L. G. de la Fuerte P. Terreros M. A. Pena J. L. Garcia-Fierro P. Hernandez-Fernandez, S. Rojas. *Applied Catalyst B - Environmental*, 77:19, 2007.

[71] W. Gu J. Jorne H. A. Gasteiger Y. Liu, C. Ji. *Journal of the Electrochemcal Society*, 158:B614, 2011.

[72] J. Greeley. *Electrochemica Acta*, 55:5545, 2010.

[73] X. Hu J. Last R. Loukrakpam J. Yin J. Lou C. Zhong B. Fang, B. N. Wanjala. *Journal of Power Sources*, 196:659, 2011.

[74] K. Persson C. Friesen T. He. K. Sieradzki G. Ceder L. Tang, B. Han. *Journal of the American Chemical Society*, 132:596, 2010.

[75] S. J. Hwang S. J. Yoo E. A. Cho T. H. Lim S. K. Kim B. Lim, J. W. Kim. *Bull. Korean Chem.*, 31:1577, 2010.

[76] W. Zhou J. Qiu Z. Zhou G. Sun Q. Xin W. Li, C. Liang. *Journal of Physical Chemistry B*, 107:6292, 2003.

[77] T. Matubara M. Nogami N. V. Long, T. Asaka. *Acta Materialia*, 59:2901, 2011.

[78] R. Patrice D. Larcher. *Journal of Solid State Chemistry*, 154:405, 2000.

Appendix A

Calculation of the theoretical active area

To calculate the total surface area on the glassy carbon a number of values have to be known. The average diameter of the particles have to be known. They can be measured either with TEM or XRD. The average diameter is denoted $d_{average}$, The catalyst loading in percent denoted L and the mg of catalyst dissolved in 1020μL solution denoted *Catalyst Mass*.From this the amount of Platinum on the glassy carbon can be calculated to be

$$\text{Amount of platinum} = \frac{\text{Catalyst Mass} \cdot L \cdot V}{1020 \cdot 100} \tag{A.1}$$

Where V in the numerator is the volume of the sample from the ink solution that is driped on to the glassy carbon, in this project it is either 10μL or 20μL. The 1020 in the denominator is because the total volume of the ink solution is 1020μL and the 100 in the denominator is because the loading of the catalyst is in percentage.
It is assumed that the Platinum particles on the surface of the carbon support are perfect spheres and there volume are given by

$$Volume = \frac{4}{3}\pi \left(\frac{d_{average}}{3}\right)^3 \tag{A.2}$$

The mass of one particle can be calculated from the density and the volume of the particles

$$\text{Mass} = \text{density} \cdot \text{Volume} \tag{A.3}$$

The density of platinum is 21.45 g/cm^3. The total number of platinum particles on the glassy carbon can be calculated to

$$\text{Number of particles} = \frac{\text{Amount of platinum}}{\text{Mass}} \tag{A.4}$$

The surface area of one particle is given by

$$\text{Surface} = 4\pi \left(\frac{d_{average}}{2}\right)^2 \tag{A.5}$$

The total platinum surface area on the glassy carbon can then be calculated from

$$\text{Total Surface} = \text{Surface} \cdot \text{Number of particles} \tag{A.6}$$

Appendix B

Included publication

Identical location transmission electron microscopy study of Pt/C electrocatalyst degradation during oxygen reduction reaction

F. J. Perez-Alonso, C. F. Elkjær, S. S. Shim, B. A. Abrams, I. E. L. Stephens, I. Chorkendoff

Journal of Power Sources, **196**, 6085, (2011)

Journal of Power Sources 196 (2011) 6085–6091

Contents lists available at ScienceDirect

Journal of Power Sources

journal homepage: www.elsevier.com/locate/jpowsour

Identical locations transmission electron microscopy study of Pt/C electrocatalyst degradation during oxygen reduction reaction

Francisco J. Perez-Alonso[a], Christian F. Elkjær[a], Signe S. Shim[a,b], Billie L. Abrams[a], Ifan E.L. Stephens[a], Ib Chorkendorff[a,*]

[a] Center for Individual Nanoparticle Functionality, Department of Physics, Building 312, Technical University of Denmark, DK-2800 Lyngby, Denmark
[b] IRD Fuel Cells A/S, Kullinggade 31, DK-5700 Svendborg, Denmark

ARTICLE INFO

Article history:
Received 14 December 2010
Received in revised form 22 January 2011
Accepted 27 March 2011
Available online 6 April 2011

Keywords:
Oxygen reduction
Identical locations transmission electron microscopy
Platinum
Corrosion
Fuel cell

ABSTRACT

The degradation mechanisms of Pt nanoparticles supported on Carbon have been characterized during oxygen reduction reaction (ORR) conditions using IL-TEM. A TEM grid is used as the sole working electrode allowing a direct correlation between the electrochemical response and the TEM analysis. We mainly observe a decrease in nanoparticle size with some particle disappearance and some particle sintering after potential cycling simulating the start-up and shut-down of a fuel cell. The observation of nanoparticles with reduced particle size provides evidence that dissolution phenomena are the main cause of degradation in Pt/C electrocatalysts, under ORR conditions.

1. Introduction

Proton exchange membrane fuel cells (PEMFC's) could play a major role in a future carbon-free society, with their ability to convert chemically stored energy into electricity. Arguably, the most significant obstacle preventing the widespread utilisation of PEMFC's is their prohibitively high cost. A significant portion of these costs can be traced to the poor activity and low stability of the Pt/C electrocatalysts at the cathode, which drives the oxygen reduction reaction (ORR) [1]. In recent years, significant improvements have been made to the activity of Pt by alloying it with other metals [2–5]. However, catalyst stability is also of critical importance for PEMFC applications [6–13].

This is an important issue for any new alloy catalyst. Even for the pure Pt there is a need to elucidate the mechanism for loosing activity during ORR. By understanding the fundamentals behind catalyst instability, we should ultimately be able to develop more fruitful strategies towards preventing Pt corrosion.

The instability of Pt is manifested as an effective loss of catalyst surface area. It is particularly pronounced when the cathode is exposed to high potentials, either during shut down/start up cycles or through inadvertent 'cell reversal'.

The loss of Pt surface area has been attributed to four different processes [7]:

(i) Ostwald ripening: the dissolution of metal ions from smaller particles, which diffuse and re-deposit onto larger particles.
(ii) Particle coalescence: the migration of Pt nanoparticles, leading to larger nanoparticles.
(iii) Dissolution of Pt nanoparticles and reprecipitation in the ionomer phase, forming new Pt nanoparticles which cannot contribute to the catalytic effect.
(iv) Detachment of nanoparticles from the carbon support.

Electrocatalyst degradation can be monitored, *in situ*, using electrochemical methods, albeit with little mechanistic insight. Transmission electron microscopy (TEM) is a powerful tool for examining the localised changes to catalyst structure during reaction conditions. However, most examples in the literature have relied on a *post-mortem* approach to TEM [14–17].

Recently, Mayrhofer et al. developed the identical location TEM (IL-TEM) technique [18–20]. Using this technique, they could observe *identical locations* of a sample examined *before* and *after* TEM analysis. In particular, their studies focussed on size distributions, the absolute number of nanoparticles and carbon support corrosion. Catalyst degradation was only observed when the sample was cycled to high potentials of 1.4 V, apparently caused by nanoparticle detachment [19,20]. On the contrary, electrocatalyst

* Corresponding author. Tel.: +45 4525 3170; fax: +45 4593 2399.
E-mail address: ibchork@fysik.dtu.dk (Ib Chorkendorff).

0378-7753/$ – see front matter © 2011 Elsevier B.V. All rights reserved.
doi:10.1016/j.jpowsour.2011.03.064

corrosion was not observed when the upper potential limit was confined to 1.05 V or 1.2 V.

In the current investigation, we use the IL-TEM technique to monitor Pt/C degradation under ORR conditions. We investigate Pt/C catalyst with a size of $\sim 2.3 \pm 0.4$ nm. In particular, we choose to investigate smaller nanoparticles as they are inherently less stable, meaning that their corrosion should be more easily observable than larger nanoparticles. This smaller size is also closer to the size given as the optimal size ($\sim$3 nm) for a maximum ORR mass activity [1].

We have modified Mayrhofer et al.'s original experiments [18–20], by using only a single working electrode, in the form of the TEM grid. In their experiments, the TEM grid was connected in parallel to another working electrode. Although Mayrhofer et al.'s configuration resulted in a more quantitative electrochemical response; our configuration allows a more direct comparison to be made between the electrochemical measurements and the TEM analysis.

Our experiments aim to simulate the effect of fuel cell load cycling (start up and shut down). This was achieved by cycling the TEM grid in O_2 saturated 0.1 M $HClO_4$, between 0.6 and 1.1 or 1.2 V at different scan rates.

2. Materials and methods

The Pt/C electrocatalyst was prepared using the inverse micelle method, with the aim of obtaining a narrow nanoparticle size distribution [21,22].

The H_2PtCl_6 precursor (0.005 M Pt concentration) was introduced into a solution containing a micro-heterogeneous environment of droplet-like inverse micelles formed by the surfactant didodecyldimethyl ammonium bromide (DDAB) (5 wt% DDAB content) in toluene. Then, an excess of $LiBH_4$ in tetrahydrofuran solution (final concentration of 0.08 M) is added to the micelle solution, whilst stirring, to achieve complete reduction of the metal particles.

Following this, a carbon black (Vulcan XC72R, CABOT)-DDAB-toluene suspension was prepared, with the appropriate weight of C to obtain a final metal content of 10 wt%. The mixture was sonicated for 30 min, resulting in a homogenous suspension. Then the nanoparticle solution was slowly added to the carbon black suspension. After 4 h of stirring, a destabilizing agent (ethanol 99.9%) was added dropwise to break the droplet-like inverse micelle equilibrium and precipitate the metal nanoparticles. This solution was continuously stirred to avoid particle agglomeration. The mixture was allowed to settle and decant overnight. The solid sample was recovered, further separated and washed with ethanol by centrifugation several times and dried at 60 °C overnight.

The electrochemical experiments were performed with Bio-Logic Instruments' VMP2 potentiostat, controlled by a computer. The rotating disc electrode (RDE) assemblies were provided by Pine Instruments Corporation. All glassware was cleaned in a 3:1 mixture of concentrated H_2SO_4:concentrated H_2O_2. This was subsequently sonicated and rinsed several times in Millipore water (>18.2 MΩ cm^{-1}, TOC < 5 ppb). A standard three-compartment glass cell was used for all electrocatalysis experiments. The electrolyte, 0.1 M $HClO_4$ (Aldrich, TraceSELECT® Ultra) was prepared using Millipore water (>18.2 MΩ cm^{-1}, TOC < 5 ppb). The counter electrode was a carbon cloth and the reference was Hg/Hg_2SO_4 electrode. However, all potentials were calibrated with respect to a reversible hydrogen electrode (RHE); the reference electrode was separated from the working electrode compartment using a ceramic frit. A TEM grid containing the Pt/C sample in contact with a glassy carbon electrode was used as the working electrode. All measurements were conducted at room temperature. Fig. 1 shows the configuration we have used whereby the TEM grid is placed inside a holder adapted for the rotating disk electrode measurements.

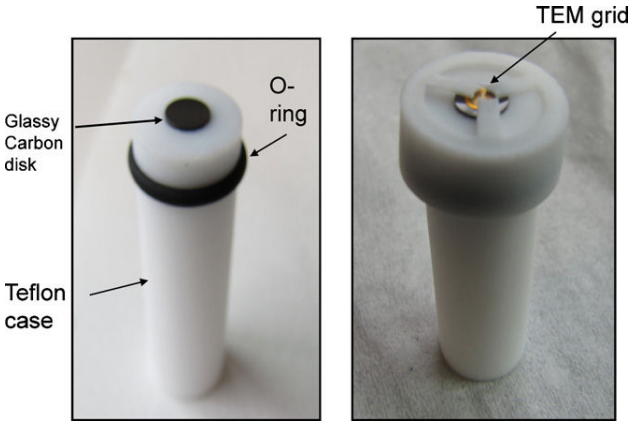

Fig. 1. Teflon holder adapted for the rotating disk electrode measurements using the Au TEM grid as working electrode.

For the corrosion tests, the working electrode was cycled between 0.6 and 1.1 V and between 0.6 and 1.2 V, without rotation, in O_2-saturated electrolyte. Two different scan rates were used, 50 and 200 mV s^{-1}. The effect of the total number of cycles was also studied by scanning the electrode between 0.6 and 1.1 V for 3000 or 30,000 cycles.

The ORR activity was carried out before and after the corrosion measurement, between 0 V and 1 V, at 20 mV s^{-1}, at 1600 RPM.

The TEM experiments were performed, using a TECNAI T20 electron microscope with a primary electron energy of 200 keV. For the TEM and electrochemical experiments, the Pt carbon supported catalyst was dispersed ultrasonically in isopropyl alcohol (Aldrich, 99.8%) to a concentration of 1.5 $mg_{catalyst}$ mL^{-1} for 30 min. A volume of 5 μL of the suspension was pippetted onto a gold-coated TEM grid with Lacey Carbon (300 mesh; Agar Scientific). We note that the catalyst loading on the grid was high in comparison to a conventional TEM experiment; this was in order to obtain a sufficiently high electrochemical response from the Pt/C on the TEM grid, when it was used as a working electrode. Despite the high catalyst loading, locations without overlapping catalyst particles were found on all the samples tested.

Prior to the ORR measurement, TEM was performed on several areas of the grid. The grid was then placed in the rotating disk set-up, the ORR was performed and the sample was then taken out again in order to repeat the TEM measurement. By using the appropriate coordinates, the same area on the TEM can be located.

3. Results and discussion

3.1. Validation of the concept

As a prerequisite, the Pt/C electrocatalyst on the TEM grid should not be affected by the transfer procedure from the microscope into the electrochemical cell and vice versa. The influence of the electrolyte was tested by submerging the TEM grid in 0.1 M $HClO_4$ overnight. From the IL images, no changes in the state of the electrocatalyst were observed, proving the reliability of the method.

The intense radiation of the electron beam can also bring about unpredictable changes to the structure of the catalyst [23]. Such artefacts from the measurement are highly undesirable. In order to account for these changes, following the electrochemical measurements, TEM analysis was also performed at locations which had not previously been exposed to the electron beam, henceforth denoted as 'different locations' (DL). These results will be discussed

in detail in Sections 3.2 and 3.3. In brief, only slight differences were observed between locations which had not previously been exposed to the electron beam and the 'identical locations' (IL).

3.2. Accelerated corrosion tests between 0.6 and 1.2 V

Fig. 2 shows the TEM images, taken before and after the ORR measurement, taken in identical locations. The sample was subjected to 3000 cycles between 0.6 and 1.2 V at 200 mV s^{-1} in 0.1 M $HClO_4$. From Fig. 2, it was found that (i) the total number of particles have decreased, following the corrosion experiment, some examples of particle disappearance are marked with red circles in the images. This was also determined after a particle count for each TEM image. (ii) The particles have decreased in size, examples are marked with green circles in the images. These phenomena are also confirmed more quantitatively by the size distribution graphs in Fig. 3a. The reduction in size and disappearance of the nanoparticles (see Fig. 2) strongly suggest that Pt has dissolved under these conditions. Moreover, there may have been some reprecipitation and sintering according to the size distribution graphs in Fig. 3a.

It should be noted that there are slight differences between the nanoparticle size distributions obtained from the identical and the different locations. In principle, the trend observed in both cases is similar. However, in the images taken from different locations, there is a marginally higher frequency of larger nanoparticles, following the corrosion experiment. Since an appreciable number of particles had disappeared altogether, the number of nanoparticles counted from IL images to obtain the nanoparticle size distribution was much less than for DL images. Thus, considering that both distributions show the same trend, the small differences observed could in principle be due to statistical artefacts, rather than a real electron beam effect. A recent *in situ* TEM study by Simonsen et al. attempted to account for the possibility of electron beam induced degradation on supported Pt nanoparticles [23]. They only observed an increase in shrinkage of Pt nanoparticles when the electron beam was combined with an oxidising gas environment in the *in situ* TEM.

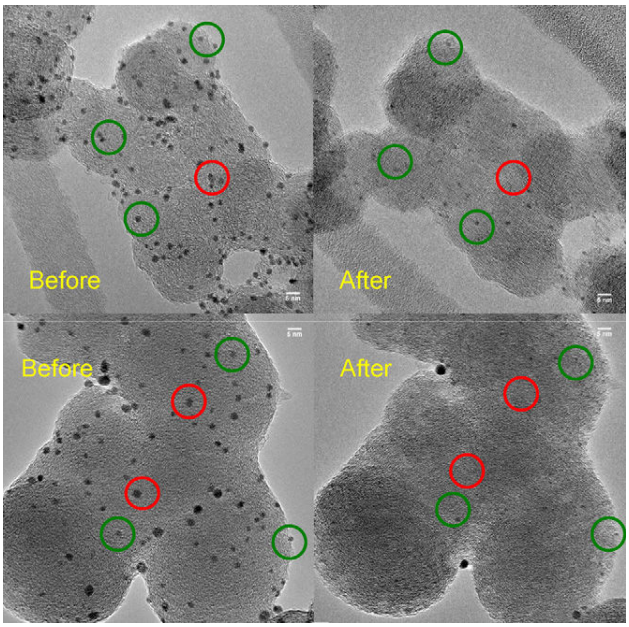

Fig. 2. IL-TEM images taken before and after accelerated corrosion test (sample was subjected to 3000 cycles between 0.6 and 1.2 V at 200 mV s^{-1} in 0.1 M $HClO_4$).

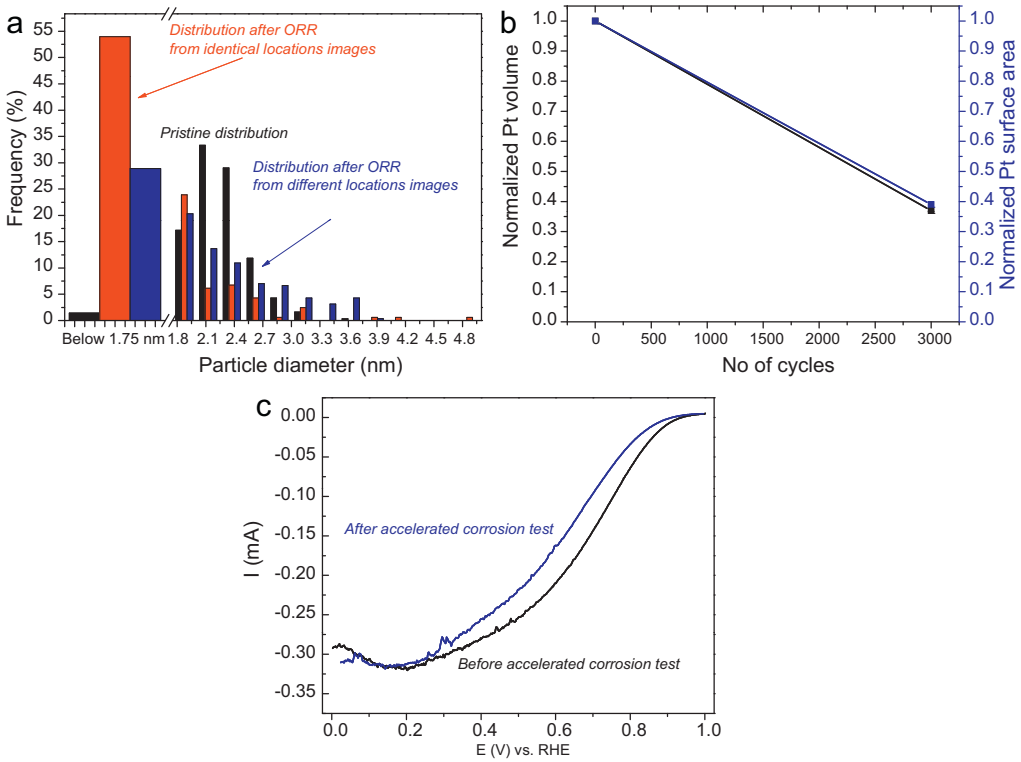

Fig. 3. (a) Nanoparticle size distribution graphs of sample subjected to 3000 cycles between 0.6 and 1.2 V, scan rate = 200 m V s^{-1} (black histogram: distribution from pristine sample (303 particles), red histograms: distribution after accelerated corrosion test from identical locations (156 particles), blue histograms (256 particles): distribution after accelerated corrosion test from different locations. (b) Normalized amount and surface area of Pt calculated before and after accelerated corrosion test from identical locations images. (c) ORR curve of sample before (black line) and after (blue line) accelerated corrosion test (For interpretation of the references to color in this figure legend, the reader is referred to the web version of the article.).

Since our TEM images were acquired in high vacuum, the electron beam effect is unlikely. Consequently, the slight differences observed between DL and IL distributions are ascribed to statistical artefacts.

Assuming a spherical shape for the nanoparticles, the area and the total volume of Pt present have been calculated from the IL images, before and after the ORR experiment, shown in Fig. 3b. A decrease of 60% in the volume and surface area of Pt was observed, as a result of the ORR corrosion experiment. Since a significant decrease in the Pt nanoparticle size was also observed, this loss of surface area is mainly attributed to the dissolution of Pt. This results correlates qualitatively with the electrochemical measurements of ORR activity, before and after the accelerated corrosion test, shown in Fig. 3c where a pronounced deactivation of 69 mV is observed in the half wave potential, $\Delta E_{1/2}$, after the accelerated corrosion test.

3.3. Accelerated corrosion tests between 0.6 and 1.1 V

Fig. 4 shows a different set of TEM images, where the catalyst has been cycled to the same conditions as in Fig. 2, albeit up to a maximum voltage of 1.1 V instead of 1.2 V, at 200 mV s^{-1}. On the basis of these images, there is some particle loss, movement and mild sintering, examples are noted with blue circles, but otherwise the particles have retained their shape during their exposure to ORR conditions. These observations are quantified in the size distribution graphs in Fig. 5a. The increased prevalence of larger particles, following the ORR, suggests that some sintering has occurred, most likely (albeit not definitively) through particle coalescence. The total volume of Pt calculated from identical locations remains unchanged while the Pt surface area decreases slightly (8%), again suggesting particle coalescence (see Fig. 5b). These results are consistent with the ORR activity measurements, where no deactivation was observed, as shown in Fig. 5c.

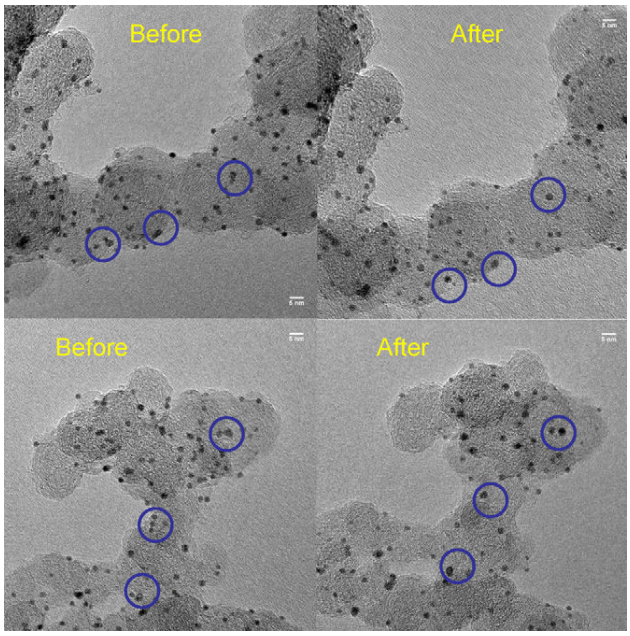

Fig. 4. IL-TEM images taken before and after accelerated corrosion test (sample was subjected to 3000 cycles between 0.6 and 1.1 V at 200 mV s^{-1} in 0.1 M $HClO_4$).

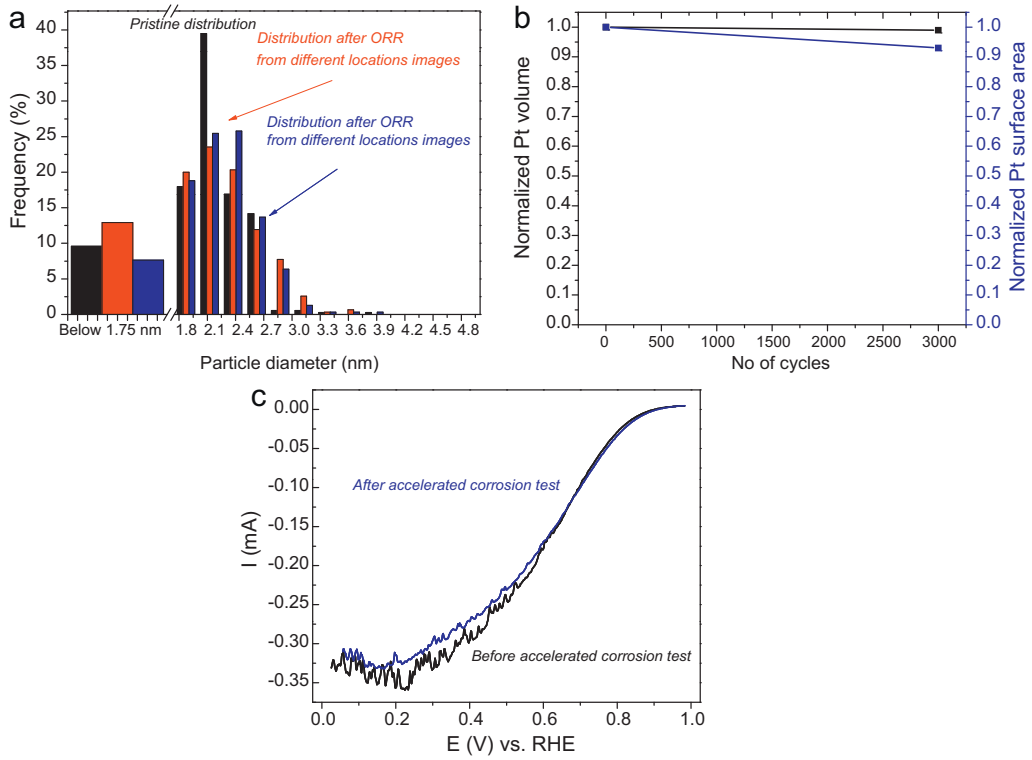

Fig. 5. (a) Nanoparticle size distribution graphs of sample subjected to 3000 cycles between 0.6 and 1.1 V, scan rate = 200 m V s^{-1} (black histogram: distribution from pristine sample (367 particles), red histograms: distribution after accelerated corrosion test from identical locations (311 particles), blue histograms: distribution after accelerated corrosion test from different locations (315 particles). (b) Normalized amount and surface area of Pt calculated before and after accelerated corrosion test from identical locations images. (c) ORR curve of sample before (black line) and after (blue line) accelerated corrosion test (For interpretation of the references to color in this figure legend, the reader is referred to the web version of the article.).

It is also worth noting that the particle distributions measured in the identical locations are roughly the same as those measured in different locations. This confirms that exposure to the electron beam does not have a significant effect on the experiments.

Since the effects on Pt degradation were not very significant after 3000 cycles of potential cycling between 0.6 and 1.1 V, the Pt/C catalyst was subjected to 30,000 cycles instead.

Fig. 6 displays the set of TEM images, before and after the accelerated corrosion test under these conditions. According to the images, there is some reduction in particle size (green circles), nanoparticle disappearance (red circles) and mild sintering (blue circles). In general, these effects are similar to those observed when the sample was cycled only 3000 times between 0.6 and 1.2 V. The size distribution graph, shown in Fig. 7a, confirms this trend: there are a higher number of large particles and there is an appreciable increase in the number of small nanoparticles, albeit to a lesser extent than the sample exposed to 3000 cycles up to 1.2 V. Notably, the catalyst exposed to 30,000 cycles does not seem to have sintered much more than the catalyst exposed to 3000 cycles. In summary, these results suggest that Pt dissolution is the main degradation mechanism under these conditions.

The total volume and the area of Pt present in the IL images have been calculated before and after the ORR experiment, as shown in Fig. 7b. In this case, a decrease of around 30% in Pt volume was observed after the ORR corrosion experiment. These results correspond qualitatively with the deactivation of 35 mV $\Delta E_{1/2}$ in ORR activity measured before and after aging, as shown in Fig. 7c. In this case, the loss in Pt surface area, at 22%, is less pronounced than the loss in its volume. This is in contrast to the experiment where the electrode was cycled for 3,000 cycles to 1.2 V (see Fig. 3b), where the proportion of surface area lost was equal to the proportion of volume lost. All of these results confirm that electrochemical dissolution of Pt is the major factor limiting this catalyst's durability with potential cycling for extended time periods.

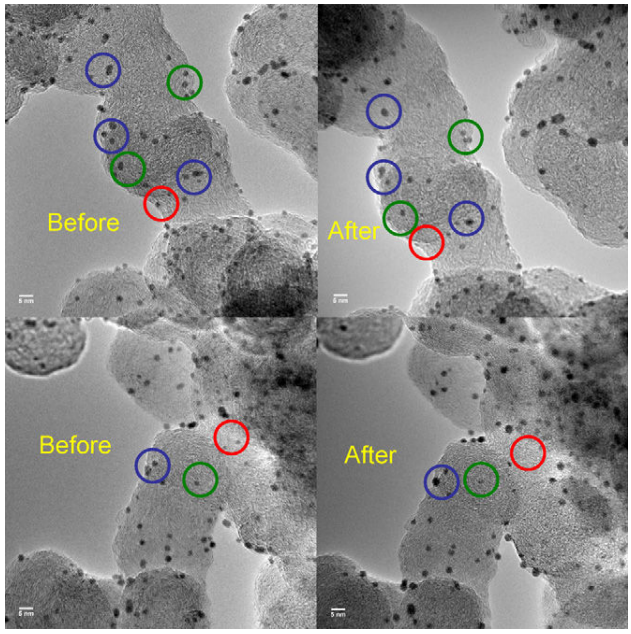

Fig. 6. IL-TEM images taken before and after accelerated corrosion test (sample was subjected to 30,000 cycles between 0.6 and 1.1 V at 200 mV s^{-1} in 0.1 M $HClO_4$).

However it is worthy to note that although our configuration allows a more direct comparison between the electrochemical

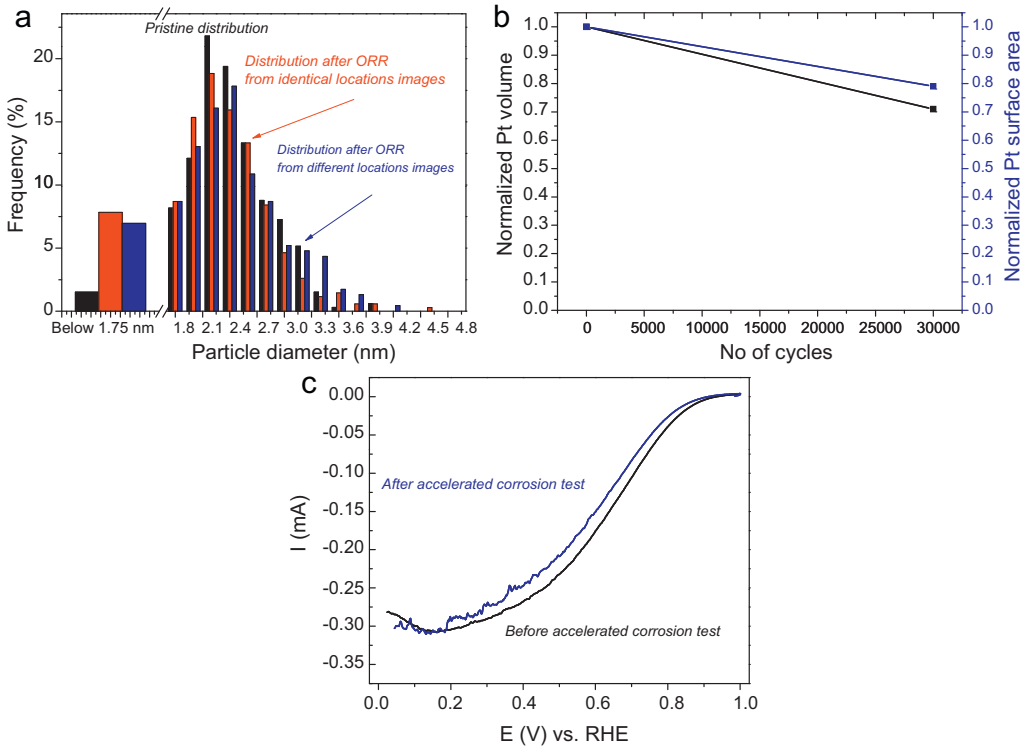

Fig. 7. (a) Nanoparticle size distribution graphs of sample subjected to 30,000 cycles between 0.6 and 1.1 V, scan rate = 200 m V s^{-1} (black histogram: distribution from pristine sample (303 particles), red histograms: distribution after accelerated corrosion test from identical locations (233 particles), blue histograms: distribution after accelerated corrosion test from different locations (230 particles). (b) Normalized amount and surface area of Pt calculated before and after accelerated corrosion test from identical locations images. (c) ORR curve of sample before (black line) and after (blue line) accelerated corrosion test (For interpretation of the references to color in this figure legend, the reader is referred to the web version of the article.).

measurements and the TEM analysis, the ORR curves obtained can be only interpreted qualitatively.

3.4. Effect of scan rate

In order to probe the effect of the scan rate on the phenomena observed, the experiments where the electrode was cycled 3000 times between 0.6 and 1.2 V and between 0.6 and 1.1 V were repeated a slower scan rate of 50 mV s^{-1}, instead of 200 mV s^{-1}. For both potential windows, the phenomena observed seemed to be independent of the scan rate (for brevity, these images have not been shown). This suggests that the Pt degradation is more dependent on the number of oxidation–reduction cycles, rather than the length of each cycle. Our observations are in agreement with the trends reported elsewhere in the literature [6].

3.5. Comparison to corrosion tests using 'thin film' rotating disk' electrode method

Although the use of a single working electrode in the form of a TEM grid allows a more direct comparison to be made between the electrochemical response and the TEM analysis, the electrochemical measurement is more qualitative than quantitative. Consequently, in the supplementary materials section, we present the results of equivalent measurements taken using the more conventional 'thin film' method [1,24]. Using the thin film method, a Pt/C ink is deposited onto the polished glassy carbon tip of a RDE (see the supplementary material). The loss of surface area was measured electrochemically by integrating the charge to adsorb H down to 0.05 V.

In brief, the thin film measurements showed that (a) the sample cycled up to 1.2 V for 3000 cycles showed a pronounced loss in surface area of ~50%, and a decrease in half wave potential of 25 mV (b) the sample cycled to 1.1 V for 3000 cycles showed a smaller loss in surface area and half wave potential, ~10% and ~8 mV, respectively, and (c) the sample cycled to 1.2 V for 30,000 cycles exhibited a more pronounced loss in the surface area and half wave potential, of 55% and of 35 mV, respectively. In (a) and (b) the electrochemically determined loss of surface area is comparable to that determined *ex situ* using the IL-TEM technique, whereas in (c) it seems to be more pronounced when the thin film method was used. The loss in half wave potentials is not exactly equivalent in the two methods. This is only to be expected, given the inherently more qualitative nature of the electrochemical measurement using the TEM grid as the sole working electrode.

Nonetheless, the generally good agreement between the two methods validates our approach for elucidating the mechanism of Pt/C degradation.

4. Discussion

According to the IL-TEM results, the degradation of our Pt/C electrocatalyst is primarily due to Pt dissolution, with some sintering, albeit to a lesser extent. To the best of our knowledge, the direct observation of Pt dissolution by the presence of particles with decreased size has not been reported previously.

The upper voltage limit value plays an important role during the accelerated corrosion test. Higher potentials (1.2 V versus 1.1 V) accelerate the dissolution of Pt. However, similar effects were observed when the sample was subjected to potential cycling between 0.6 and 1.1 V for longer time periods.

Our observations are also in good agreement with the main models described in the literature. Darling and Meyers [25,26] established a dissolution model for Pt particles, based on three different processes: electrochemical dissolution of the bare Pt surface, the oxidation of the Pt surface and the subsequent chemical dissolution of the oxidised Pt surface. They assumed that the chemical dissolution of oxidised Pt should be slow, and the electrochemical dissolution of Pt metal should predominate. Consequently, when the Pt surface is sufficiently oxidised, the underlying metal should be passivated against electrochemical dissolution. However, there has been some degree of debate as to whether Pt degradation in fuel cells occurs via the electrochemical dissolution of bare Pt or the chemical dissolution of oxidised Pt [7,25–29]. Kawahara et al. also suggest that the electrochemical reduction of PtO_2 could also play a role [30].

Regardless of the exact mechanism by which Pt dissolves, experimental evidence suggests that Pt dissolution should be enhanced considerably when the electrode is cycled to 1.2 V, instead of 1.1 V, in agreement with our own observations [25]. It is also known that Pt corrosion is enhanced when the voltage is cycled rather than under potentiostatic conditions [31].

It is worth perusing the differences between our own results and those of Mayrhofer et al., who using a similar IL-TEM methodology [20]. They observed very little, if any, degradation of their Pt/C catalyst when they cycled the electrode to 1.05 V or 1.2 V. However, we note that they used a different Pt/C catalyst, with a loading of ~50 wt% Pt, and particle diameter of 5 nm; in comparison, our catalyst had a loading of 10 wt% Pt and a smaller particle diameter of 2.5 nm.

There is a considerable body of theoretical and experimental evidence which would suggest that the stability of Pt nanoparticles is determined by their size [7,28,29,32,33]. Shao-Horn et al. made a thermodynamic estimation of particle size induced stability, using a thermodynamic analysis, based on the Gibbs Thomson equation and an extension of the Darling model [7]. They predicted an exponential increase in dissolution rate, as the particle size is decreased below 5 nm. Thus, the model established a critical change in lifetimes of nanoparticle to dissolve completely on the scale of many thousands of hours for 5 nm nanoparticles to the scale of ten to hundreds of hours for 2 nm ones.

Shao-Horn's analysis is also supported by the recent investigations of Tang et al. [28,29]. They directly measured the dissolution potential of individual Au supported Pt nanoparticles, using electrochemical scanning tunnelling microscopy (EC-STM). They supported their data with a series of density functional theory (DFT) calculations. Their theoretical model extended the simple Gibbs Thomson analysis, accounting for the role of surface passivation and site specific dissolution as a function of particle size. Both experiment and theory showed that the dissolution potential had an almost linear increase with particle size. For particles below 4 nm in diameter, the electrochemical dissolution of metallic Pt should be thermodynamically favoured. However, for nanoparticles above 4 nm in diameter, hydroxyl adsorption should occur at lower potentials than electrochemical Pt metal dissolution; in this case if dissolution occurs, it would be via the chemical dissolution of oxidised Pt.

On the basis of the aforementioned studies, it is perhaps unsurprising that our Pt nanoparticles, at 2.3 nm, should be more susceptible to dissolution than those of Mayrhofer et al., with a diameter of 5 nm.

In summary, in this work we report a reduction in nanoparticle size, for carbon supported Pt catalysts. The experimental conditions were chosen to simulate the start up and shut down cycles of a fuel cell. Our observations provide direct, microscopic evidence that dissolution phenomena are the main cause of degradation in Pt/C electrocatalysts, under ORR conditions.

The kinetics of Pt dissolution is dependent upon nanoparticle size, shape and their interaction with the support. An optimisation of these parameters would greatly reduce Pt surface area loss during voltage cycling. The extent of Pt dissolution seems to

be governed by a complex interplay between the electrochemical dissolution of Pt, the anodic formation of oxidised Pt and its subsequent dissolution. Further investigations are needed to develop a deeper understanding of Pt dissolution. With greater mechanistic insight, new strategies could be developed to avoid or restrict Pt corrosion during fuel cell operation.

5. Conclusions

This study has demonstrated the use of the IL-TEM method with the TEM grid as the sole working electrode. This configuration allowed a qualitative, albeit direct correlation to be made between the electrochemical response and the TEM analysis.

The Pt/C electrocatalyst was subjected to potential cycling, simulating the start-up and shut-down of a fuel cell. A reduction in particle size, with some particle disappearance, proved that Pt dissolution is the dominant mechanism of degradation. Some sintering occurred in all of experiments developed, most likely (albeit not definitively) through particle coalescence.

Increasing the upper voltage limit value (1.2 V) accelerated the corrosion of Pt. However, the same effects were also observed when the sample was subjected to potential cycling until 1.1 V for longer time periods.

Acknowledgements

We gratefully acknowledge funding from the Danish Strategic Research Council's HyCycle program, the Danish Council for Technology and Innovation's FTP program. IELS acknowledges funding from PSO-financed ForskEL/EL grant (High Performance MEA's, project 010076) from energinet.dk. FJPA acknowledges funding from the Spanish Government Ministry of Education's, "Programa Nacional de Movilidad de Recursos Humanos del Plan Nacional de I-D+I 2008–2011". The Center for Individual Nanoparticle Functionality is supported by the Danish National Research Foundation.

Appendix A. Supplementary data

Supplementary data associated with this article can be found, in the online version, at doi:10.1016/j.jpowsour.2011.03.064.

References

[1] H.A. Gasteiger, S.S. Kocha, B. Sompalli, F.T. Wagner, Applied Catalysis B-Environmental 56 (2005) 9–35.
[2] P. Strasser, S. Koh, T. Anniyev, J. Greeley, K. More, C.F. Yu, Z.C. Liu, S. Kaya, D. Nordlund, H. Ogasawara, M.F. Toney, A. Nilsson, Nature Chemistry 2 (2010) 454–460.
[3] V. Stamenkovic, B.S. Mun, K.J.J. Mayrhofer, P.N. Ross, N.M. Markovic, J. Rossmeisl, J. Greeley, J.K. Norskov, Angewandte Chemie-International Edition 45 (2006) 2897–2901.
[4] V.R. Stamenkovic, B.S. Mun, M. Arenz, K.J.J. Mayrhofer, C.A. Lucas, G.F. Wang, P.N. Ross, N.M. Markovic, Nature Materials 6 (2007) 241–247.
[5] J. Greeley, I.E.L. Stephens, A.S. Bondarenko, T.P. Johansson, H.A. Hansen, T.F. Jaramillo, J. Rossmeisl, I. Chorkendorff, J.K. Norskov, Nature Chemistry 1 (2009) 552–556.
[6] R. Borup, J. Meyers, B. Pivovar, Y.S. Kim, R. Mukundan, N. Garland, D. Myers, M. Wilson, F. Garzon, D. Wood, P. Zelenay, K. More, K. Stroh, T. Zawodzinski, J. Boncella, J.E. McGrath, M. Inaba, K. Miyatake, M. Hori, K. Ota, Z. Ogumi, S. Miyata, A. Nishikata, Z. Siroma, Y. Uchimoto, K. Yasuda, K.I. Kimijima, N. Iwashita, Chemical Reviews 107 (2007) 3904–3951.
[7] Y. Shao-Horn, W.C. Sheng, S. Chen, P.J. Ferreira, E.F. Holby, D. Morgan, Topics in Catalysis 46 (2007) 285–305.
[8] J. Zhang, K. Sasaki, E. Sutter, R.R. Adzic, Science 315 (2007) 220–222.
[9] S. Zhang, X.-Z. Yuan, J.N.C. Hin, H. Wang, K.A. Friedrich, M. Schulze, Journal of Power Sources 194 (2009) 588–600.
[10] Y.Y. Shao, G.P. Yin, Y.Z. Gao, Journal of Power Sources 171 (2007) 558–566.
[11] S. Chen, H.A. Gasteiger, K. Hayakawa, T. Tada, Y. Shao-Horn, Journal of the Electrochemical Society 157 (2010) A82–A97.
[12] F. Maillard, L. Dubau, J. Durst, M. Chatenet, J. Andre, E. Rossinot, Electrochemistry Communications 12 (2010) 1161–1164.
[13] E. Guilminot, A. Corcella, M. Chatenet, F. Maillard, F. Charlot, G. Berthome, C. Iojoiu, J.Y. Sanchez, E. Rossinot, E. Claude, Journal of the Electrochemical Society 154 (2007) B1106–B1114.
[14] P.J. Ferreira, G.J. la O, Y. Shao-Horn, D. Morgan, R. Makharia, S. Kocha, H.A. Gasteiger, Journal of the Electrochemical Society 152 (2005) A2256–A2271.
[15] K. Yasuda, A. Taniguchi, T. Akita, T. Ioroi, Z. Siroma, Physical Chemistry Chemical Physics 8 (2006) 746–752.
[16] T. Akita, A. Taniguchi, J. Maekawa, Z. Sirorna, K. Tanaka, M. Kohyama, K. Yasuda, Journal of Power Sources 159 (2006) 461–467.
[17] P. Yu, M. Pemberton, P. Plasse, Journal of Power Sources 144 (2005) 11–20.
[18] K.J.J. Mayrhofer, M. Hanzlik, M. Arenz, Electrochimica Acta 54 (2009) 5018–5022.
[19] K.J.J. Mayrhofer, J.C. Meier, S.J. Ashton, G.K.H. Wiberg, F. Kraus, M. Hanzlik, M. Arenz, Electrochemistry Communications 10 (2008) 1144–1147.
[20] K.J.J. Mayrhofer, S.J. Ashton, J.C. Meier, G.K.H. Wiberg, M. Hanzlik, M. Arenz, Journal of Power Sources 185 (2008) 734–739.
[21] J.P. Wilcoxon, B.L. Abrams, Chemical Society Reviews 35 (2006) 1162–1194.
[22] P. Hernandez-Fernandez, S. Rojas, P. Ocon, J.L.G. de la Fuente, P. Terreros, M.A. Pena, J.L. Garcia-Fierro, Applied Catalysis B-Environmental 77 (2007) 19–28.
[23] S.B. Simonsen, I. Chorkendorff, S. Dahl, M. Skoglundh, J. Sehested, S. Helveg, Journal of the American Chemical Society 132 (2010) 7968–7975.
[24] K.J.J. Mayrhofer, D. Strmcnik, B.B. Blizanac, V. Stamenkovic, M. Arenz, N.M. Markovic, Electrochimica Acta 53 (2008) 3181–3188.
[25] R.M. Darling, J.P. Meyers, Journal of the Electrochemical Society 150 (2003) A1523–A1527.
[26] R.M. Darling, J.P. Meyers, Journal of the Electrochemical Society 152 (2005) A242–A247.
[27] S.G. Rinaldo, J. Stumper, M. Eikerling, Journal of Physical Chemistry C 114 (2010) 5773–5785.
[28] L. Tang, B. Han, K. Persson, C. Friesen, T. He, K. Sieradzki, G. Ceder, Journal of the American Chemical Society 132 (2009) 596–600.
[29] L. Tang, X. Li, R.C. Cammarata, C. Friesen, K. Sieradzki, Journal of the American Chemical Society 132 (2010) 11722–11726.
[30] S. Kawahara, S. Mitsushima, K. Ota, N. Kamiya, ECS Transactions 3 (2006) 625–631.
[31] K. Kinoshit, Jt Lundquis, P. Stonehar, Journal of Electroanalytical Chemistry 48 (1973) 157–166.
[32] R. Makharia, S. Kocha, P. Yu, M.A. Sweikart, W. Gu, F. Wagner, H.A. Gasteiger, ECS Transactions 1 (2006) 3–18.
[33] R. Jinnouchi, E. Toyoda, T. Hatanaka, Y. Morimoto, The Journal of Physical Chemistry C 114 (2010) 17557–17568.